

Degradation Study on Solid Oxide Steam Electrolysis

Von der Fakultät Energie-, Verfahrens- und Biotechnik der Universität Stuttgart
zur Erlangung der Würde eines Doktors der Ingenieurwissenschaften (Dr.-Ing.)
genehmigte Abhandlung

vorgelegt von
Michael Philipp Hörlein
aus München

Hauptberichter: Prof. Dr. K. Andreas Friedrich
Mitberichter: Prof. Dr. Jürgen Fleig

Tag der mündlichen Prüfung: 1. Juli 2020

Institut für Gebäudeenergetik, Thermotechnik und Energiespeicherung
der Universität Stuttgart

2020

Acknowledgements

I thank Prof. Andreas Friedrich for giving me the opportunity to conduct my research on an equally interesting and promising topic. I am thankful for his support as well as for allowing me to finish the thesis abroad and accepting the resulting delay.

For his supervision as well as his friendly and trusting attitude I would like to thank Dr. Günter Schiller. I thank Prof. Jürgen Fleig for co-supervising this work.

Special thanks go to my colleagues Matthias Riegraf and Rémi Costa. I enjoyed many fruitful discussions and am thankful for the occasional motivational boost provided in strenuous times.

For their support and goodwill I would like to thank Ina Plock, Robert Ruckdäschel, Indro Biswas and Vitaly Yurkiv. They all provided viable input from their respective field of expertise and I gratefully acknowledge their contribution to this work.

Finally, I feel the urge to thank my wife Anna for carrying my decisions surrounding this work. I know this episode was not easy for you and I greatly appreciate your support – private and technical – while at the same time accepting my pace at finishing this work. Thank you!

Abstract

Steam solid oxide electrolysis (SOE) is a method to transform electrical into chemical energy in the form of hydrogen with the prospect of very high conversion efficiencies, which could play a major role as storage capacity in future electricity systems. However, its longevity is limited by numerous degradation processes which need to be addressed before. This thesis elucidates degradation of solid oxide electrolysis cells (SOEC) by systematically investigating the influence of three key operating parameters – temperature, hydrogen gas humidity and current density – on cell deterioration.

A detailed understanding of rate limiting processes governing cell performance was achieved based on experimental results as well as the application of a physico-chemical model approach. Five processes, separable by electrochemical impedance spectroscopy were identified: the ohmic resistance accounting for the conduction of ions through the electrolyte as well as contact resistances, a hydrogen electrode process representing oxygen ion conduction within the hydrogen electrodes' YSZ backbone coupled with the charge transfer reaction, the hydrogen electrode charge transfer reaction, the oxygen electrode's charge transfer reaction coupled with its oxygen ion transport and finally mass transport limitations.

In order to study the influence of operating conditions on degradation, a series of 20 SOECs were operated for 1000 h under identical conditions, while only the investigated parameters deviated. The influence of temperature was investigated between 750 °C and 850 °C, the humidity ranged from 40 %MH to 80 %MH, while the current density varied between OCV and 1.5 A/cm². This systematic parameter study allowed for the separation of four independent degradation processes, two of which contribute to the ohmic resistance and would be inseparable otherwise. Furthermore, it provides in-sight into the mechanism of each degradation process.

One major source of degradation is caused by unidirectional transport of Ni away from the hydrogen electrode | electrolyte interface, leaving behind a porous YSZ layer virtually deprived of Ni, which effectively translates into an increase of the electrolyte's thickness. This Ni-depletion is driven by current density and only occurs significantly at humidities of 80 %MH and temperatures of 800 °C and above. A second degradation process, also contributing to the ohmic resistance, was identified to be a partial change of the electrolyte's crystallographic phase from cubic to tetragonal. This process shows

a linear progression with the square root of time and is more pronounced at lower temperatures within the investigated range of parameters. Another important source of degradation could be linked to a change in the crystallographic structure of the oxygen electrode, which is dependent on operating temperature but largely unaffected by current density. Finally, the hydrogen electrode also exhibits degradation for most investigated conditions. While it is exposed to a series of degradation mechanisms, it is shown that the degradation mainly originates from a change of the ionic conductivity in the YSZ backbone while the charge transfer plays a minor role. Thus, observed microstructural changes resulting in a reduction of the triple phase boundary (TPB) length are not primarily responsible for hydrogen electrode degradation.

Zusammenfassung

Die Wasserdampfelektrolyse mittels Festoxidzellen (SOE) ist eine Methode elektrische in chemische Energie in Form von Wasserstoff umzuwandeln. Sie hat das Potential sehr hohe Umwandlungseffizienz zu erreichen und könnte als Speicher eine große Rolle in zukünftigen Energiesystemen darstellen. Verschiedene Degradationsprozesse limitieren jedoch ihre Lebensdauer und müssen zunächst kontrolliert werden. Diese Arbeit vertieft das Verständnis der Degradation von Festoxidelektrolysezellen (SOEC), indem systematisch der Einfluss der drei Schlüsselparameter – Temperatur, Brenngasfeuchtigkeit und Stromdichte – untersucht wird.

Ein detailliertes Verständnis der Prozesse, welche die Leistungsfähigkeit der Zelle limitieren, wurde sowohl durch experimentelle Ergebnisse als auch durch die Anwendung eines physiko-chemischen Modells erreicht. Dabei wurden fünf durch elektrochemische Impedanzspektroskopie unterscheidbare Prozesse identifiziert: der ohmsche Widerstand, der die Leitung von Ionen durch den Elektrolyten sowie Kontaktwiderstände darstellt, der Transport von Sauerstoffionen durch das YSZ-Rückgrat der Brenngaselektrode gekoppelt mit dem Ladungstransferwiderstand, der Ladungstransferwiderstand der Brenngaselektrode, der Ladungstransferwiderstand der Sauerstoffelektrode gekoppelt mit dem Sauerstoffionen Transport und schließlich Massentransportlimitierungen.

Um den Einfluss der Betriebsparameter auf die Degradation zu untersuchen, wurden 20 SOECs für 1000 h betrieben. Dabei unterschieden sich die Betriebsbedingungen nur in dem zu untersuchenden Parameter. Der Einfluss der Temperatur wurde zwischen 750 °C und 850 °C, der Feuchtigkeit zwischen 40 %MH und 80 %MH und der Stromdichte zwischen OCV und 1.5 A/cm² untersucht. Diese systematische Parameterstudie erlaubte es vier unabhängige Degradationsprozesse zu separieren, wovon zwei zur Erhöhung des ohmschen Widerstands beitragen und andernfalls nicht unterscheidbar wären. Außerdem ermöglicht diese Studie Einsicht in die Mechanismen der jeweiligen Degradationsprozesse.

Eine Hauptquelle der Degradation liegt im Transport von Ni von der Grenzfläche Brenngaselektrode | Elektrolyt weg. Die zurückbleibende Schicht ist praktisch von Ni befreit und entspricht somit einer Erhöhung der Elektrolytdicke. Diese Ni-Verarmung ist Stromdichte-getrieben und findet in nennenswertem Maß nur bei 80 %MH und min-

destens 800 °C statt. Ein zweiter Degradationsprozess, der ebenfalls zum ohmschen Widerstand beiträgt konnte als teilweise kristallographischer Phasenwechsel des Elektrolyten von kubisch zu tetragonal identifiziert werden. Dieser Prozess wächst linear mit der Quadratwurzel der Zeit und ist im untersuchten Bereich bei niedrigeren Temperaturen stärker ausgeprägt. Eine weitere wichtige Quelle der Degradation konnte mit der Veränderung der kristallographischen Struktur der Sauerstoffelektrode in Verbindung gebracht werden. Diese hängt von der Betriebstemperatur ab, ist jedoch nahezu unbeeinflusst von der Stromdichte. Schließlich degradiert auch die Brenngaselektrode bei den meisten der untersuchten Betriebsbedingungen. Während sie verschiedene Degradationsmechanismen ausgesetzt ist konnte gezeigt werden, dass die Degradation hauptsächlich von einer Verschlechterung der Leitfähigkeit des YSZ-Rückgrats herrührt und kaum von der Ladungstransferreaktion. Folglich sind mikrostrukturelle Veränderungen, die in den Elektroden beobachtet wurden und zu einer Reduktion der Länge der Dreiphasengrenze (TPB) führen nicht hauptverantwortlich für die Degradation der Brenngaselektrode.

Contents

| | | |
|----------|--|-----------|
| 1 | Introduction | 1 |
| 1.1 | Scope of the present dissertation | 2 |
| 1.2 | Outline of the present dissertation | 3 |
| 2 | Scientific and Technological Background | 4 |
| 2.1 | Solid oxide electrolysis cell..... | 4 |
| 2.1.1 | Functional principle..... | 4 |
| 2.1.2 | Cell architectures and materials | 5 |
| 2.2 | Advantages of solid oxide electrolysis | 7 |
| 2.3 | Degradation rate terminology | 8 |
| 2.4 | Literature review on SOE degradation..... | 10 |
| 2.4.1 | Hydrogen electrode degradation | 11 |
| 2.4.2 | Oxygen electrode degradation | 12 |
| 2.4.3 | Electrolyte degradation..... | 14 |
| 3 | Scientific Approach and Methodology | 16 |
| 3.1 | Experimental concept and scientific approach | 16 |
| 3.2 | Experimental set-up..... | 19 |
| 3.2.1 | Test rig | 20 |
| 3.2.2 | Cell housing..... | 20 |
| 3.2.3 | Humidification | 23 |
| 3.2.4 | Impedance spectroscopy measurement..... | 24 |
| 3.2.5 | Heat-up, reduction, initiation and cool down..... | 25 |
| 3.2.6 | Procedure of degradation experiment | 25 |
| 3.2.7 | Solid oxide electrolysis cells | 26 |
| 3.3 | Post-test measurements..... | 26 |
| 3.3.1 | Scanning electron microscopy..... | 27 |
| 3.3.2 | Raman spectroscopy..... | 27 |
| 3.3.3 | X-ray diffraction | 28 |
| 3.3.4 | X-ray photoelectron spectroscopy | 28 |
| 3.3.5 | Image analysis..... | 28 |
| 3.4 | Model simulation..... | 29 |
| 4 | Cell Characterization | 31 |
| 4.1 | Microstructural characterization..... | 31 |
| 4.2 | Characterization of electrochemical performance..... | 35 |
| 4.3 | Simulative characterization..... | 41 |
| 4.3.1 | Model validation..... | 41 |

| | | |
|----------|---|------------|
| 4.3.2 | Reduction studies | 45 |
| 5 | Degradation Study | 50 |
| 5.1 | Ohmic resistance | 51 |
| 5.1.1 | Ni-depletion | 51 |
| 5.1.1.1 | In-situ results | 51 |
| 5.1.1.2 | Post-test results..... | 54 |
| 5.1.1.3 | Discussion | 60 |
| 5.1.2 | YSZ-aging | 70 |
| 5.1.2.1 | In-situ results | 70 |
| 5.1.2.2 | Post-test results..... | 71 |
| 5.1.2.3 | Discussion | 74 |
| 5.1.3 | Further investigations regarding ohmic resistance | 80 |
| 5.2 | Oxygen electrode resistance | 83 |
| 5.2.1 | In-situ results | 83 |
| 5.2.2 | Post-test results..... | 88 |
| 5.2.3 | Discussion | 99 |
| 5.3 | Hydrogen electrode resistance | 103 |
| 5.3.1 | In-situ results | 103 |
| 5.3.2 | Post mortem results..... | 108 |
| 5.3.3 | Discussion | 109 |
| 5.4 | Gas Diffusion and Conversion | 111 |
| 6 | Conclusion | 112 |
| 7 | Outlook | 114 |

List of Tables

| | |
|--|-----|
| Table 1: Parameters of contacting meshes..... | 23 |
| Table 2: Reduction procedure..... | 25 |
| Table 3: List of parameters used for electrochemical modeling in this study ... | 30 |
| Table 4: Quantification of microstructural properties of the hydrogen electrode in its initial state..... | 35 |
| Table 5: Processes considered for quantification, their respective physical interpretation, initial characteristic frequency and typical initial resistance at 800 °C, 60 %MH and 0.5 A·cm ⁻² | 40 |
| Table 6: Overview of the increase of ohmic resistance after 1000 h for all 20 long-term tests. | 53 |
| Table 7: Crystallographic lattice parameters of oxygen electrode's phases of reference sample as well as operated cells. | 94 |
| Table 8: List of ionic radii of LSCF ions according to [135] | 102 |
| Table 9: Hydrogen electrodes' microstructural characteristics of cells operated at OCV in comparison to reference cell. | 109 |

List of Figures

| | | |
|----------|--|----|
| Fig. 1: | Overview of typical power output, capacity values and discharge times for several EES systems [2] | 2 |
| Fig. 2: | General principle of a solid oxide electrolysis cell. | 5 |
| Fig. 3: | Energy demand for water electrolysis as a function of temperature at standard pressure. | 8 |
| Fig. 4: | Testmatrix consisting of three temperatures, three humidities and four current densities devised to individually identify the influence of each investigated parameter on degradation processes. A 1000 h degradation experiment is conducted at each of the 20 presented combinations of operating conditions. | 17 |
| Fig. 5: | Degradation experiment of four cells measured for 1000 h at 800 °C, 80 %MH and OCV, 0.5 A/cm ² , 1.0 A/cm ² and 1.5 A/cm ² , respectively. The black vertical lines indicate the interruption of current for intermediate cell characterization by EIS measurements. | 18 |
| Fig. 6: | (A) Progression of each individual resistance contribution during operation compared to (B) the absolute change of each individual resistance contributions. Both are exemplary shown for a cell operated at 800 °C and 80 %MH at OCV. | 19 |
| Fig. 7: | (A) Sealing concept of implemented new cell holder design compared to (B) sealing principle of conventional cell holder designs..... | 22 |
| Fig. 8: | Representative Kramers-Kronig test of a recorded impedance spectrum attests high EIS quality. | 24 |
| Fig. 9: | Cross-section of a reference cell displaying the respective cell layers | 32 |
| Fig. 10: | Image of the porous LSCF structure of the oxygen electrode close to the electrolyte of a reference cell | 32 |
| Fig. 11: | Exemplary section of the hydrogen electrode of a reference cell which is used for quantitative analysis. Images of this section were recorded using SE detector (A) and IL detector (B). Combining this information (C) leads to a separation of the three phases pores (red), percolated Ni (yellow) and YSZ (rest) which can then be used for quantification. | 34 |
| Fig. 12: | Polarization curve of a representative cell in fuel cell mode at 4 %MH after reduction..... | 35 |
| Fig. 13: | Representative induction-corrected impedance spectra of cells in their initial state measured at 4 %MH and OCV, 60 %MH and OCV as well as 60 %MH and -0.5 A/cm ² . Image at the top shows the Nyquist plot of the spectra while the bottom graph shows the imaginary Bode plot. | 36 |
| Fig. 14: | DRT analysis of an impedance spectrum of a cell in its initial state. Four processes can be separated with specific frequencies of 10 ⁴ Hz (hydrogen electrode), 10 ³ Hz (hydrogen electrode), 10 ² Hz (oxygen electrode) and 10 Hz (gas transport). | 38 |

| | |
|--|----|
| Fig. 15: (A) Equivalent circuit model used for quantification of recorded impedance spectra and (B) location of individual rate limiting steps .. | 39 |
| Fig. 16: Four representative impedance spectra of cells in their initial state recorded at 800 °C, 60 %MH and 0.5 A/cm ² which reveal the cells' good reproducibility. Contributions of individual rate limiting processes are visualized..... | 40 |
| Fig. 17: Comparison of recorded (dots) and simulated (line) impedance spectra at OCV, 60 %MH and various temperatures..... | 42 |
| Fig. 18: Comparison of recorded (dots) and simulated (line) impedance spectra at OCV, 800 °C and various humidities. | 43 |
| Fig. 19: Comparison of recorded (dots) and simulated (line) impedance spectra at 60 %MH, 800 °C and various current densities. | 44 |
| Fig. 20: Measured (dots) and simulated (line) polarization curves at 60 %MH and a temperature of 700 °C and 800 °C..... | 45 |
| Fig. 21: Model reduction study at OCV, 60 %MH and 800 °C. Comparison between simulated impedance of the "full 2D model" (solid black line) and two reduced models: A "reduced 1D model" (dashed red line) excluding gas conversion and the "model of oxygen electrode only" isolating oxygen electrode / electrolyte electrochemistry (dash-dotted blue line). | 46 |
| Fig. 22: Change of charge transfer reaction rate (CT rate) in "reduced 1D model" (red line) and its effect on impedance. Minus sign (-) denotes the decrease of the parameter (dash dot line), plus sign (+) denotes the increase of parameter (dotted line). Conditions are 800 °C, OCV and 60 %MH for all spectra. | 48 |
| Fig. 23: Change of YSZ content of hydrogen electrode in " reduced 1D model" (red line) and its effect on impedance. Minus sign (-) denotes the decrease of the parameter (dash dot line), plus sign (+) denotes the increase of parameter (dotted line). Conditions are 800 °C, OCV and 60 %MH for all spectra. | 49 |
| Fig. 24: Voltage evolution with time for cells operated at different current densities and (a) 800 °C and 40 %MH, (b) 800 °C and 60 %MH, (c) 800 °C and 80 %MH, (d) 750 °C and 80 %MH, and (e) 850 °C and 80 %MH. | 50 |
| Fig. 25: Change in ohmic resistance of cells operated at different current densities and (a) 800 °C and 40 %MH, (b) 800 °C and 60 %MH, (c) 800 °C and 80 %MH, (d) 750 °C and 80 %MH, and (e) 850 °C and 80 %MH. | 52 |
| Fig. 26: SEM image of the electrolyte hydrogen electrode interface of a reference cell. It was recorded at low acceleration voltages and without prior carbon deposition. Using this technique four different phases can be distinguished: YSZ, pores, percolated and non-percolated Ni..... | 56 |
| Fig. 27: Images of the electrolyte hydrogen electrode interfaces of four cells operated at 800 °C and 80 %MH for 1000 h. The cells presented were measured at OCV, 0.5 A/cm ² , 1.0 A/cm ² and 1.5 A/cm ² , respectively. Increasingly large areas depleted of Ni can be observed with increasing current density. The SEM-Legend | |

- displayed for the cell operated at OCV is representative for all images of Fig. 27 through Fig. 29. 56
- Fig. 28: Images of the electrolyte | hydrogen electrode interfaces of four cells operated at 800 °C and 1.5 A/cm². The cells presented were measured at 40 %MH, 60 %MH, 80 %MH, respectively. While the cell operated at 80 %MH clearly shows a layer completely depleted of Ni, the cell run at lower humidities do not show distinct signs of Ni depletion. The dark spots in the percolated Ni-phase of the 40 %MH-image are caused by problems during sample preparation. 58
- Fig. 29: Images of the electrolyte | hydrogen electrode interfaces of four cells operated at 80 %MH and 1.5 A/cm² for 1000 h. The cells presented were measured at 750 °C, 800 °C and 850 °C, respectively. A high degree of Ni-depletion could be found at the cells run at 800 °C and 850 °C, which forms a layer completely deprived of Ni. The cell measured at 750 °C also shows Ni-depletion, which are, however, less pronounced and limited to small regions. The dark spots in the percolated Ni-phase of the 750 °C-image are caused by problems during sample preparation. ... 59
- Fig. 30: Schematic depiction of the gas concentrations in a SOEC hydrogen electrode in dependence of the distance from the electrolyte. The change in gas compositions results in a gradient of the redox potential, i.e. in stronger reducing conditions closer to the electrolyte. 62
- Fig. 31: Hypothesis on Ni-depletion as presented by Mogensen et al.[29]. In the electrode close to the electrolyte Ni particles have lost contact to the YSZ structure as well as to each other (Lost contact zone, LCZ). The reaction zone is shifted away from the electrolyte to the intact structure zone (ISZ). Ni migrates from the support along the steam gradient to the reaction zone, while Ni also migrates from the nonpolarized isolated particles close to the electrolyte. 63
- Fig. 32: Comparison of two cells operated in SOEC mode. Cell A (1000 h, 800 °C, 1.25 A/cm², 90/10 H₂O/H₂) [11] clearly shows the loss of contact between Ni and YSZ particles (red arrows). The cell in Fig. 32B (1000h, 800 °C, 1.5 A/cm², 80/20 H₂O/H₂) does not show this gap formation and is representative for the cells degraded during this study. 64
- Fig. 33: Potential difference between percolated and non-percolated Ni particles both connected to the YSZ skeleton. (A) displays a scenario where the gas concentration as well as the μ_{O_2} are identical, resulting in a potential difference equal to the Ni overpotential. (B) describes a scenario where both Ni particles are located at different distances from the electrolyte, resulting in an additional potential difference caused by difference in μ_{O_2} , i.e. the overvoltage necessary to transport the O²⁻-ions through the YSZ shaft. 65
- Fig. 34: Schematic depiction of local heat generation (positive voltages) and consumption (negative voltages) in electrolysis and fuel cell mode. (a) Local heat generation for a SOEC with ideally non-

| | | |
|----------|---|----|
| | polarizable electrodes. (b) Local heat generation for a SOEC at thermo-neutral conditions (sum of heat source and sink terms = 0), with reversible heat generation/consumption from (a) and irreversible terms at hydrogen electrode (P1+P2), electrolyte (P0) and oxygen electrode (P3) estimated based on initial resistance values in Table 5. (c) Local heat generation for a SOFC with ideally non-polarizable electrodes. (d) Local heat generation for a SOFC assuming the same irreversible losses as for the SOEC in (b). Heat generation based on mass transport is assumed to be negligible..... | 69 |
| Fig. 35: | Degradation of the ohmic resistance at OCV and different temperatures (left) and different humidities (right). | 70 |
| Fig. 36: | Time dependence of ohmic degradation at OCV based on the square root time. | 71 |
| Fig. 37: | (A) Area normalized Raman spectra of two cells operated at 750 °C and 850 °C, respectively, in comparison with the reference cell. For better visualization intensities of cell '750 °C' are shifted by 0.25 and of cell '850 °C' are shifted by 0.5. (B) Difference between spectra of operated cells and reference sample (C) Difference between spectra of cells operated at 750 °C and 850 °C. Degraded cells were operated at OCV and 80 %MH. | 73 |
| Fig. 38: | Zirconia-Yttria phase diagram according to Lakiza et al. [112] including the lines (dotted) for metastable diffusionless transformation from cubic to tetragonal (line 1) and from tetragonal to monoclinic (line 2). | 75 |
| Fig. 39: | Temperature required to achieve a mean diffusion distance of 1 nm, 5 nm and 15 nm for Y ³⁺ and of 1 μm, 5 μm and 15 μm for O ²⁻ after a certain time in YSZ. Calculation is based on diffusion data extracted from [109, 114, 115]. | 76 |
| Fig. 40: | EDS linescans through electrolyte and diffusion barrier layer towards oxygen electrode. (A) and (B) show SEM images of linescan location of reference cell and cell operated at 850 °C and OCV, respectively. The dashed red circle shows a singular indent with increased Sr concentration. (C) to (F) show the intensity profiles of Zr, Y, La and Sr for various investigated cells. | 81 |
| Fig. 41: | SEM images of electrolytes of different cells for comparison of microstructural integrity. (A) reference cell, (B) through (D) cells operated at 1.5 A/cm ² , 80 %MH and 750 °C, 800 °C and 850 °C, respectively. | 83 |
| Fig. 42: | Influence of operating temperature on degradation of oxygen electrode process. Cells operated at (A) 750 °C, (B) 800 °C and (C) 850 °C, current densities of OCV, 0.5 A/cm ² , 1.0 A/cm ² , 1.5 A/cm ² at each respective temperature and 80 %MH. | 86 |
| Fig. 43: | Influence of operating temperature on degradation of oxygen electrode process. Cells operated at (A) 40 %MH, (B) 60 %MH and (C) 80 %MH, current densities of OCV, 0.5 A/cm ² , 1.0 A/cm ² , 1.5 A/cm ² at each respective humidity and 800 °C..... | 87 |
| Fig. 44: | BSE-SEM images of the oxygen electrode of (A) reference sample and (B) the cell operated at 800 °C, 80 %MH and 1.0 A/cm ² for 1000 h | 89 |

- Fig. 45: Average A- and B-site composition of LSCF layer in vicinity of electrolyte measured by REM-EDS analysis of cells operated at combinations of temperature (750 °C, 800 °C and 850 °C) and current densities (OCV, 0.5 A/cm², 1.0 A/cm², 1.5 A/cm²). All cells were operated at 80 %MH..... 90
- Fig. 46: XPS analysis of LSCF cation concentration on surface of LSCF structure. The measurements were conducted on the LSCF surface previously in touch with the contacting mesh. Beside the reference, two cells operated at 800 °C, 80 %MH and OCV and 1.5 A/cm², respectively were investigated. (Compare Fig. 42B for respective in-situ results) 92
- Fig. 47: XRD spectra of LSCF layer of cells operated at (A) 750 °C, (B) 800 °C and (C) 850 °C and different current densities, respectively, in comparison with a reference sample. Cells operated at 750 °C show no significant changes. Cells operated at 800 °C and 850 °C show the formation of additional peaks at slightly lower angles relative to the peaks of the reference sample, suggesting the formation of a secondary phase..... 96
- Fig. 48: Recorded XRD spectrum of reference sample with fits (top) and corresponding residuals (bottom). The reference spectrum was fitted assuming cubic (*Pm3m*) or rhombohedral (*R3c: R*) structure. ... 97
- Fig. 49: Recorded XRD spectrum of cell operated at OCV and 800°C with fit assuming two cubic (*Pm3m*) structures (top) and corresponding residuals (bottom). 98
- Fig. 50: Change in hydrogen electrode resistance of the cells operated at (a) 800 °C and 40 %MH, (b) 800 °C and 60 %MH, (c) 800 °C and 80 %MH, (d) 750 °C and 80 %MH, and (e) 850 °C and 80 %MH. The graphs show the increase in total hydrogen electrode resistance P1 + P2 in the left panel and the increase of the individual contributions P1 and P2 in the right panel..... 106
- Fig. 51: Bode Plots of cells operated at 800 °C, 80 %MH and OCV, 0.5 A/cm², 1.0 A/cm² and 1.5 A/cm², respectively, displaying the change of impedance characteristics during 1000 h of operation. ... 108

Abbreviations

| | |
|-------|--|
| ASB: | angle selective backscattering |
| ASC: | anode supported cell |
| BSE: | back scattered electron |
| CGO: | Ceria Gadolinium Oxide |
| CNLS: | complex nonlinear least squares |
| CPE: | constant phase element |
| CSC: | cathode supported cell |
| CT: | charge transfer |
| DoE | design of experiments |
| EDS: | energy-dispersive X-ray spectroscopy |
| EES: | electric energy storage |
| EIS: | electrochemical impedance spectroscopy |
| ESC: | electrolyte supported cell |
| GDC: | Gadolinia doped Ceria |
| GDU: | gas distribution unit |
| ILD: | in-lense detector |
| ISZ: | intact structure zone |
| LCZ: | lost contact zone |
| LSCF: | Lanthanum Strontium Cobalt Ferrite |
| LSM: | Lanthanum Strontium Manganite |
| MEA | membrane electrode assembly |
| MH: | molar humidity |
| MIEC: | mixed ion-electron conductor |
| MSC: | metal supported cell |
| OCV: | open circuit voltage |
| ScSZ: | Scandia stabilized Zirconia |
| SED: | secondary electron detector |
| SEM: | scanning electron microscopy |
| smL | standard milliliter |
| SOC: | solid oxide cell |
| SOE: | solid oxide electrolyser |
| SOEC: | solid oxide electrolysis cell |
| SOFC: | solid oxide fuel cell |
| SRO: | short range ordering |
| TPB: | triple phase boundary |
| XPS: | X-ray photoelectron spectroscopy |

XRD: X-ray diffraction
YSZ: Yttria stabilized Zirconia

Nomenclature

| | | |
|-----------------|-------------------------|--|
| $\%MH$ | – | molar steam content |
| a | Å | lattice parameter |
| $a_{Ni(OH)_x}$ | – | activity of volatile Ni(OH) _x species |
| d | – | dimensions of particle growth |
| D_0 | $\frac{m^2}{s}$ | pre-exponential diffusion factor |
| d_{Eff} | m | equivalent thickness of dense YSZ layer |
| d_M | m | thickness of mesh |
| $d_{Ni-depl}$ | m | thickness of Ni depleted layer |
| d_W | m | mesh wire diameter |
| d_{YSZ} | m | thickness of YSZ electrolyte |
| $D_{Y,YSZ}$ | $\frac{m^2}{s}$ | temperature dependent diffusion constant for Y ³⁺ in YSZ |
| DR_r | $\frac{1}{s}$ | resistance degradation rate |
| DR_u | $\frac{1}{s}$ | voltage degradation rate |
| E_D | J | activation enthalpy of diffusion |
| F | $\frac{A \cdot s}{mol}$ | Faraday Constant |
| g | $\frac{m^3}{m^{-d}}$ | particle geometry factor |
| i | $\frac{A}{m^2}$ | current density |
| m | – | growth mode parameter |
| \dot{N} | $\frac{1}{s \cdot m^3}$ | rate of nucleus formation |
| N_0 | $\frac{1}{s \cdot m^3}$ | temperature independent nucleation rate |
| $n_{A,Sr}$ | – | A-site occupancy of Sr |
| OCV | V | open circuit voltage |
| p_{H_2} | Pa | partial pressure of H ₂ |
| p_{H_2O} | Pa | partial pressure of H ₂ O |
| Q_N | J | activation energy for atoms jumping through the matrix nucleus interface |
| \dot{Q}_{rev} | $\frac{J}{s}$ | reversible heat generation |

| | | |
|--------------------|-------------------------|--|
| R | $\frac{J}{mol \cdot K}$ | universal gas constant |
| r_0 | $\Omega \cdot m^2$ | initial area specific resistance |
| r_O | \AA | ionic radius of oxygen-ions |
| r_A | \AA | ionic radius of A-site cations |
| r_B | \AA | ionic radius of B-site cations |
| R_{eff} | $\Omega \cdot m^2$ | additional resistance of the Ni-depleted layer |
| R_{ohm} | $\Omega \cdot m^2$ | ohmic resistance |
| r_t | $\Omega \cdot m^2$ | area specific resistance at time t |
| R_{YSZ} | $\Omega \cdot m^2$ | ohmic resistance of YSZ electrolyte |
| t | s | time |
| t_{Gold} | – | Goldschmidt tolerance factor |
| T | K | temperature |
| U_0 | V | initial operating voltage |
| U_{Nernst} | V | Nernst potential |
| U_t | V | operating voltage at time t |
| V_M | m^3 | volume mesh layer |
| V_W | m^3 | volume mesh wire |
| Y | m^3 | volume of particle |
| z | – | charge number |
| Z | – | perovskite deficiency |
| α | $^\circ$ | lattice cell angle |
| β_{YSZ} | – | volume fraction of YSZ in hydrogen electrode |
| ΔH | $\frac{J}{mol}$ | reaction enthalpie |
| ΔG^* | $\frac{J}{mol}$ | critical free energy for nucleus formation |
| ΔE | $\frac{J}{K \cdot mol}$ | reaction entropy |
| ε_M | – | mesh porosity |
| η | V | overpotential |
| $\mu_{O^{2-},YSZ}$ | $\frac{J}{mol}$ | chemical potential of oxygen ions within YSZ |
| v | $\frac{1}{s}$ | growth velocity |
| ρ_W | m | mesh opening size |
| τ_{YSZ} | – | tortuosity of YSZ in hydrogen electrode |
| χ_{H_2} | – | mole fraction of H ₂ |
| χ_{H_2O} | – | mole fraction of H ₂ O |

1 Introduction

The transition to a more renewable electricity generation is accompanied by the challenge of an increasing mismatch between production and demand, which leads to a growing electric energy storage (EES) demand.[1] The need for storage technologies is further driven by the increasing importance of off-grid EES systems such as batteries for electrical vehicles.

There is a variety of different EES technologies each with individual specifications which make them desirable for different applications. Fig. 1 offers an overview of several EES technologies concerning typical power output, capacity values and discharge times. Rotation mass of generators and pumped hydro energy storage present the majority of Germany's grid integrated EES systems and compensate for short (0.1 s – 15 min) and medium term (15 min – 12 h) peaks. Considering the topographical limitation for pumped hydro storage it becomes obvious that current systems need to be complemented by technologies with larger capacities if weekly or longer fluctuations like “dark calms”¹ are to be managed.[2, 3]

The transformation of electric to chemical energy for storage has the largest capacity potential of known EES technologies. Water electrolysis is one example and refers to the electrochemical production of hydrogen from water using electricity. Its large potential is based on the fact that hydrogen – the most common element – is used as storage species and that the storage unit can be scaled independently of the transformation device. Furthermore, the already existing natural gas network presents an extensive infrastructure for storage and transportation, where a certain share of hydrogen can be introduced directly. Its full nominal capacity of approximately 200 TWh can be accessed by processing hydrogen to synthetic natural gas.[2]

The drawbacks of water electrolysis are its high cost and comparably low round-trip efficiencies, considering electrochemical hydrogen production in an electrolyzer (charging) and re-electrification in a fuel cell (discharging).[4] However, especially one type

¹ Refers to a period with low photovoltaic (dark) and little wind power production (calm). Typically, in central Europe such weather phenomena do not last longer than three weeks.[3]

of electrolyzer – the solid oxide electrolyzer (SOE) – has potential for very high conversion efficiencies, which can be increased even further by integration of a waste heat source. Its high operating temperature however, leads to several degradation processes thus limiting its lifespan. This issue needs to be addressed in order to ready this technology for large scale implementation.

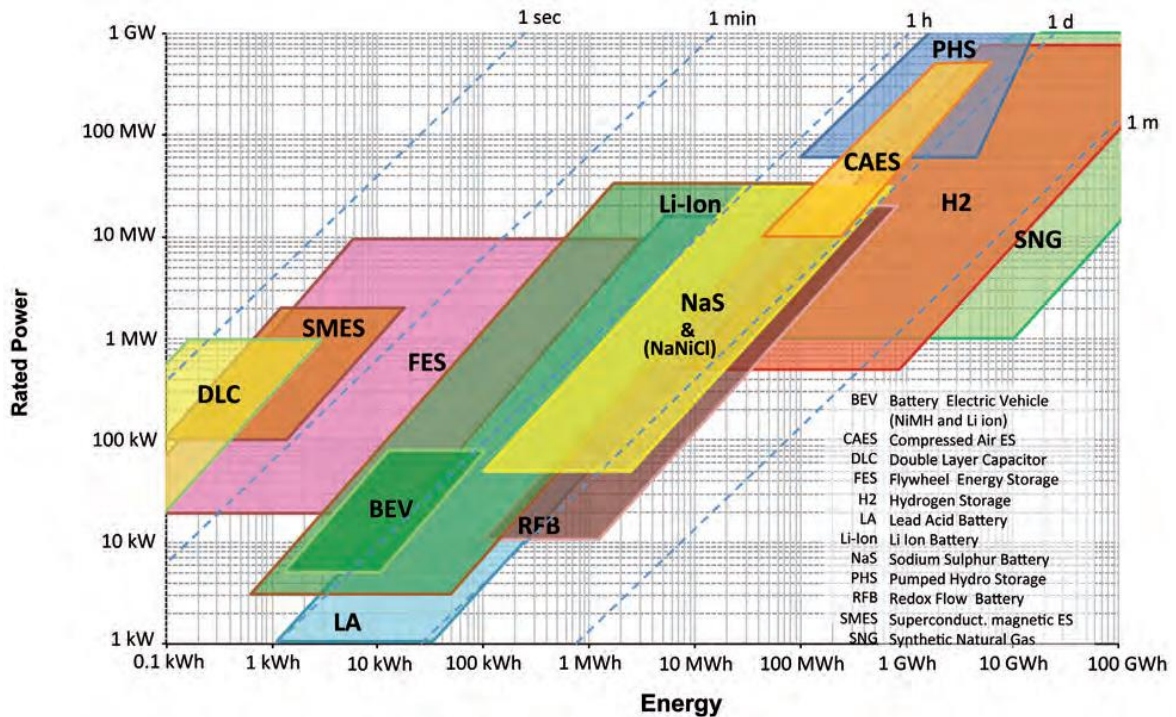


Fig. 1: Overview of typical power output, capacity values and discharge times for several EES systems [2]

1.1 Scope of the present dissertation

The centerpiece of this dissertation is a systematic study investigating the correlation between degradation of solid oxide electrolyzer cells (SOEC) and major operating parameters. A test matrix for a total of 20 comparable 1000 h degradation experiments was executed in order to isolate the impact of operating temperature, hydrogen gas humidity and current density. In-situ results are substantiated by post-test analyses allowing establishing connections between decrease in electrochemical performance and changes occurring in the cells. To complete this work a physico-chemical model is applied to provide a detailed understanding of processes limiting cell performance. Based on this knowledge it is used to elucidate degradation findings.

In literature there exist no degradation studies systematically investigating the influence of key operating parameters like the present work. A comparison of different studies to gain detailed information on parameter dependence is generally tricky as different studies generally diverge in several parameters. Knowing the parameter dependence of degradation processes however, is a powerful tool in understanding their underlying mechanisms. Furthermore, it allows the separation of otherwise undistinguishable degradation contributions.

1.2 Outline of the present dissertation

This dissertation is structured as follows:

- Section 1 and 2 provide fundamental information on SOEC technology and a literature overview over the current state of knowledge on SOEC degradation.
- Section 3 describes the scientific concept of this study and subsequently gives detailed information on experimental as well as theoretical techniques applied.
- Section 3.4 dedicates itself to cell characterization. This includes microstructural properties, electrochemical performance and separation of individual rate limiting processes. Furthermore, a physico-chemical model is parameterized in reference to a series of measurements and model reduction studies are provided.
- Section 5 presents the degradation findings. In-situ as well as post-test results are shown, parameter dependencies explained and mechanisms discussed. This section is divided into subsections according to separability of electrochemical impedance spectroscopy (EIS), i.e. degradation of ohmic resistance, oxygen electrode polarization, hydrogen electrode polarization and gas diffusion and conversion.
- Section 6 and 7 conclude the thesis and suggests consecutive studies.

2 Scientific and Technological Background

2.1 Solid oxide electrolysis cell

The term electrolysis describes a method in which an electrical current is used to facilitate an endergonic electrochemical reaction. Production of hydrogen and oxygen via electrochemical water splitting reaction is one example:



There are several types of electrolyzers each with different advantages and at different stages of development. The SOEC is one of them owing its name to the ceramic nature of its electrolyte. It is sometimes also referred to as high temperature electrolysis for its typical operating temperature between 700 °C and 1000 °C. However, this term is ambiguous and is also used for other electrolysis techniques.

While research on SOE has intensified during the last decade the cells used for SOE are commonly based on solid oxide fuel cell (SOFC) materials and architectures.[5] Consequently, up to now there are hardly any books focusing solely on SOEC, while the general electrochemical principle and information on materials and designs can be extracted from SOFC fundamental literature.[6, 7] The following paragraphs will therefore only briefly summarize SOEC fundamentals.

2.1.1 Functional principle

A schematic depiction of SOEC functioning principle is displayed in Fig. 2. An applied external current induces the reduction of water at the hydrogen electrode (cathode) forming gaseous hydrogen and oxygen ions. The latter pass through the ion conducting while electronically insulating and gastight electrolyte to the oxygen electrode (anode) and are oxidized there to form gaseous oxygen. The released electrons are connected to the electrical power source to complete the electrical circuit.

This means that in water electrolysis the redox reaction of equation (2-1) is split into oxidation and reduction reaction occurring at oxygen and hydrogen electrode, respectively, according to the following equations:

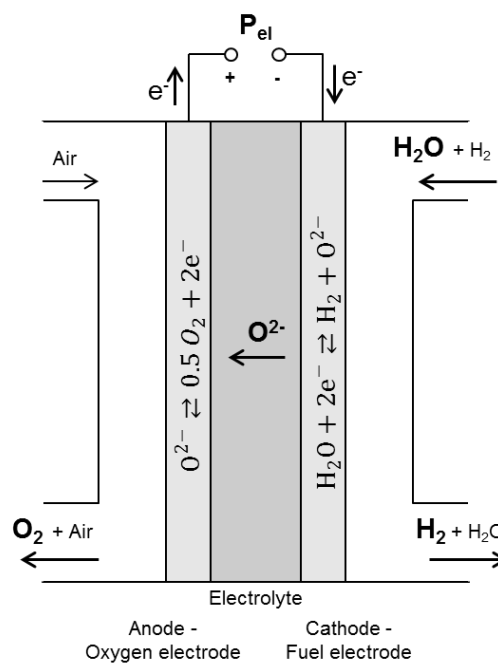
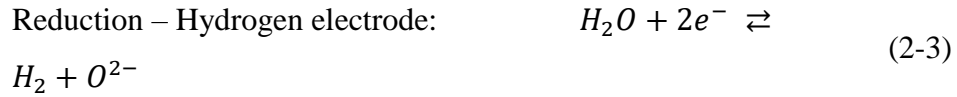


Fig. 2: General principle of a solid oxide electrolysis cell.

2.1.2 Cell architectures and materials

There are mainly two geometries for SOECs. The tubular design exhibits good mechanical stability and sealing properties, while the planar design is advantageous in terms of power density and manufacturing cost.[8, 9] Cell architecture depends on the layer providing mechanical support. Electrolyte supported cells (ESC) provide good mechanical robustness at the cost of high ohmic resistance and therefore require high

operating temperatures. To overcome this oxygen electrode (CSC²) and hydrogen electrode supported cells (ASC²) were developed. However, both electrode supported designs exhibit inherent problems, namely high electronic resistance and low redox stability. By introducing a metal support to the cell (MSC) many limitations of the previous cell architectures can be overcome.[10] However, new challenges concerning manufacturing and long term chemical stability arise.

The solid oxide cell (SOC) electrolyte has to provide sufficient ionic but low electronic conductivity, while being chemically stable in both reducing and oxidizing atmospheres. ZrO₂ doped with typically 8 mol% Y₂O₃ (8YSZ³) provides good overall properties. While other candidates such as Sc₂O₃ doped ZrO₂ (ScSZ) show higher ionic conductivities, 8YSZ remains today's most widely applied and proven electrolyte material.

A porous cermet of Ni and 8YSZ is most commonly used as hydrogen electrode. In this system Ni fulfills the function of catalyst as well as electronic conductor, which is why the Ni phase has to be connected in a percolation network. The 8YSZ backbone provides ionic conductivity. The charge transfer reaction can only occur at the so called triple phase boundary (TPB), where gas phase, electronic conductor and ionic conductor meet. Consequently the electrode's microstructure has great influence on performance and durability.[11]

There are two categories of materials typically used as oxygen electrode. Predominately electronic conducting materials such as La_{1-x}Sr_xMnO_{3-δ} (LSM) need to be mixed with an ionic conductor – typically the electrolyte material – forming a porous layer. Analog to the hydrogen electrode's cermet in this setup the electrochemical reaction occurs at the TPB, thus limiting performance. Materials with good ionic as well as electronic conductivities (MIEC) such as La_{1-x}Sr_xCo_{1-y}Fe_yO_{3-δ} (LSCF) are not limited to the one dimensional TPB but provide reaction sites all over its surface, resulting in a signif-

² The abbreviations CSC and ASC originate from SOFC terminology and refer to cathode- and anode supported cell, respectively.

³ The abbreviation translates into Ytria stabilized Zirconia. This name describes the fact that sufficient Ytria doping levels stabilize the cubic phase of YSZ down to room temperature. This is desirable as phase changes and the accompanying volume changes could result in mechanical stress or even failure. Additionally, the cubic phase provides highest ionic conductivity.

icantly higher performance. However, LSCF was reported to have higher degradation rates.[12] Furthermore, LSCF is reactive towards YSZ forming an insulating SrZrO_2 layer at the electrode | electrolyte interface. Therefore a diffusion barrier layer, typically $\text{Ce}_{0.9}\text{Gd}_{0.1}\text{O}_{1.95}$ (CGO) has to be introduced.[13, 14]

2.2 Advantages of solid oxide electrolysis

Solid oxide electrolysis has several advantages. Its high operating temperatures induce rapid reaction kinetics. The resulting low overpotentials translate into high conversion efficiencies.

Further advantages can be explained by thermodynamic considerations of the water electrolysis reaction as presented in Fig. 3. In order to facilitate better relation to cell operation each energy value ΔH was additionally translated into the corresponding voltage U according to

$$U = \frac{\Delta H}{F \cdot z} \quad (2-4)$$

with Faraday constant F and number of electrons participating in the reaction z . It reveals that the portion of the reaction enthalpy which needs to be supplied as electrical energy decreases with increasing operating temperature while the thermal energy demand increases accordingly. Consequently, an increasing amount of heat generated during operation due to internal resistances can be used directly to satisfy total energy demand. As a result conversion efficiencies of virtually 100 % can be achieved on cell level while maintaining appreciable reaction rates. . The step in reaction enthalpy in Fig. 3 at 100 °C represents the reduced amount of energy which has to be provided by the fuel cell if water is provided in gaseous form. Consequently, the conversion efficiencies on system level can be largely increased, if a waste heat source is available at sufficiently high level to evaporate the reactant water.

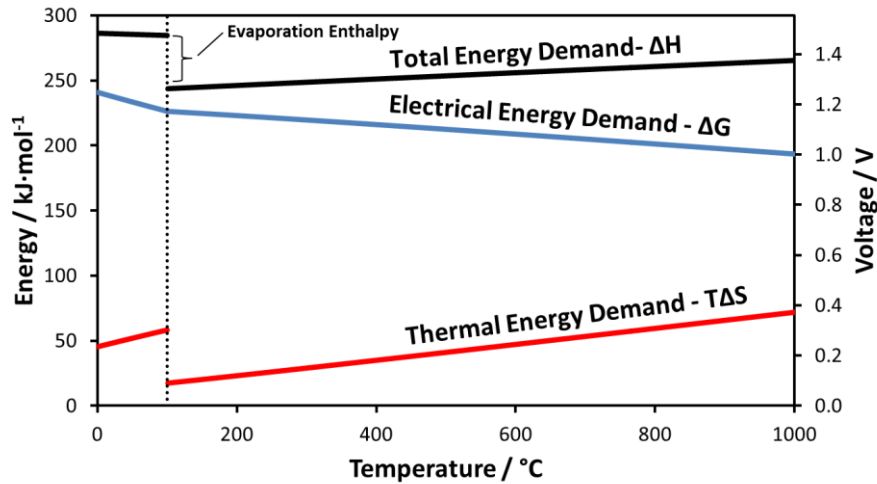


Fig. 3: Energy demand for water electrolysis as a function of temperature at standard pressure.

Depending on the overall overpotential a SOEC can be operated in three different modes. If the operating voltage surpasses the total energy demand, i.e. that the overvoltages exceed the thermal energy demand the cell runs in exothermic mode, while a cell voltage below the total energy demand results in endothermic operation. If the cell voltage matches the total energy demand which is approximately 1.3 V at typical operating temperatures the cell works in thermo-neutral conditions. This is desired for system application as it reduces system complexity, while operation above and below thermo-neutral conditions can be deliberately used to adjust system temperature.

Furthermore, SOEC exhibits reactant flexibility. Apart from H₂O also CO₂ can be electrolyzed. While it is possible to do so with pure CO₂ more commonly co-electrolysis of a mixture of H₂O and CO₂ is realized. The resulting mixture of H₂ and CO called forming gas can be used to subsequently synthesize a variety of hydrocarbons following the Fischer-Tropsch process. More recently the idea of co-electrolysis coupled with internal hydrocarbon synthesis arose [15].

2.3 Degradation rate terminology

The above presented advantages clearly illustrate the potential of SOEC. However, the high operating temperatures also pose challenges such as unwanted side reactions or thermal stress. These phenomena generally deteriorate cell performance – the cells degrade.

In literature degradation rates are typically presented as a relative increase in operating voltage averaged over a certain time, according to

$$DR_U = \frac{(U_t - U_0)}{U_0 \cdot t} \quad (2-5)$$

with the voltage degradation rate DR_U , the initial operating voltage U_0 and the operating voltage U_t at time t . It is commonly presented in the format [% / 1000 h]. While this parameter offers an easy way to evaluate system longevity, it should be treated carefully when comparing different measurements. It is the author's opinion that for fundamental analysis degradation should be defined as increase in resistance. Analog to the voltage degradation rate DR_U the degradation rate DR_r based on the increase in resistance can be calculated as

$$DR_r = \frac{(r_t - r_0)}{r_0 \cdot t} \quad (2-6)$$

with the area specific resistance r_0 and r_t initially and after time t , respectively. This approach only works if a linear polarization curve can be approximated. Otherwise the differential resistance $dr(i)$ has to be used.

The relation between operating voltage U and area specific resistance r is given as

$$U(t) = U_{Nernst}(t) + r(t) \cdot i(t) \quad (2-7)$$

with the Nernst potential U_{Nernst} , and the current density i . Under galvanostatic conditions and constant gas feed the voltage degradation rate DR_U can therefore be calculated in relation to the initial and final overall resistance, by

$$DR_U = \frac{(r_t - r_0) \cdot i}{(U_{Nernst} + r_0 \cdot i) \cdot t} \quad (2-8)$$

A comparison between equations (2-6) and (2-8) reveals the difference in reporting degradation based on increase in operating voltage or overall resistance. Generally, DR_r can be compared unambiguously between different measurements, as it only reflects the relative increase in resistance. DR_U on the other hand is additionally influenced by the gas mixtures via the Nernst potential and the current density applied. This can lead to the irritating situation that the voltage degradation rate of a sample is larger relative to another sample even though its resistance degradation rate is lower – since it is operated at higher current density or at higher p_{H_2O} / p_{H_2} ratio.

2.4 Literature review on SOE degradation

A multitude of studies investigating SOE degradation on cell as well as stack-level arose during the past decade. The main difference can be found in stack specific additional degradation contributions, namely deterioration of interconnect contact and pollution from tubing and interconnects. Consequently, stack degradation is commonly found to be higher than cell degradation.[16] However, this work is focusing on degradation phenomena on cell level which is why stack specific degradation is out of the scope of this dissertation.

Generally, at cell level a wide range of degradation rates has been reported. One of the lowest degradations was observed by Schefold et al. for a single cell operated at -1 A/cm^2 and approximately $780 \text{ }^\circ\text{C}$ for 9000 h.[17] They observed a linear increase in operating voltage until approximately 7600 h, when hardware malfunction caused a significant voltage step. The mean voltage degradation rate DR_U during this time amounted $3 \text{ \%}_U/\text{kh}$, which translates into a DR_R of $18 \text{ \%}_R/\text{kh}$ for the given experimental details.⁴ Several other studies show degradation rates as high as $DR_U > 10 \text{ \%}$ corresponding to DR_R of $50 \text{ \%}_R/\text{kh}$ and above.[18–21] The situation is furthermore complicated as degradation often progresses nonlinear, especially within the first hundred hours, making the description of degradation as a summarized value less useful.[18, 20, 22] Additionally, the mode of operation plays an important role towards degradation rate. A recent study over several hundred hours of cell operation published by Graves et al. shows that cell degradation can be largely prevented by alternating between electrolysis and fuel cell operation.[23]

This brief overview of overall degradation rates reveals that degradation is of great concern for SOEC viability, while a detailed investigation of underlying processes is required to understand and finally mitigate performance deterioration. The following section gives an overview over previously observed SOEC degradation phenomena and provides explanations to the current state of knowledge. This overview is limited to mechanisms and studies relevant to the cell composition used in this study, namely Ni/YSZ | YSZ | CGO | LSCF for hydrogen electrode, electrolyte, diffusion barrier layer

⁴ In order to calculate the resistance degradation rate the overall Nernst potential was approximated as mean of inlet and outlet Nernst potential.

and oxygen electrode, respectively. As mentioned above stack degradation is an important and decisive issue which, however, is out of the scope of this work.

2.4.1 Hydrogen electrode degradation

Processes reported on hydrogen electrode degradation can be divided into two categories. On the one hand the Ni phase exhibits microstructural changes at typical SOEC operating conditions. On the other hand the hydrogen electrode Ni/YSZ cermet was shown to be sensitive to impurities.

The generally higher hydrogen gas humidities in electrolysis operation compared to typical fuel cell conditions leads to a group of degradation mechanisms. These are based on the volatility of Ni in water vapor rich atmospheres to form Ni(OH)_x species, like Ni(OH)_2 . Jiao et al.[24] showed a correlation between morphological changes to a porous Ni phase and hydrogen gas humidities even under low humidification ranging from dry conditions to a steam content of 30 %MH. Furthermore, they revealed the influence of the gas concentration gradient forming at the TPB under current locally increasing Ni mobility. They suggested a combined underlying mechanism of humidity enhanced surface diffusion and vaporization–deposition process of volatile Ni species.

Coarsening of Ni microstructure can be one effect resulting in a decreased electrode performance. This was shown by several studies at moderate humidities of approximately 50 %MH.[18, 25]

Under extreme conditions of 950 °C, 90 %MH and 2 A/cm² another phenomenon was observed by Hauch et al.[18]. They observed Ni “filling up” the porous phase close to the electrolyte leading to a dense layer composed of Ni and YSZ. This was explained by the transport of volatile Ni species along the gas concentration gradient towards the most reducing conditions, i.e. the hydrogen electrode | electrolyte interface. Simultaneously, an increase of the ohmic resistance by a factor of three was recorded, which was attributed to the electrochemical deactivation of the formed dense layer resulting in an effective increase in electrolyte thickness.

More recently a seemingly reverse trend of Ni migration was observed in several studies.[11, 26, 27] Post mortem measurements revealed that the first few micrometers of the hydrogen electrode closest to the electrolyte were completely depleted of Ni. The remaining porous YSZ layer is electrochemically inactive for the charge transfer reac-

tion. Similar to the previously described phenomenon the shift of the active reaction zone away from the dense electrolyte layer results in an additional contribution to the ohmic resistance. Its impact is depending on porosity and tortuosity of the electrode's YSZ backbone leading to significant resistances even for thin layers. While the mechanism for this process is not yet fully understood Mogensen et al. proposed a hypothesis suggesting that Ni particles become isolated thus leading to a gradient in activity of volatile Ni species[28] which will be explained in more detail in chapter 5.1.1, while a study by Hauch et al. identified the overpotential as a driving force.[11]

Impurities were shown to have an influence on hydrogen electrode performance.[18] Silica poisoning is very common and typically originates from glass sealants or as an inherent contaminant of the YSZ powder.[18, 29, 30] Under typical SOEC operating conditions the presence of SiO_2 leads to a significant Si(OH)_4 vapor pressure, causing degradation due to its corrosive nature.[31] The Si(OH)_4 vapor pressure was shown to increase with increasing temperature, humidification and current density.[21] Due to the gas concentration gradient impurities accumulate at the TPB hindering accessibility and increasing electrode polarization resistance. Operating the cell in fuel cell mode thus reversing the gas concentration gradient can partially remove impurities and reactivate the cell, as shown by Hauch et al.[19]

2.4.2 Oxygen electrode degradation

Most studies reported in literature were conducted on cells using LSM/YSZ composite as oxygen electrode.[16, 32] Microstructural deterioration finally leading to the delamination of the electrode from the electrolyte is a commonly observed phenomenon for this system.[22, 30, 33, 34] Virkar developed a model revealing that in electrolysis very high oxygen pressures can occur at the interface between oxygen electrode and electrolyte or even within the electrolyte close to the interface. The high oxygen pressure builds up in pores and cavities until finally the limit of mechanical stability is reached and cracks are formed. The quantity of oxygen partial pressure as well as its location is depending on several material as well as operating parameters. It was shown that high current densities leading to high oxygen electrode overpotentials drive electrode delamination. Virkar's model furthermore predicts that the introduction of minor electronic conductivity of the electrolyte can significantly decrease the potential for delamination. However, this is undesirable as it inevitably reduces faradaic conversion

efficiency. Furthermore, the electrode's microstructure and its processing play an important role.[18]

The problem of delamination can largely be overcome by employing a mixed ion-electron conductor like LSCF, avoiding the oxygen pressure build up at the interface of ionic and electronic conductor.[17, 35] Additionally, the generally higher activity of LSCF compared to LSM electrode reduces electrode's overpotential. Furthermore, for MIECs the charge transfer reaction is not limited to the TPB as for LSM /YSZ composite electrode. This makes it less prone to impurity blocking of the reaction site and the subsequent build-up of oxygen partial pressure.[36]

An additional degradation phenomenon often observed is the formation of Cr containing secondary phases. This is of large concern on stack level due to commonly Cr containing stainless steel interconnects. However, even for single cell experiments it is still relevant as there might be other Cr sources such as tubing or connects. Within the oxygen electrode Cr reacts to block the TPB in case of a LSM/YSZ electrode, while in case of LSCF it forms insulating layers.[37–40]

Tietz et al. observed after 9000 h of operation a “broadening” of the original XRD reflections of LSCF in stack operation “towards lower angles” as well as very low intensity peaks corresponding to Co_3O_4 . At the same time they observed gradients in intensity in BSE-SEM images of LSCF interpreting this as evidence for compositional changes.[41]

While there are few studies on LSCF degradation in SOEC mode, there is a much larger pool of studies on LSCF in fuel cell operation. A summary of these can be found in more detail elsewhere.[42, 43] The knowledge of degradation processes under SOFC conditions can be helpful, but its adoption to SOEC mode has to be undertaken very carefully as the difference in local oxygen partial pressure as well as the reversed current density have a significant effect on LSCF stability.[44] An example for this is the phenomenon of Sr segregation. While this is commonly reported for SOFC conditions[45, 46] the same does not appear to be the case in SOEC operation. A more recent study even indicates that positive polarization of the oxygen electrode leads to reincorporation of previously segregated Sr.[47]

2.4.3 Electrolyte degradation

YSZ is not chemically stable in contact with LSCF at typical operating conditions. It will react to form secondary phases with much lower ionic conductivity such as SrZrO_3 . In order to prevent this, a few micrometer thick diffusion barrier layer is introduced which is usually composed of CeO_2 doped with 10 mol% Gd (10GDC).[12, 48] While this adds an additional contribution to the internal resistance of the cell, the high performance of LSCF is generally considered to predominate.[49]

Several reports show that even if a 10GDC diffusion barrier layer is employed the formation of SrZrO_3 can still be observed. This is explained by cation transport through the barrier layer via grain boundary diffusion as well as surface diffusion along cracks.[50] Although 10CGO is not suitable to completely prevent the formation of secondary phases, it can be drastically delayed by a well manufactured dense layer.[50]

At high current densities (shown for 1 A/cm^2 and above) the YSZ electrolyte itself was shown to deteriorate. Pore formation along YSZ grain boundaries was observed close to the electrolyte | oxygen electrode interface [35, 41] and was found to be more severe at higher current densities and temperatures.[20] Jacobsen et al. observed that evolution of gaseous oxygen can occur within the grain boundaries under high polarization, by calculating the electromotive force of oxygen inside YSZ.[51] The accumulation of oxygen molecules at the grain boundaries significantly hinders oxygen ion transport. The resulting increase in ohmic resistance can thus be much larger than expected from post mortem analyses.[16] The generated pores along the grain boundaries can grow and finally form cracks in the electrolyte and weaken contact with the oxygen electrode.[33]

Additionally to the formation of pores along the grain boundaries, intragranular pore formation was also observed as a result of high current in front-like shapes parallel to the YSZ | CGO interface.[41] Tietz et al. explain this by the difference in YSZ cation mobility analog to the formation of “Kirkendall voids”[52, 53], while the removed material was found in form of a dense layer at the YSZ | CGO interface. Matus et al.[54] observed similar deterioration in the YSZ layer of an oxygen pump operated at 1045°C and 4.5 A/cm^2 . The authors suggest an explanation based on the mobility of interstitial oxygen and oxygen vacancies in an electrical or chemical gradient, resulting in agglomeration of complexes of Zr^{4+} and oxygen vacancies.

YSZ was also shown to exhibit an “aging effect”, i.e. a reduction of ionic conductivity with time. Kondoh et al. systematically investigated this phenomenon at different temperatures as well as different Ytria levels and summarized previous studies on the topic.[55, 56, 57 and references therein] They conclude that the most likely mechanism responsible is the formation of “short range ordering” of oxygen ion vacancies around Zr^{4+} ions, increasing their activation energy and thus decreasing the overall conductivity. There are more recent studies, which offer a different explanation and show that the phase transition from cubic to tetragonal can occur at typical SOC operation temperatures despite the fact that cubic 8YSZ is often considered to be fully stabilized down to room temperature.[58, 59]

The problem with interpreting electrolyte degradation phenomena is that no in-situ separation via EIS is possible. The situation is further complicated as degradation processes of other cell components like the previously described Ni depletion of the hydrogen electrode or a change in LSCF perovskite composition leading to a decreased electronic conductivity also manifest themselves in the ohmic resistance. Therefore it is not possible to quantify the contribution of each individual processes using solely singular EIS data and post-test analyses. This can easily result in misleading conclusions if an increase in ohmic resistance is readily attributed to observations which appear to be most severe in post mortem measurements.

3 Scientific Approach and Methodology

3.1 Experimental concept and scientific approach

As described previously there is a large pool of studies on degradation for SOFCs and a growing number concerning SOECs. However, it is difficult to combine these to a unified picture as there are always differences in experimental details. Divergence can be found in elemental topics like different cell architectures or compositions. Even larger are the possible discrepancies in operating conditions such as temperature, current density, gas compositions at each electrode, gas conversion rates, flow rates or operating times to name just a few. Additionally to the just mentioned variations in controlled experimental details there is a high chance for unintentional deviations such as purity of feed gases, principle and stability of humidification and cell housing design including sealing concept and quality. Furthermore, the cells inherently possess different properties depending on the details of cell manufacturing. All these differences hamper a detailed comparison of different studies with the aim of extracting information on the influence of operating parameters on degradation.

However, knowledge of this correlation can significantly increase the understanding of degradation in two major ways. It can give insight into the mechanism, kinetics and driving forces of known degradation phenomena, facilitating the development of strategies to mitigate them. Additionally, it offers the possibility to separate and identify degradation processes due to their different dependence on operating parameters which would otherwise be undistinguishable. This is of special significance for the ohmic resistance which comprises a large number of contributions as previously described. The relevance of this point will be demonstrated in detail by the results of chapter 5.1.

In order to establish a clear correlation between degradation processes and operating conditions a set of experiments was devised. Three parameters – namely the operating temperature, the current density and the hydrogen gas humidity – were chosen to be most revealing and the experimental matrix shown in Fig. 4 was devised to identify the influence of each parameter individually. All other parameters were kept constant for all degradation measurements. Furthermore, the problem of unintentional deviations between measurements could be largely overcome by conducting all experiment in the

same test rig and using highly reproducible commercially produced cells of the same batch.

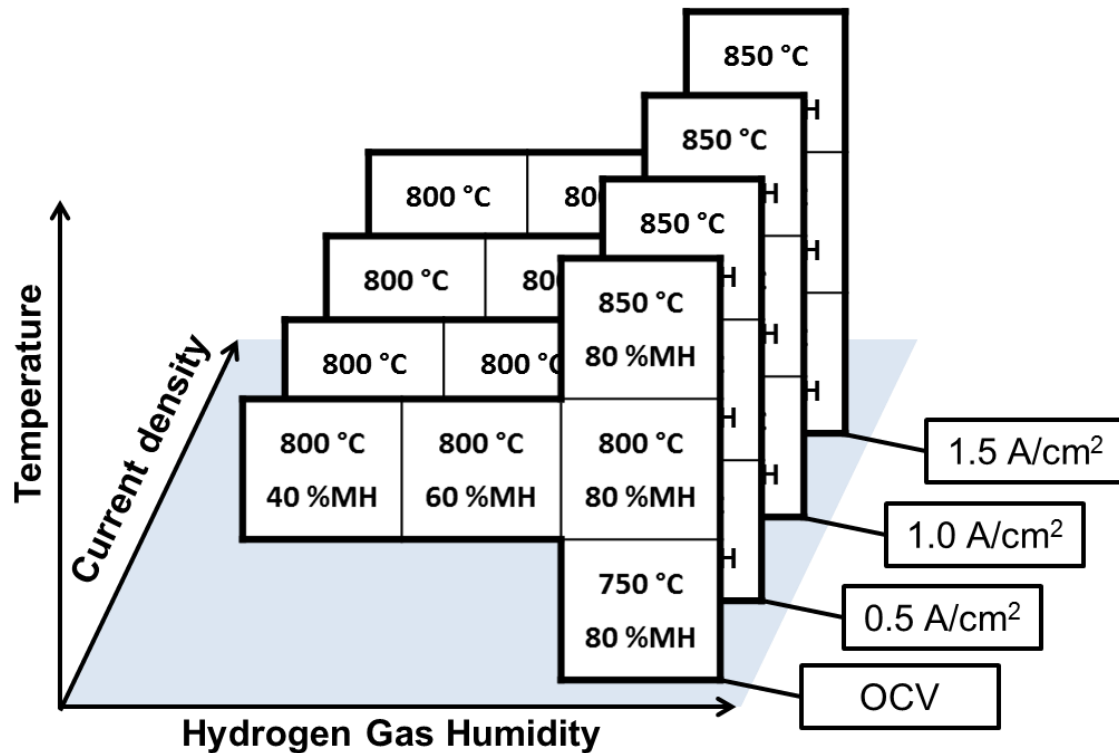


Fig. 4: Test matrix consisting of three temperatures, three humidities and four current densities devised to individually identify the influence of each investigated parameter on degradation processes. A 1000 h degradation experiment is conducted at each of the 20 presented combinations of operating conditions.

An alternative option to the presented test matrix would be a design of experiments (DoE) approach in which all investigated parameters (independent variables) are changed simultaneously between experiments. Their individual influence on the investigated changes (dependent variables) is extracted via statistical analysis of the data. There are, however, preconditions for this approach to provide reliable results which are difficult to meet in this study. For instance a strong non-linearity of dependencies – as it could i.e. be expected close to OCV – is problematic and would have to be previously known and compensated for by a large number of measurement points. Also, an unambiguous quantification of observed changes in the cells is difficult to achieve, especially when it comes to post-mortem analyses and gets additionally aggravated by statistical issues such as outliers. Furthermore, not all observed changes (dependent variables) were known in advance but rather a result of the conducted experiments. As a consequence, it was chosen not to follow a DoE approach but instead conduct the previously

described test matrix where changes in all investigated parameters can be analyzed individually.

A new cell was operated for 1000 h at each of the 20 parameter combinations displayed in Fig. 4. Fig. 5 exemplary shows the operation voltage's progression over the duration of the experiment for cells operated at 800 °C, 80 %MH and all four different current densities. In addition to an initial cell characterization the development of each cell's resistance was monitored by regular impedance spectroscopy measurements approximately every 168 h as indicated by the black vertical lines in Fig. 5. After operation a final characterization was conducted.

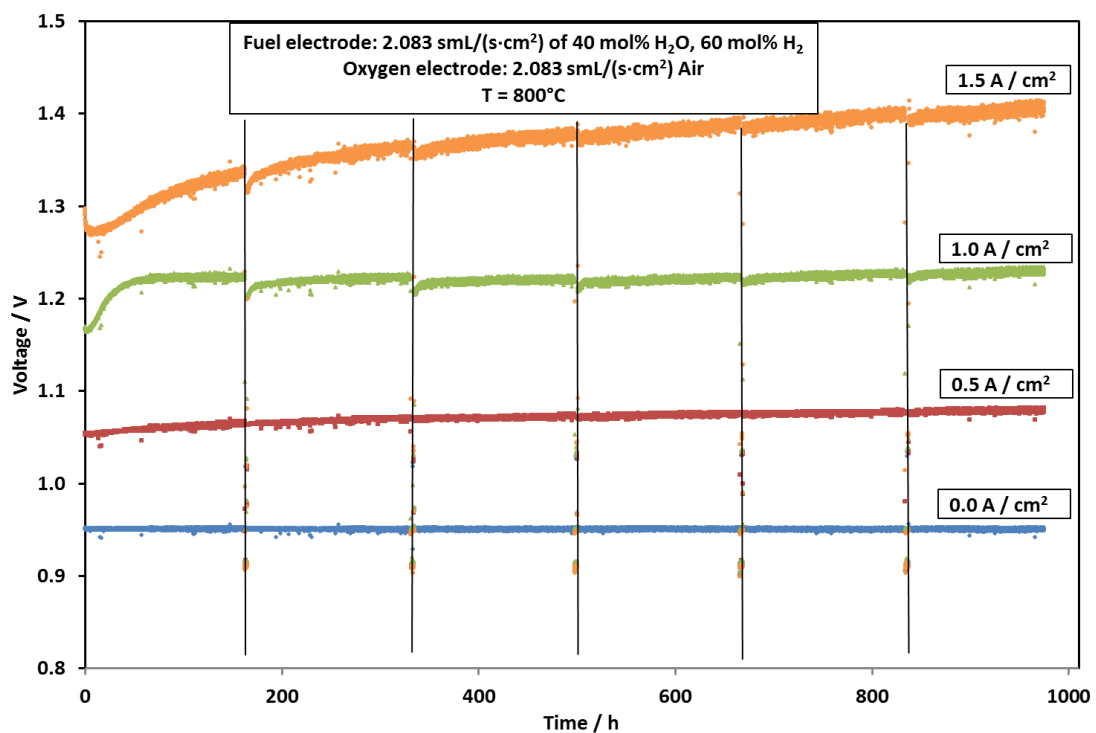


Fig. 5: Degradation experiment of four cells measured for 1000 h at 800 °C, 80 %MH and OCV, 0.5 A/cm², 1.0 A/cm² and 1.5 A/cm², respectively. The black vertical lines indicate the interruption of current for intermediate cell characterization by EIS measurements.

The gathered impedance data is used to distinguish between individual contributions of ohmic resistance, hydrogen electrode electrochemistry, oxygen electrode electrochemistry and gas diffusion and conversion, as exemplary shown in Fig. 6A for the cell operated at 800 °C and 80 %MH at OCV. The details of the impedance data analysis and interpretation will be described in chapter 3.4, while standard deviations of these measurements are given in Table 5 in chapter 4.2 based on cells in their initial state. For

better visualization of the individual degradation contributions the resistance values are displayed as absolute changes in resistance as plotted in Fig. 6B.

After operation each cell was examined by a range of post-test analyses. The coupled information of the observed in-situ degradation and the gathered information on parameter dependencies in conjunction with changes observed by post-test analyses allow for an enhanced identification and in-depth interpretation of the major relevant degradation processes occurring.

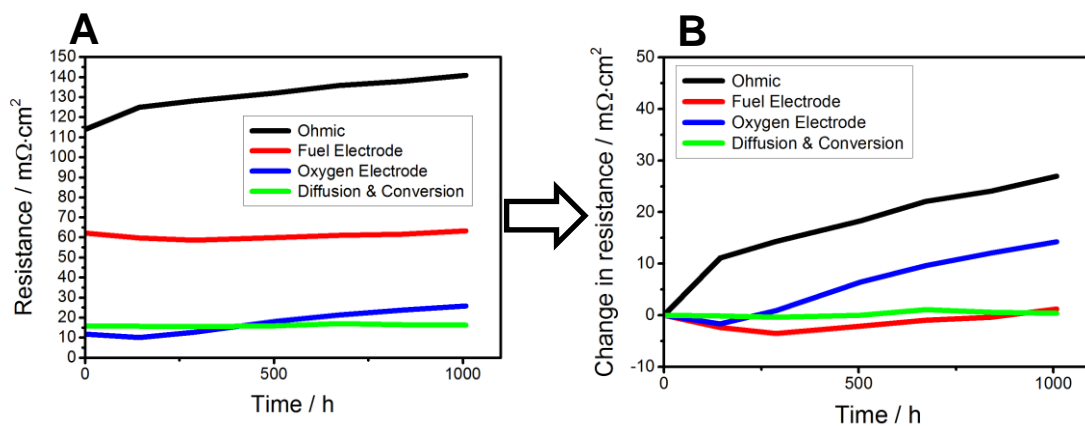


Fig. 6: (A) Progression of each individual resistance contribution during operation compared to (B) the absolute change of each individual resistance contributions. Both are exemplary shown for a cell operated at 800 °C and 80 %MH at OCV.

3.2 Experimental set-up

The following section describes the major experimental details. The author chose to give this topic some additional focus and offer detailed information on the experimental framework in the believe that this is important for comparing, reproducing or simulating the presented results as well as explaining possible discrepancies with other studies. Furthermore, it might be beneficial for people aiming at conducting similar experiments.

3.2.1 Test rig

For electrochemical operation a test rig with four test sites for reversible measurements of single cells was used. The test rig provides one gas mixture as feed for hydrogen- and oxygen electrode, respectively, which are consecutively split into four equal parts and supplied to each test site. The flow rate for all experiments was $2.08 \text{ mL}/(\text{s}\cdot\text{cm}^2)$ (standard milliliter per second and square centimeter). All test sites are symmetrically arranged inside one furnace. Consequently, cells measured during one experiment share the same default temperature, while deviations can originate from differences in current density or sealing quality. The current density for each cell could be controlled individually up to $1.5 \text{ A}/\text{cm}^2$ in electrolysis as well as fuel cell mode.

Temperatures were monitored by type-K thermocouples in designated holes at various positions inside the ceramic cell holders thus avoiding media contact. This was chosen as it prevents possible contamination of hydrogen- and oxygen electrode gases while avoiding the need for further sealants. Positions of thermocouples were chosen so that inlet and outlet gas temperature of the hydrogen electrode as well as the cell temperature could be monitored. The latter was measured by a thermocouple located centrally over the oxygen electrode and one millimeter inside the cell holder resulting in an approximate distance of 1.8 mm above the electrode including the contacting meshes. As this is the temperature measurement describing the actual cell temperature most accurately it is henceforth referred to as “cell temperature”.

3.2.2 Cell housing

For the measurement of hydrogen electrode supported cells a new cell holder was designed and implemented. Hydrogen electrode supported cells are commonly designed in a way that the oxygen electrode is smaller than the hydrogen electrode support and the electrolyte thus providing the electrolyte as a surface which can be used for sealing (compare Fig. 7). Due to the low ionic conductivity of the electrolyte any in-plane effects can be neglected so that the oxygen electrode' area can be considered as the active area of the cell. The challenge for any cell holder is to ensure good sealing quality between both hydrogen- and air-electrode as well as between hydrogen gas compartment and surrounding air. Conventionally, this is realized by introducing a sealing ceramic as depicted in Fig. 7B. The problem with this system is that the combined thickness of cell,

contacting meshes and gold ring have to be estimated accurately, in order to use a sealing ceramic of appropriate thickness resulting in sufficient sealing quality. This is especially delicate since the thickness of the meshes as well as of the gold ring decreases during heat up procedure. As consequence, the sealing between hydrogen gas compartment and surrounding air is often improved by introducing silica based sealing materials. The newly designed cell holder concept avoids this by arranging both sealing surfaces in a perpendicular orientation as shown in Fig. 7A. This leads to a series of advantages, among which are:

- One gold ring is sufficient for high sealing quality, thus eliminating the need for silica based sealing materials.
- The sealing works independent of thickness of cell and contacting meshes and compensates for settling of gold ring or contacting meshes.
- This cell holder design allows for independent weight load applied to shell, i.e. pressure on gold ring and oxygen electrode gas distribution unit (GDU), i.e. pressure on contacting meshes and cell.
- A reducing atmosphere all over the hydrogen electrode substrate is ensured, including electrochemically inactive parts of the cell, by providing space next to the substrate which is flushed with hydrogen electrode gas flow. (compare Fig. 7) This is crucial for hydrogen electrode supported cells as oxidizing conditions would lead to rapid disintegration of the cell.

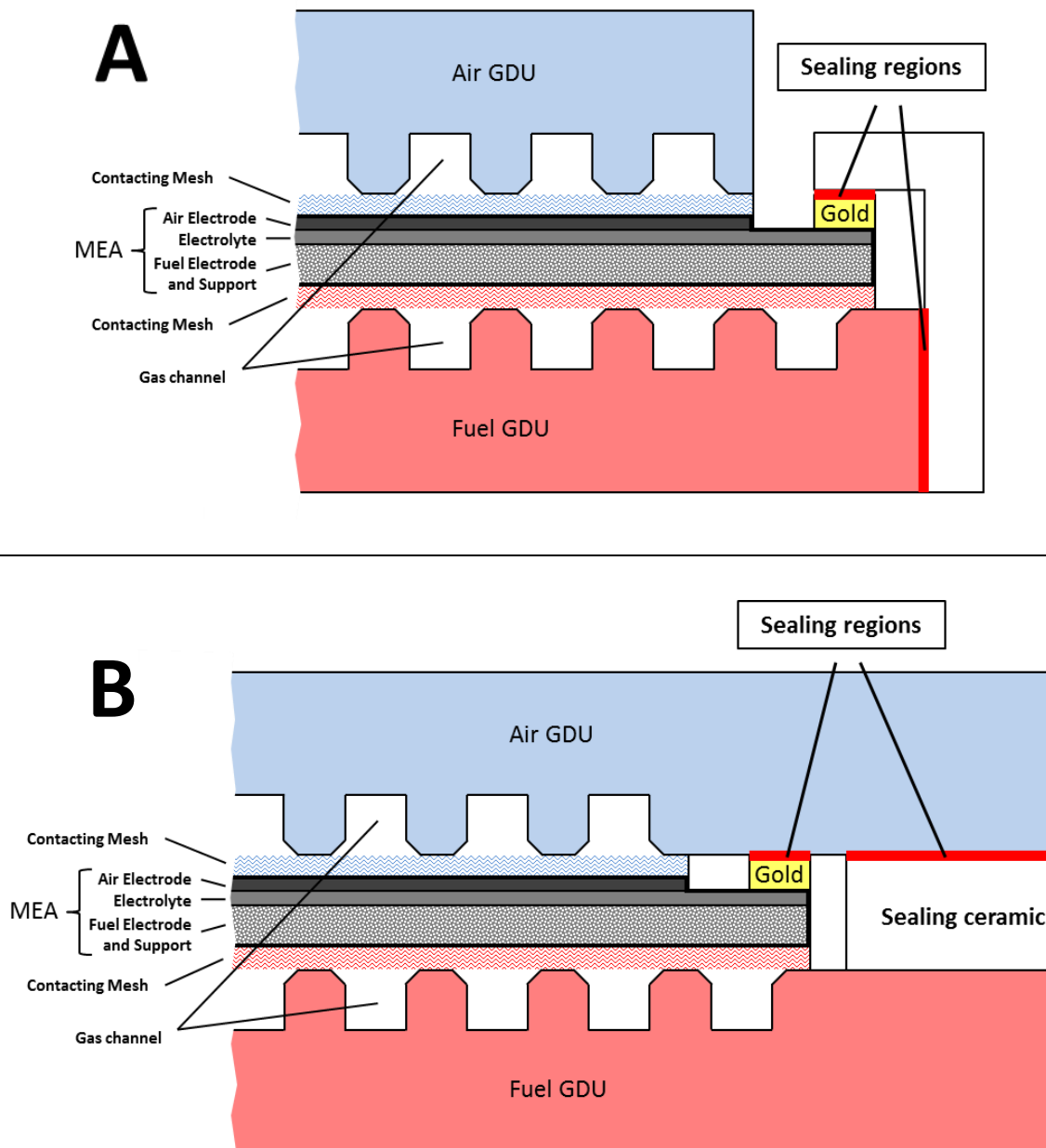


Fig. 7: (A) Sealing concept of implemented new cell holder design compared to (B) sealing principle of conventional cell holder designs.

The cells were contacted by different meshes. For the hydrogen electrode two layers of a Ni-mesh were used. Since the hydrogen electrode substrate provides good electronic conductivity a comparatively coarse mesh was chosen with a wire diameter d_W of 0.1 mm and an opening size ρ_W of 0.225 mm. According to equation (3-1) this results in a mesh porosity ε_M of approximately 0.76.

$$\varepsilon_M = 1 - \frac{V_W}{V_M} = 1 - \frac{\frac{2}{(d_W + \rho_W)} \cdot \left(\frac{d_W}{2}\right)^2 \pi}{2d_W} \quad (3-1)$$

With V_W and V_M as volume of mesh wires and porous mesh layer, respectively. This equation is based on the assumption that the thickness of the mesh d_M equals twice the diameter of the single wire, assuming that the mesh's ductility under pressure is sufficient to force the interlacing wires to touch, however resulting in no deformation of the wire cross-section.

$$d_M = 2d_W \quad (3-2)$$

The oxygen electrode was contacted by a series of Pt meshes: one fine, two medium and two coarse ones with a wire thickness of 0.04 mm, 0.076 mm and 0.12 mm and an opening size of 0.125 mm, 0.24 mm and 0.5 mm, respectively. The parameters for all used meshes can be found in Table 1.

| | d_W | d_M | ρ_W | ε_M | Material |
|---------------------------|-------|-------|----------|-----------------|----------|
| Hydrogen-electrode | 0.1 | 0.2 | 0.225 | 0.76 | Ni |
| Oxygen-electrode (coarse) | 0.12 | 0.24 | 0.5 | 0.848 | Pt |
| Oxygen-electrode (medium) | 0.076 | 0.152 | 0.24 | 0.811 | Pt |
| Oxygen-electrode (fine) | 0.04 | 0.08 | 0.125 | 0.810 | Pt |

Table 1: Parameters of contacting meshes

3.2.3 Humidification

The hydrogen gas humidification (henceforth solely referred to as “humidity”) was implemented with a “Controlled Evaporator Mixer” (CEM) in combination with a liquid water mass flow controller (Cori-Flow™, Bronkhorst, Netherlands). A flow of liquid water is being pressed through a nozzle by a gas stream resulting in a spray dispersed in the carrier gas. This mist is lead into a heated chamber which temperature is sensitive and has to be chosen high enough for all droplets to evaporate before touching the chamber walls and low enough to evaporate homogeneously. It therefore has to be controlled precisely and evenly. This is of great importance in order to achieve a stable water vapor supply and consequently stable cell voltages.

Carrier gas and liquid water supply can be controlled individually. However, there are limitations to the ratio. For the desired flow rates a maximum humidity of a little

over 80 %MH and a minimal humidity of 4 %MH can be realized. In this study only H_2 was used as carrier gas so that for all measurements a mixture of only hydrogen and water vapor are applied as hydrogen electrode gas.

3.2.4 Impedance spectroscopy measurement

Impedance spectroscopy measurements are the main source of in-situ monitoring of the cells during the experiments. These were conducted using an “IM6 A-level electrochemical workstation” as frequency generator and frequency response analyzer in combination with a “PP240 external potentiostat” (both from Zahner, Germany). Measurements were conducted in galvanostatic mode with a root mean square value of the AC current stimulus of 200 mA or 500 mA. This was chosen so that the maximal resulting root mean square value of the voltage was approximately 10 mV or lower. The recorded frequency typically ranged from 500 mHz to 100 kHz, but was adjusted to lower frequencies if necessary. All impedance spectroscopy measurements were conducted under stable conditions, i.e. temperature, gas flows, etc. were virtually constant.

Data quality was validated according to the Kramers-Kronig relations. The test was conducted using the program Lin-KK which is based on Boukamp’s idea [60] and refined by Schoenleber.[61, 62] A representative calculation of residuals is displayed in Fig. 8 and shows that the impedance spectra recorded fulfill the three Kramers-Kronig conditions: causality, linearity and stability. The residual spike at 50 Hz likely originates from grid interference.

Distribution of relaxation times (DRT) was calculated with a modified Levenberg-Marquardt algorithm adapted from Ref.[63].

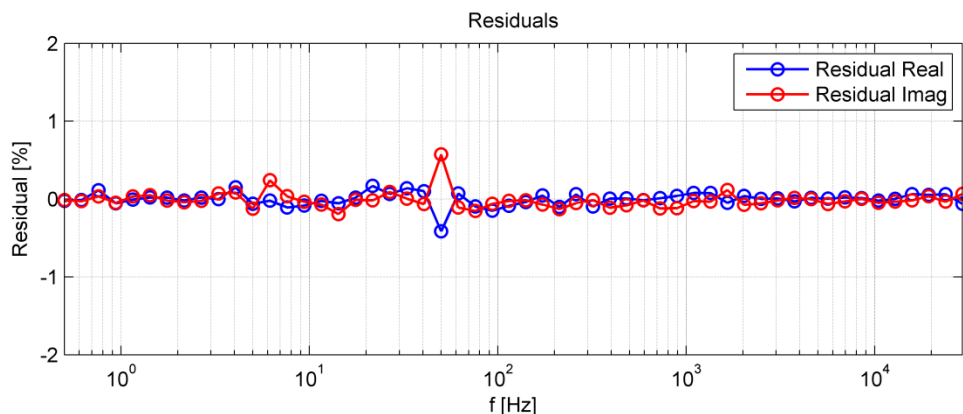


Fig. 8: Representative Kramers-Kronig test of a recorded impedance spectrum..

3.2.5 Heat-up, reduction, initiation and cool down

After being mounted the cells were heated up at a rate of approximately 3 K/min up to 900 °C. The heating rate was defined to limit thermal stress to the cells as well as the cell holders and ensure their integrity.

At 900 °C the cells were reduced according to the steps in Table 2. After a cool down to 800 °C the cells were initiated with a polarization-curve up to 1.5 A/cm² at a rate of 1.5 mA/(s·cm²) in fuel cell mode with hydrogen humidified by 4 %MH steam and a total flow rate of 2.08 smL/(s·cm²) (standard milliliter per second and square centimeter). Consecutively, impedance spectroscopy measurements were conducted at 4 %MH and 60 %MH at OCV and 8 A/cm² (electrolysis mode), respectively in order to characterize the initial state of the cells. After this initial characterization the degradation experiment was started as described in the following chapter. Finally, after the ultimate impedance spectroscopic characterization the cells were cooled down in 1.04 smL/(s·cm²) forming gas at a rate of 3 K/min or lower. The oxygen electrode was always supplied with compressed, dehumidified and filtered air, while the flow rate was always set to match that of the hydrogen electrode.

| Target Temperature | Time at Target Temperature | Hydrogen electrode | | | | Air electrode |
|--------------------|----------------------------|--------------------------|--------------------------|--------------------------|--------------|--------------------------|
| | | Hydrogen | Nitrogen | Forming gas | χ_{H_2} | Purified air |
| °C | min | smL/(s·cm ²) | smL/(s·cm ²) | smL/(s·cm ²) | % | smL/(s·cm ²) |
| 900 | 15 | 0 | 0 | 0.522 | 5 | 0.522 |
| 900 | 60 | 0.067 | 1.042 | 0 | 6 | 1.108 |
| 900 | 30 | 0.133 | 1.042 | 0 | 11 | 1.175 |
| 900 | 30 | 0.267 | 1.042 | 0 | 20 | 1.308 |
| 900 | 30 | 0.533 | 1.042 | 0 | 34 | 1.575 |
| 900 | 30 | 1.067 | 1.017 | 0 | 51 | 2.083 |
| 900 | 60 | 2.083 | 0 | 0 | 100 | 2.083 |

Table 2: Reduction procedure

3.2.6 Procedure of degradation experiment

After heat-up and initial characterization, the degradation experiment was started. The desired temperature and humidification were applied and the cells were strained with the desired current. Flow rates were kept constant after the final reduction step, which translates into a minimum steam utilization of approximately 3.5 % at 0.5 A/cm² and 80 %MH and a maximum of approximately 20 % at 1.5 A/cm² and 40 %MH. The

high flow rates were chosen to reduce gradients across the length of the cell and thus minimizing the emergence of local degradation effects.

The current was interrupted approximately every 168 h (weekly) for intermediate cell characterizations. In order to gain comparable data humidification and temperature were adjusted to 60 %RH and 800 °C, respectively for all impedance spectroscopy measurements. These were conducted at OCV as well as 8 A/cm² in order to investigate the effect of degradation in electrolysis operation while keeping the current density low enough to exclude additional degradation due to the EIS measurement. After characterization current was reapplied and the degradation measurement was continued. At the end of the degradation experiment after approximately 1000 h a final characterization was conducted, again at the previously mentioned conditions, before the cells were cooled down.

3.2.7 Solid oxide electrolysis cells

The investigated cells are commercial fuel cells produced by CeramTec, Plochingen, Germany. They are supported by a 290 µm hydrogen electrode layer, which is a composite of Ni and 8YSZ produced by warm pressing using a so-called Coat-Mix material and pre-sintered at 1230 °C. The active electrode of the cells is a porous composite consisting of 8-10 µm Ni/8YSZ active layer. The electrolyte consists of a tape-casted 8YSZ layer with a thickness of 10 µm sintered at 1230 °C. In addition a 3-4 µm screen-printed GCO diffusion barrier layer was employed to reduce reactivity between the 8YSZ electrolyte and the La_{0.6}Sr_{0.4}Co_{0.2}Fe_{0.8}O_{3-δ} (LSCF-6428) oxygen electrode, which has a thickness of approximately 30 µm. A detailed characterization of the cells will be provided in chapter 3.4.

3.3 Post-test measurements

Various diagnostic tools were applied on reference and operated cells in order to gain insight into changes within the cells. These post-test measurements will be described briefly in the following section while special properties and settings will be explained.

3.3.1 Scanning electron microscopy

All layers of the cells were investigated for morphological changes by scanning electron microscopy (SEM), using a Zeiss ULTRA plus. As common for SOFC materials high acceleration voltages (10–20 kV) were being used, while a carbon layer was sputtered onto the investigated surface to prevent charge build-up. Angle selective backscatter (AsB) detector was applied.

Additionally, to these “conventional” measurements, images were taken under special conditions. The charge up of the investigated surface can intentionally be exploited by omitting the carbon layer while using low acceleration voltages of 0.8–1 kV in combination with an In-Lens Detector (ILD). This results in a contrast between an electronically conducting percolated phase (white) and isolated particles (dark). Images taken with the Secondary Electron Detector (SED) at the same low acceleration voltages can provide good material separation. The combination of these two measurements is especially helpful to highlight the Ni percolation network and distinguish percolated from isolated Ni particles.

Furthermore, the build in energy-dispersive X-ray spectroscopy (EDS) was implemented to identify target compositions as well as detect local compositional changes such as demixing. While at typical setting a lateral resolution of $1\ \mu\text{m}^2$ and below can be realized, it is limited due to a depth excitation and resonance of several μm .

3.3.2 Raman spectroscopy

Raman spectroscopy was applied to investigate YSZ modifications using a Horiba Jobin Yvon HR ramanspectrometer. For analyses a laser beam with a wavelength of 532 nm was applied. In order to achieve sufficient lateral resolution an optical microscope was employed leading to a focus of approximately $4\ \mu\text{m}^2$. This also leads to a local increase in sample temperature. While this can be problematic for organic materials like PEM-polymers, the investigated YSZ is designed for high temperature application and therefore the measurement should have no significant influence.[64] Data was generated with a spectral resolution of approximately $2\ \text{cm}^{-1}$ and an accumulation of 50 repetitions.

3.3.3 X-ray diffraction

X-ray diffraction (XRD) was conducted on a STOE-STADI-diffractometer in a BRAGG-BRENTANO test assembly. The acceleration voltage was set to 45 kV, the X-ray current intensity was 30 mA, cobalt as tube cathode material. The X-ray path was influenced by slits and single-crystal monochromators to Co $K_{\alpha 1}$ with $\lambda = 0.178899$ nm; step time/data point = 3 s; step size = 0.04° ; $2\theta = 15-90^\circ$. Data analysis was conducted using the program “Spectragryph v1.0.6”.

3.3.4 X-ray photoelectron spectroscopy

Surface sensitive analyses of the LSCF layer were conducted by X-ray photoelectron spectroscopy (XPS) at room temperature using an Al K_{α} X-ray source (Thermo XR4). Combined with a lens setup a resolution of 0.8 mm^2 was achieved. Measurements were conducted in vacuum (10^{-9} mbar base pressure) generated by a Thermo Scientific ESCALAB 250. Quantification of analyzed elements is based on peak integrals and sensitivity factors provided from Thermo Scientific. In order to gain information on sub-surface layers Ar^+ sputtering was conducted using a Thermo EX05 ion gun. More detailed information on experimental settings can be found elsewhere.[65]

3.3.5 Image analysis

Image analysis was conducted using the public domain software “ImageJ 1.50i”. If necessary images were processed using the built-in processing functions prior to adjusting gray level thresholds according to desired phase separation. In order to limit noise effects an area threshold of 10 and 20 square pixel⁵ was introduced for Ni and pore phase, respectively.

⁵ The images used for analysis were $144 \cdot 1024$ pixels, leading to a total area of approximately $147 \cdot 10^3$ square pixel. The area discrepancy due to the introduction of an area threshold is below 1 % relative to total area of the respective phase. However, the threshold is of important as perimeter / area ratio would be falsified significantly by a large number of wrongly detected small particles.

3.4 Model simulation

Simulation was conducted using a 2D modeling framework for planar SOC, originally presented in [66] and described therein in more detail. Based on physical conservation laws it encompasses transport and conversion in the gas channels and porous layers as well as coupled electrochemistry and transport in electrodes and electrolyte. It implements an elementary-kinetic description of electrochemical and heterogeneous reactions, where multi-step chemical mechanisms account for coupled charge-transfer and surface chemistry. Mass transport is considered on different levels applying continuum mechanics. Convection and diffusion within the channel is described using Navier-Stokes conservation equations whereas Stefan-Maxwell diffusion and Darcy viscous flow are used to describe mass transport in the porous layers. The model furthermore considers electric potential steps due to interfacial double layers and allows for the prediction of electrochemical impedance spectra. The original model framework has since been refined and widely applied for various SOC related topics like Ni re-oxidation [67, 68], CO conversion [69, 70], carbon deposition [71, 72], sulfur poisoning [73, 74], pressurized operation [75–78], reformat conversion [71] and composite LSCF/CGO oxygen electrodes [79].

The simulation approach was implemented to characterize cells used in this investigation, in order to better understand experimental findings, while model reduction studies are conducted to elucidate the nature of rate limiting processes. The model parameters used and their respective values are listed in Table 3.

| Parameter | Value | Reference |
|--|---|------------|
| <u>Ni/YSZ Hydrogen electrode</u> | | |
| Thickness of active layer | 10 μm | Experiment |
| Thickness of support layer | 290 μm | Experiment |
| Hydrogen electrode porosity | 0.37 | Experiment |
| Hydrogen electrode/gas surface specific area | $3.0 \cdot 10^6 \text{ m}^2 \cdot \text{m}^{-3}$ | Estimate |
| Hydrogen electrode pore tortuosity | 1.7 | Estimate |
| Ni particle radius | 0.5 μm | Assumed |
| Anode pore size | 1 μm | Assumed |
| Surface site density | $6.1 \cdot 10^{-5} \text{ mol} \cdot \text{m}^{-2}$ | [71, 80] |
| Interfacial DL capacitance | $1.2 \text{ F} \cdot \text{m}^{-2}$ | Fit |
| <u>YSZ Electrolyte</u> | | |
| Thickness, d_{YSZ} | 10 μm | Experiment |

3 - Scientific Approach and Methodology

| | | |
|---|--|------------|
| Ionic conductivity of bulk YSZ | $T/(1.4 \cdot 10^7 \text{K}) \cdot e^{(90000/k_B T)}$ S/m | [71, 80] |
| Surface site density | $1.3 \cdot 10^{-5} \text{ mol} \cdot \text{m}^{-2}$ | [71, 80] |
| Bulk density | $6800 \text{ kg} \cdot \text{m}^{-3}$ | [71, 80] |
| Bulk vacancy/oxygen fraction | 0.0401/0.9599 | [71, 80] |
| LSCF/YSZ cathode | | |
| Thickness | 30 μm | Experiment |
| LSCF/gas surface specific area | $9.1 \cdot 10^4 \text{ m}^2 \cdot \text{m}^{-3}$ | [79] |
| Oxygen electrode porosity | 0.37 | Experiment |
| Oxygen electrode pore tortuosity | 2 | Assumed |
| Oxygen electrode pore size | 0.167 μm | [79] |
| LSCF particle radius | 1 μm | Assumed |
| Pore size | 1 μm | Assumed |
| LSCF/gas phase DL capacitance | $100 \text{ F} \cdot \text{m}^{-2}$ | [79] |
| LSCF/CGO Interfacial DL capacitance | $(0.245 \cdot T / \text{K} - 185) \text{ F} \cdot \text{m}^{-2}$ | [79] |
| Surface site density | $1.0 \cdot 10^{-5} \text{ mol} \cdot \text{m}^{-2}$ | [79] |
| Bulk density | $6890 \text{ kg} \cdot \text{m}^{-3}$ | [79] |
| Bulk vacancy/oxygen fraction | 0.01/0.99 | [79] |
| Current collector mesh | | |
| Hydrogen electrode side Ni net | $1024 \text{ mesh} \cdot \text{cm}^{-2}$ $6.4 \cdot 10^{-4} \text{ m}$ | Experiment |
| Hydrogen electrode mesh porosity, ε_M | 0.78 | Experiment |
| Hydrogen electrode mesh tortuosity | 3.5 | Experiment |
| Hydrogen electrode mesh pore size, ρ_W | 80 μm | Experiment |
| Oxygen electrode side Pt net | $3600 \text{ mesh} \cdot \text{cm}^{-2}$ $8.64 \cdot 10^{-4} \text{ m}$ | Experiment |
| Oxygen electrode mesh porosity, ε_M | 0.83 | Experiment |
| Oxygen electrode mesh tortuosity | 3.0 | Experiment |
| Oxygen electrode mesh pore size, ρ_W | 128 μm | Experiment |
| Gas channel | | |
| Length | 0.065 m | Experiment |
| Thickness | $3.0 \cdot 10^{-3} \text{ m}$ | Experiment |
| Inflow velocity | 0.125 sL/(cm ² ·min) | Experiment |
| Experimental conditions | | |
| Temperature, T | 973 K – 1123 K | Experiment |
| Pressure | 1 atm | Experiment |
| Hydrogen electrode gas Composition | H ₂ / H ₂ O (variety) | Experiment |
| Oxygen electrode gas Composition | 21 % O ₂ , 79 % N ₂ | Experiment |

Table 3: List of parameters used for electrochemical modeling in this study

4 Cell Characterization

In order to investigate SOEC it is of crucial importance to understand the investigated cells as thoroughly as possible. Obviously, knowledge of the initial state of the cells is of great importance, while a detailed understanding of the individual rate limiting processes is necessary to reliably separate, quantify and interpret degradation processes.

This chapter will provide detailed information about the cells investigated using different approaches. Microstructural properties will be presented by SEM imaging while image analysis is used for microstructural quantification. The electrochemical performance will be investigated based on polarization curves as well as impedance spectroscopic data using equivalent circuit approach, which is furthermore substantiated by DRT analysis. Finally, a physico-chemical model is implemented in a wide range of operating parameters including model reduction studies in order to elucidate the fundamental elementary processes involved and ensure a better understanding of experimental results.

4.1 Microstructural characterization

The cross-section of a reference cell is presented in Fig. 9. The reference cell was previously only heated up, reduced and cooled down according to the procedure described in chapter 3.2.5. Fig. 9 displays the individual layers and reveals their homogeneity in thicknesses. The difference in porosity and particle size between substrate and active electrode is clearly visible. The YSZ electrolyte shows a number of manufacturing related small holes. The crack along the CGO | YSZ interface as well as signs of spalling are in all likelihood caused during sample preparation as a result of epoxy resin shrinkage. The LSCF layer shows a rough topography reaching half way through the thickness of the layer. This was observed for all cells and is probably caused by the removal of contacting mesh or alternatively production related.

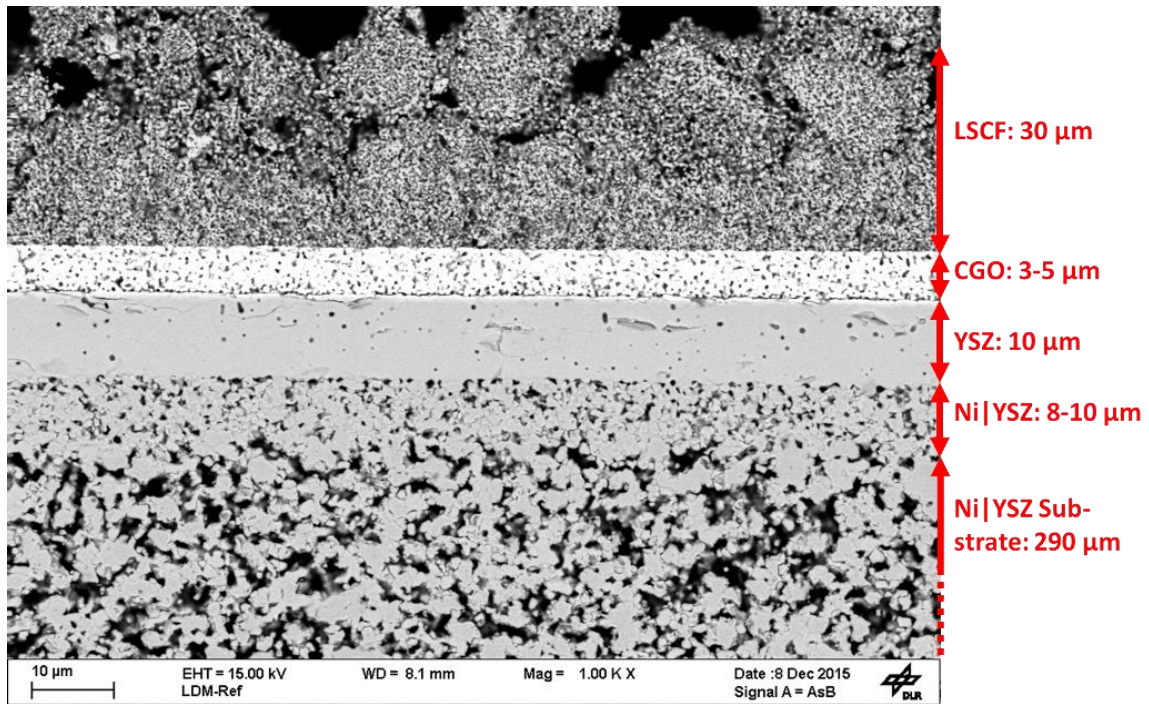


Fig. 9: Cross-section of a reference cell displaying the respective cell layers

A section of the oxygen electrode close to the electrolyte of a reference cell is presented in Fig. 10. It shows a fine microstructure with sub-micrometer particles and high porosity. Furthermore, irregularities within the LSCF can be observed concerning signal intensities. These are caused by differences in molar weight resulting in varying intensities of back scattered electrons (BSE). This phenomenon will be further discussed in section 5.2.

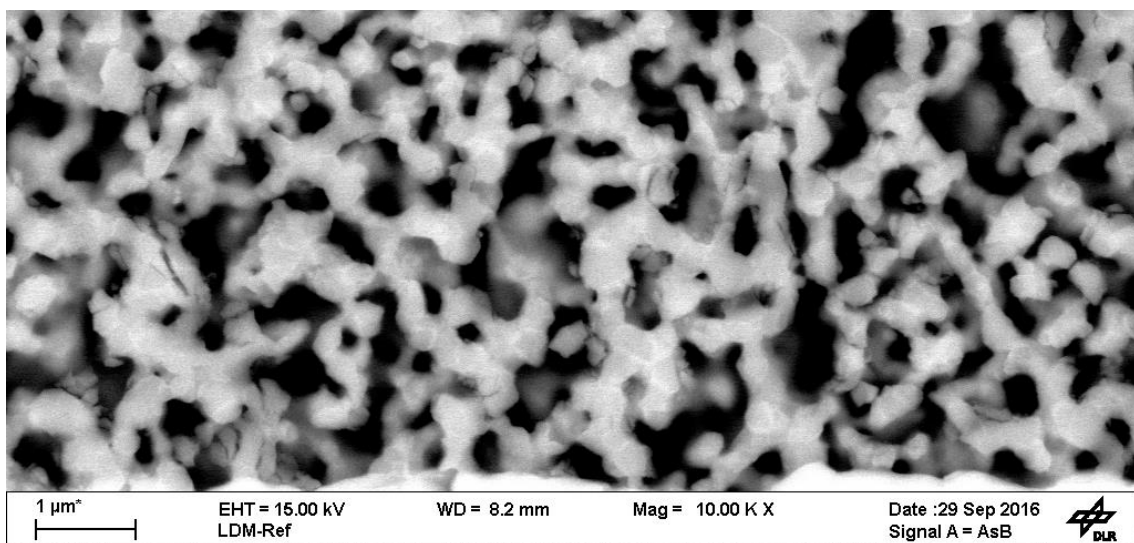


Fig. 10: Image of the porous LSCF structure of the oxygen electrode close to the electrolyte of a reference cell

Quantification of microstructural properties is important to assess changes objectively. Fig. 11A displays a low acceleration voltage SE-SEM image of a reference cell's active electrode with electrolyte (top) and support layer (bottom). The framed section was used for quantification and presents an area of 8 μm by 56 μm . This was chosen to ensure that the results are not influenced by the support. The identical section of the cell was also investigated using an IL detector as presented in Fig. 11B. Combining the information of these two images results in the possibility to separate the three phases – pores, YSZ skeleton and Ni percolation network⁶ – using an image analysis tool. The result is shown in Fig. 11C where the areas used for quantification are displayed in red and yellow for pores and percolated Ni, respectively. The remaining area is allocated to the YSZ phase.

⁶ Additionally, there is a fourth phase, the non-percolated Ni particles. These could not be separated using image analysis software and are allocated to the YSZ phase (compare Fig. 11C). However, from a quantitative aspect they are of little significance.

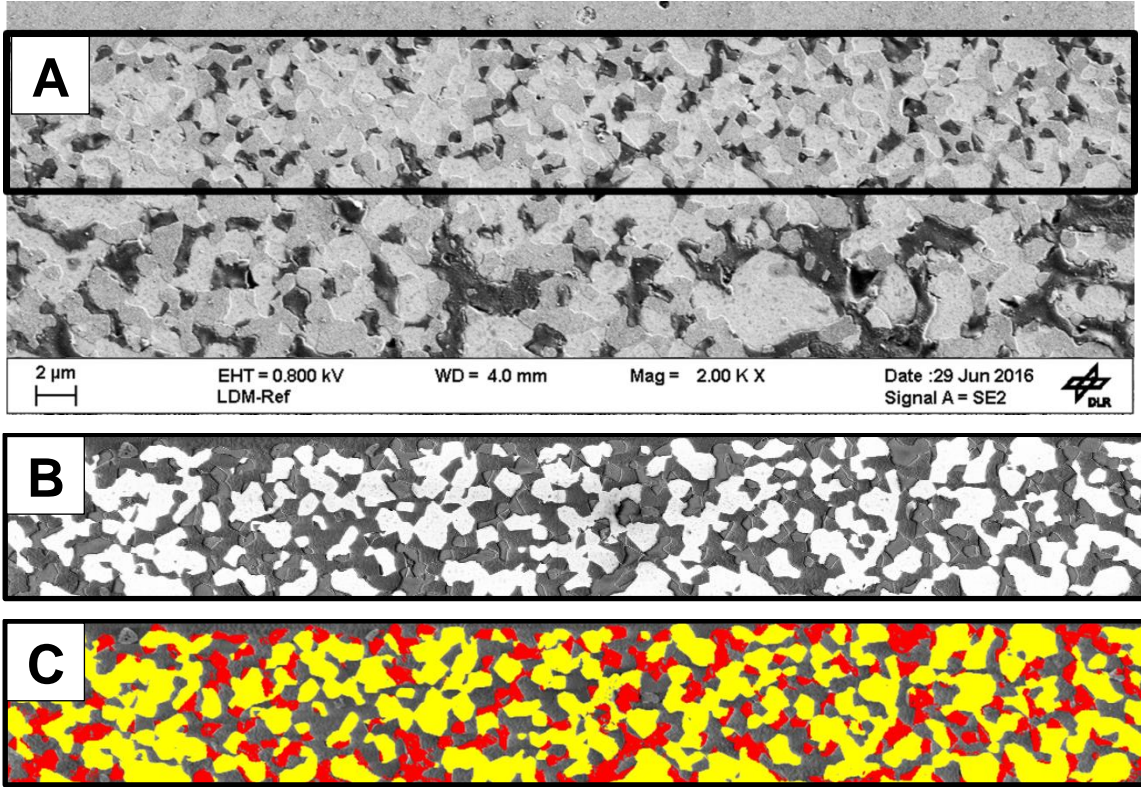


Fig. 11: Exemplary section of the hydrogen electrode of a reference cell which is used for quantitative analysis. Images of this section were recorded using SE detector (A) and IL detector (B). Combining this information (C) leads to a separation of the three phases pores (red), percolated Ni (yellow) and YSZ (rest) which can then be used for quantification.

The respective area corresponds to the volume fraction of each phase. While it would be desirable to extract information about the average particle size and number of particles per area, this information is dubious since the Ni particles are connected in an irregularly shaped network and therefore not separable unambiguously. Unfortunately, it is also impossible to extract the length of the triple phase boundary from this 2D image while 3D reconstruction is required for this type of information. However, the ratio of perimeter to area of the percolated Ni phase in the cross-section is a good parameter to describe size and shape of the Ni particles, as it reflects the surface area potentially available per Ni volume. This will be given as an equivalent radius r_{equ} of a theoretical sphere with the same perimeter P to surface A ratio according to:

$$r_{equ} = \frac{2A}{P} \quad (4-1)$$

The respective parameters are presented in Table 4.

| | $A_{YSZ} / \%$ | $A_{Ni_perc} / \%$ | $A_{Pores} / \%$ | $r_{equ} / \mu m$ |
|----------------------------|-----------------------------------|-----------------------------------|-----------------------------------|-------------------------------------|
| Position 1 | 37.3 | 44.4 | 18.4 | 0.596 |
| Position 2 | 37.0 | 43.7 | 19.3 | 0.552 |
| Position 3 | 35.9 | 46.0 | 18.1 | 0.601 |
| Position 4 | 37.7 | 47.0 | 15.3 | 0.624 |
| Average⁷ | 37.0 ± 0.67 | 45.2 ± 1.29 | 17.8 ± 1.50 | 0.591 ± 0.026 |

Table 4: Quantification of microstructural properties of the hydrogen electrode in its initial state.

4.2 Characterization of electrochemical performance

The initial polarization curve of each cell was conducted in fuel cell mode (negative current⁸) at low humidities for better performance comparison to SOCs reported in literature. A representative polarization curve is depicted in Fig. 12. The final current density of -1.5 A/cm^2 was reached at a voltage of approximately 725 mV which corresponds to a power density of 1.1 W/cm^2 . It should be noted that this is not the maximum power density for these cells. However, the cells were not strained past -1.5 A/cm^2 during initial characterization in order to minimize its impact.

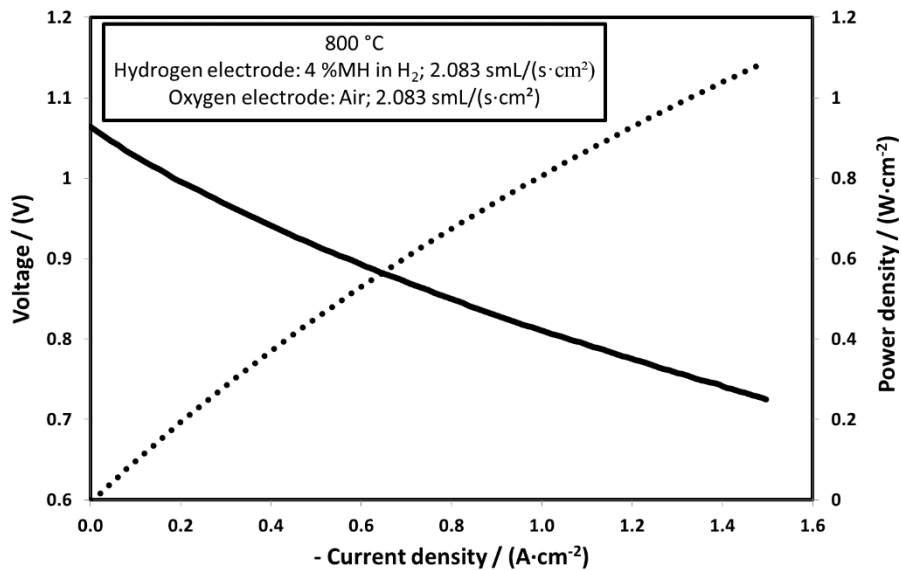


Fig. 12: Polarization curve of a representative reference cell in fuel cell mode at 4 %MH after reduction.

⁷ Mean value with standard deviation

⁸ Positive current densities are used to describe electrolysis mode since this work focusses on electrolysis while negative currents represent fuel cell mode.

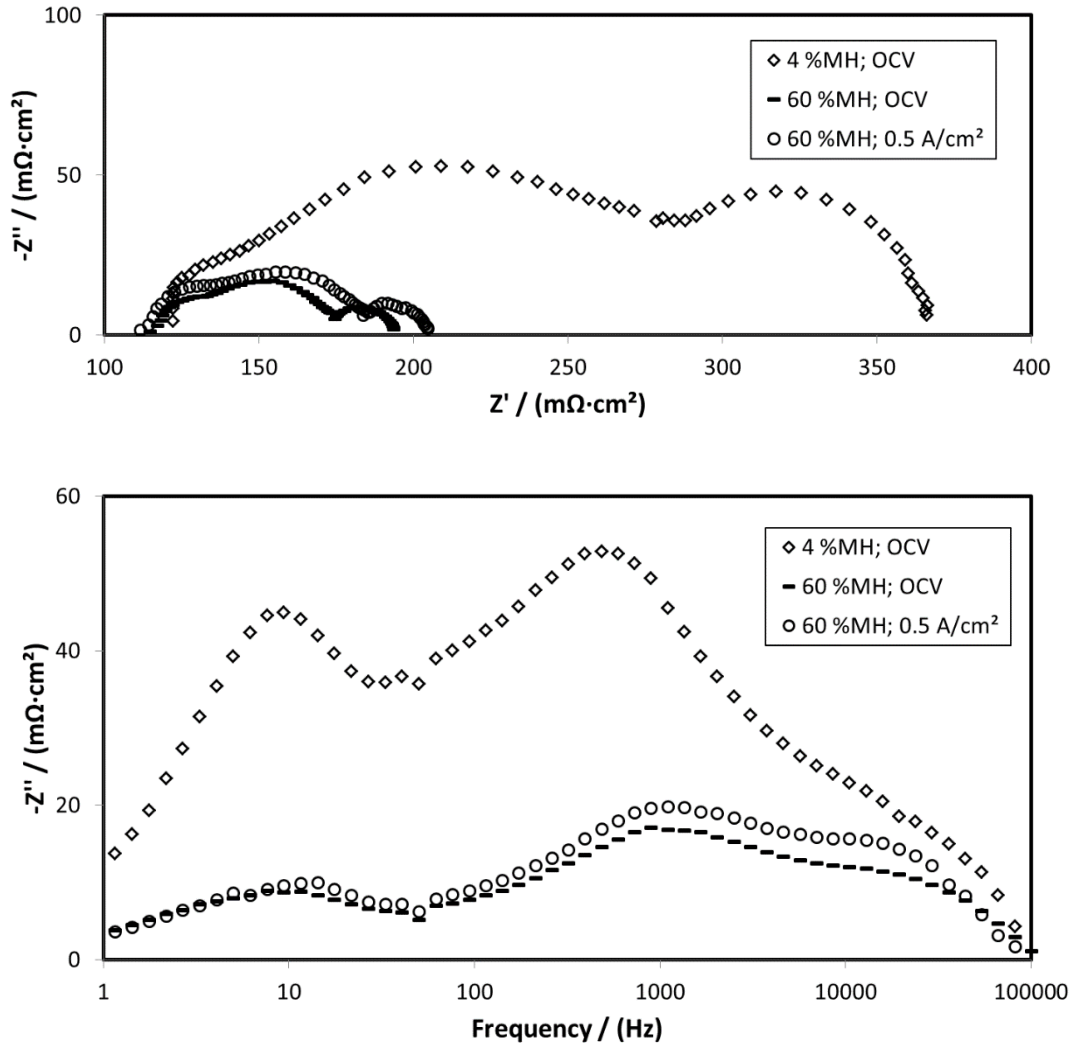


Fig. 13: Representative induction-corrected impedance spectra of cells in their initial state measured at 4 %MH and OCV, 60 %MH and OCV as well as 60 %MH and -0.5 A/cm^2 . Image at the top shows the Nyquist plot of the spectra while the bottom graph shows the imaginary Bode plot.

Initial characterization also included impedance spectra under different conditions as presented in Fig. 13. The ohmic resistance is virtually identical for all investigated operating conditions confirming that the furnace temperature was adopted properly to compensate for the DC-bias related temperature change. The increase of humidity from 4 %MH to 60 %MH leads to a drastic decrease of the polarization resistance as expected. When comparing both spectra recorded at 60 %MH but different current densities, deviations can be found almost exclusively at the high frequency hydrogen elec-

trode processes (10^3 Hz to 10^4 Hz). The process at approximately 10 Hz which corresponds to the gas concentration polarization increases only marginally.

Quantification of recorded impedance spectra was realized by fitting spectra to a previously determined equivalent circuit according to the complex nonlinear least squares (CNLS). Obviously, the validity of the quantitative results strongly depends on the quality of the equivalent circuit. To ensure a physically meaningful equivalent circuit interpretation DRT analysis was applied. This technique improves the separation of overlapping processes and provides information on their characteristic frequencies. A typical DRT plot of a cell in its initial state measured at 800 °C and 60 %MH is presented in Fig. 14. Including the ohmic resistance, it shows the existence of five rate limiting processes separable by impedance spectroscopy. Their characteristic frequencies are approximately one order of magnitude apart and roughly occur at 10^4 , 10^3 , 10^2 and 10 Hz, respectively.

By varying operating parameters and monitoring their influence on the individual processes, dependencies can be determined allowing for a physical interpretation of the respective processes.[81–84] The results suggest that the two high frequency peaks ($\sim 10^3$ and 10^4 Hz) can be assigned to the hydrogen electrode limitation, the medium frequency peak ($\sim 10^2$ Hz) represents the oxygen electrode charge transfer combined with its ionic resistance and the low frequency peak (~ 10 Hz) corresponds to the gas transport limitation at the hydrogen electrode. These findings are in accordance with the simulative study presented in chapter 4.3, where also a more detailed explanation of the physical processes will be given.

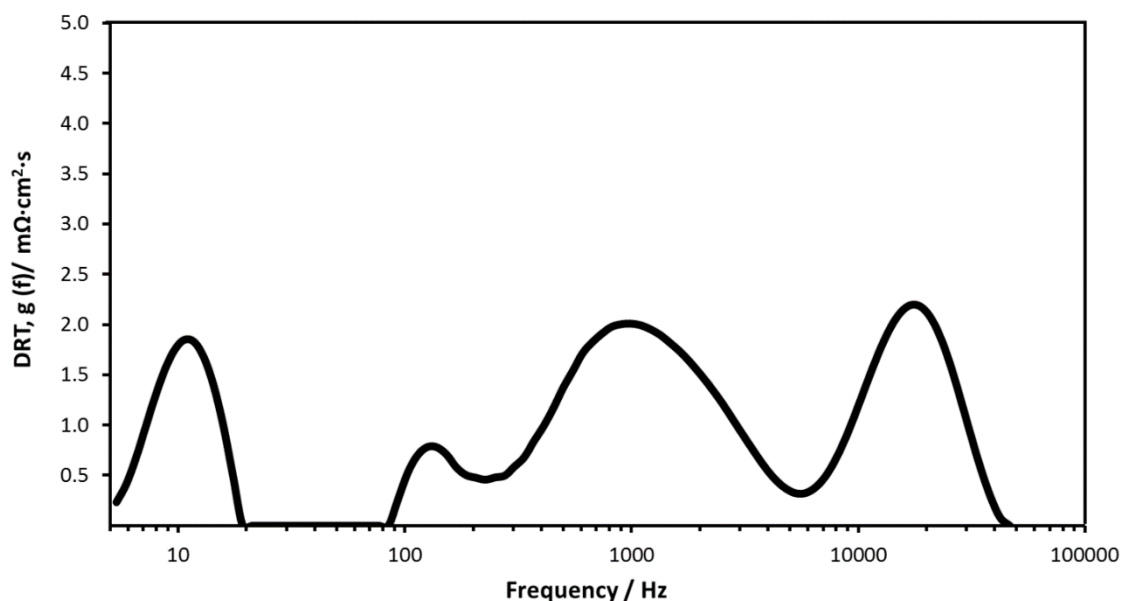


Fig. 14: DRT analysis of an impedance spectrum of a cell in its initial state.

This insight leads to the equivalent circuit model presented in Fig. 15A which was used for CNLS quantification. Both hydrogen electrode processes are represented by R-CPE-elements (resistor in parallel with a constant phase element with exponent of 0.9). The oxygen electrode process is characterized by a closed Gerischer Element, accounting for the charge transfer coupled with the ionic transport within the electrode.[81–87] The gas transport limitation is portrayed by a RC-element⁹. Additionally, a serial resistance represents the ohmic resistance which is dominated by the ionic resistance of the electrolyte but also encompasses contact resistances while an inductive element compensates for inductive interference.

⁹ The gas transport limitation is dominated by gas conversion in contrast to diffusion, as will be explained in the following chapter. Therefore, this process is not characterized by a Warburg Element as commonly seen in literature.[81, 83–85]

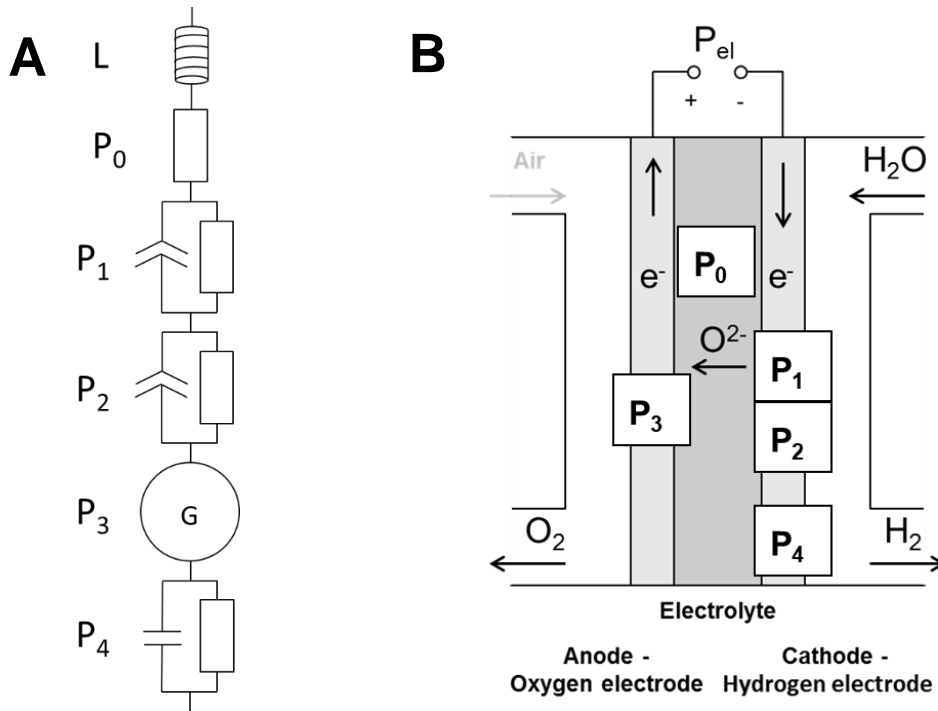


Fig. 15: (A) Equivalent circuit model used for quantification of recorded impedance spectra and (B) location of individual rate limiting steps

A list of these processes can be found in Table 5 summarizing their physical interpretation while also specifying the respective average initial resistance. Fig. 16 visualizes the contribution of the separable rate limiting processes. It also reveals high reproducibility for the cells used in this study as illustrated by the good alignment of exemplary impedance spectra of four cells in their initial state.

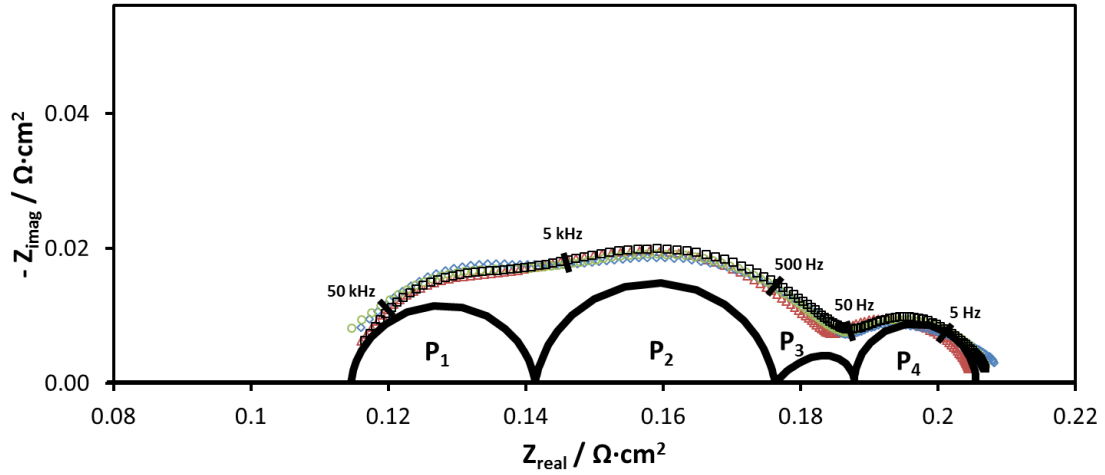


Fig. 16: Four representative impedance spectra of cells in their initial state recorded at 800 °C, 60 %MH and 0.5 A/cm². Contributions of individual rate limiting processes are visualized.

| Process notation | Physical interpretation | Characteristic frequency / Hz | Average initial value | Standard deviation / mΩ·cm ² |
|------------------|---|-------------------------------|-------------------------|---|
| L | Compensation for inductive interference | - | 1-10 nH | |
| P ₀ | Ohmic resistance (ionic transport resistance through electrolyte & contact resistances) | - | 114 mΩ·cm ² | 2.1 |
| P ₁ | Hydrogen electrode ionic transport coupled with charge transfer reaction | 2·10 ⁴ | 29 mΩ·cm ² | 2.9 |
| P ₂ | Hydrogen electrode charge transfer reaction | 10 ³ | 34 mΩ·cm ² | 2.6 |
| P ₃ | Oxygen electrode charge transfer and ionic transport | 10 ² | 11 mΩ·cm ² | 0.5 |
| P ₄ | Hydrogen electrode gas transport | 10 | 17.5 mΩ·cm ² | 0.7 |

Table 5: Processes considered for quantification, their respective physical interpretation, initial characteristic frequency and typical initial resistance at 800 °C, 60 %MH and 0.5 A·cm⁻².

The ohmic resistance represents a series of different contributions. While the ionic resistance of the YSZ electrolyte is its largest share, it is unfortunately not possible to separate it from the ionic resistance of the GDC-layer, contact resistances and others. Furthermore, the resistivity of YSZ produced by tape casting varies depending on the production procedure. A typical value of 50 Ω·cm to 60 Ω·cm at 800 °C [88, 89] suggests that the YSZ electrolyte accounts for approximately 50 % of total ohmic resistance of the cells tested.

4.3 Simulative characterization

4.3.1 Model validation

One target of the simulative approach in this dissertation is to provide detailed knowledge of the investigated cells. While there are many cell parameters which can be determined directly by electrochemical or post-test investigations, there are intrinsic cell parameters which cannot be measured directly or only investing significant effort. An accurate and sufficiently detailed model however can provide in-depth knowledge of the investigated system.

For this the model was parameterized in accordance with a series of polarization curves and impedance spectroscopic measurements in a broad range of operating conditions. The cells used for model parameterization were previously operated at 800 °C, 60 %MH and 0.5 A/cm² for 500 h. This was mainly done for two reasons:

- 1) The time necessary to conduct the experiments required to parameterize the model framework is approximately three days. It is crucial that all cell parameters remain as close to constant as possible during this period. In light of this demand, the cells' initial operating period where significant changes occur in short amount of time is unfit to provide sufficiently stable conditions. (Compare Fig. 5)
- 2) Conditions were chosen to represent all cells and their states as well as possible. Therefore cells were aged for half the usual operating time at average temperature and humidity while the current density was chosen to be slightly below average to exclude possible singular effects occurring only at high current densities.

A comparison between induction-corrected experimental and simulated impedance spectra at different temperatures, hydrogen gas humidities and current densities are presented in Fig. 17, Fig. 18 and Fig. 19, respectively in both Nyquist and Bode Plot. There is a good qualitative and quantitative agreement between modeling and experimental results concerning number of impedance features, magnitude of resistances and relaxation frequencies over the complete investigated range of experimental conditions. The only deviation worth mentioning can be observed at polarization of -0.75 A/cm² shown in Fig. 19, where the simulated spectra exhibits slightly lower imaginary impedance

values at 10^3 Hz and above compared to the experimental data. This could possibly be explained by high frequency interferences in the experimental data, as indicated by the drifting of data points towards lower resistances in the very high frequency region of the Nyquist Plot.

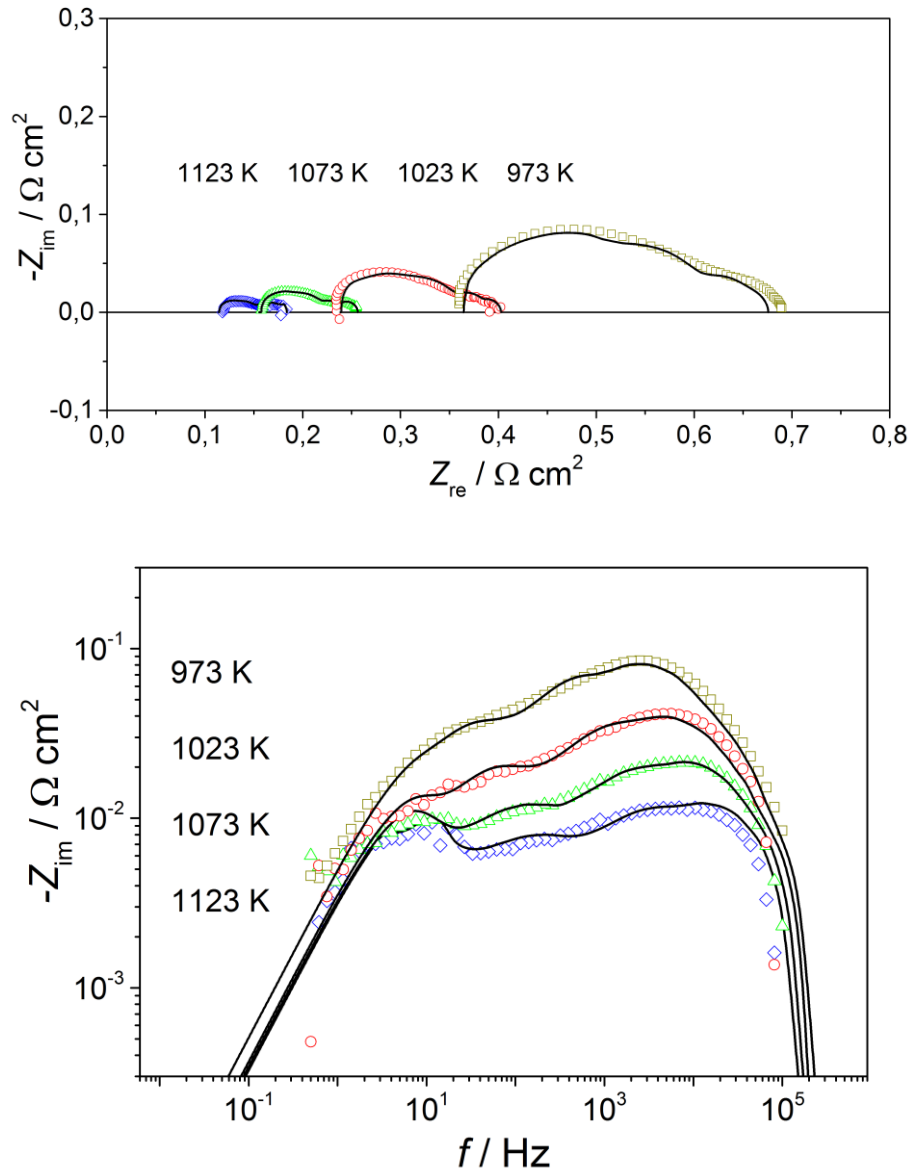


Fig. 17: Comparison of recorded (dots) and simulated (line) impedance spectra at OCV, 60 %MH and various temperatures.

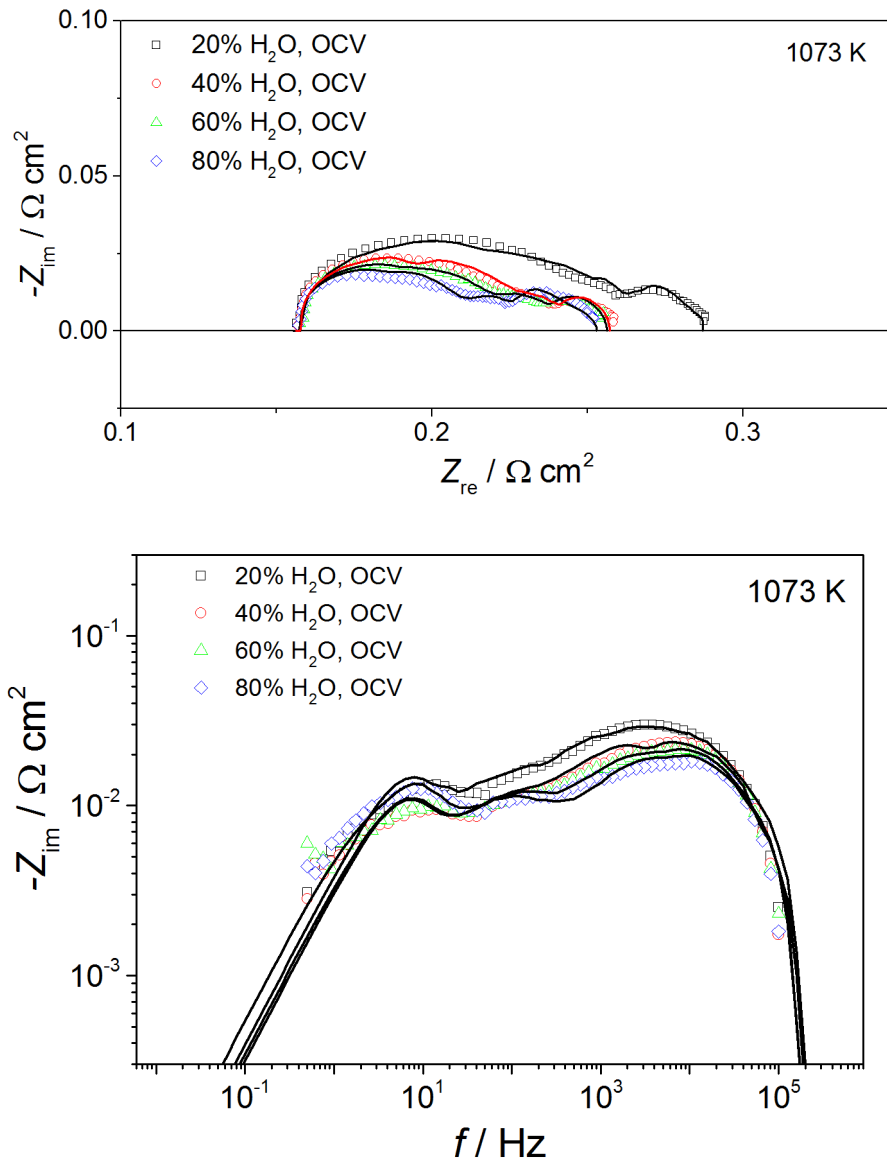


Fig. 18: Comparison of recorded (dots) and simulated (line) impedance spectra at OCV, 800 °C and various humidities.

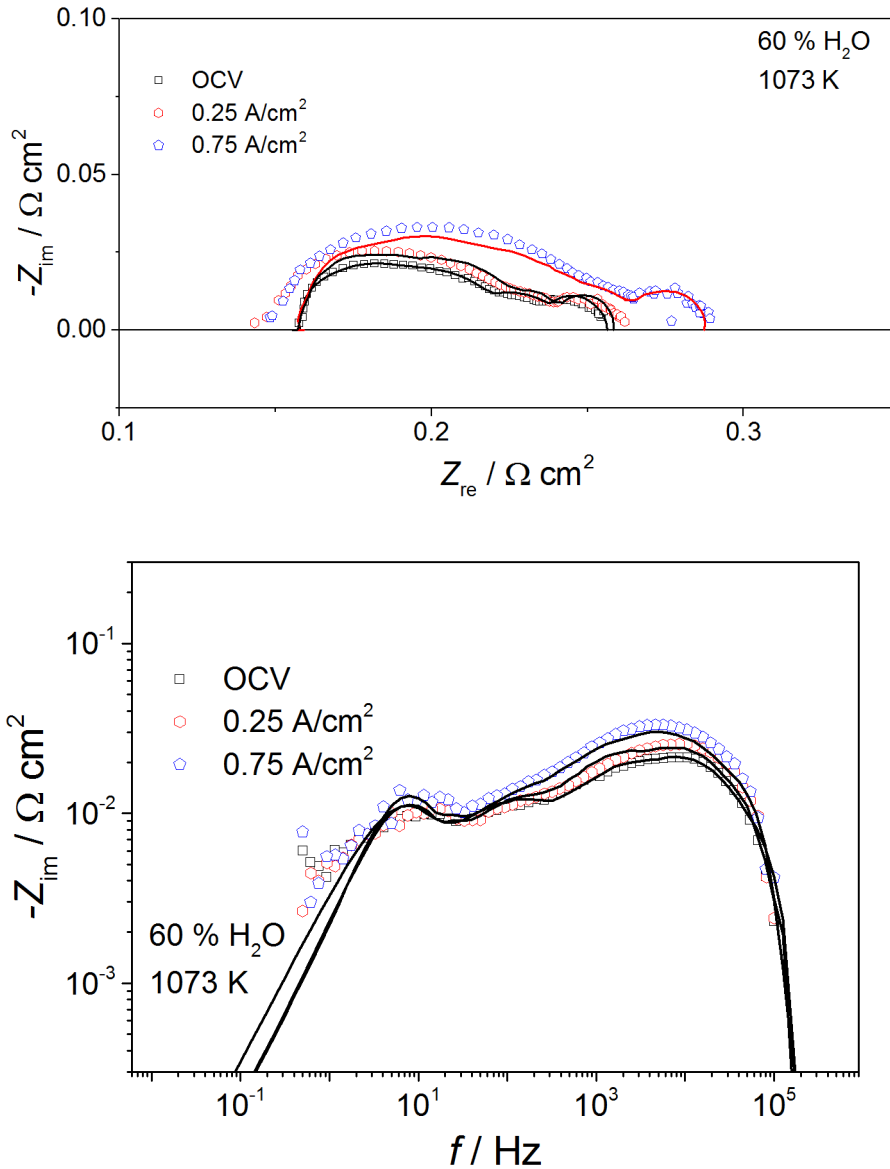


Fig. 19: Comparison of recorded (dots) and simulated (line) impedance spectra at 60 %MH, 800 °C and various current densities.

Additionally to the various impedance spectra also reversible SOC polarization curves were recorded at two temperatures and compared to simulated polarization curves as depicted in Fig. 20. Again there is a good agreement between the two in the simulated range. Only at high current densities in electrolysis mode a slight deviation can be observed where the voltage is higher for the measured data. This can possibly be explained by a suspected partial bypass of hydrogen gas within the new cell holders, which would account for the slightly higher than expected increase in voltage at high current densities.

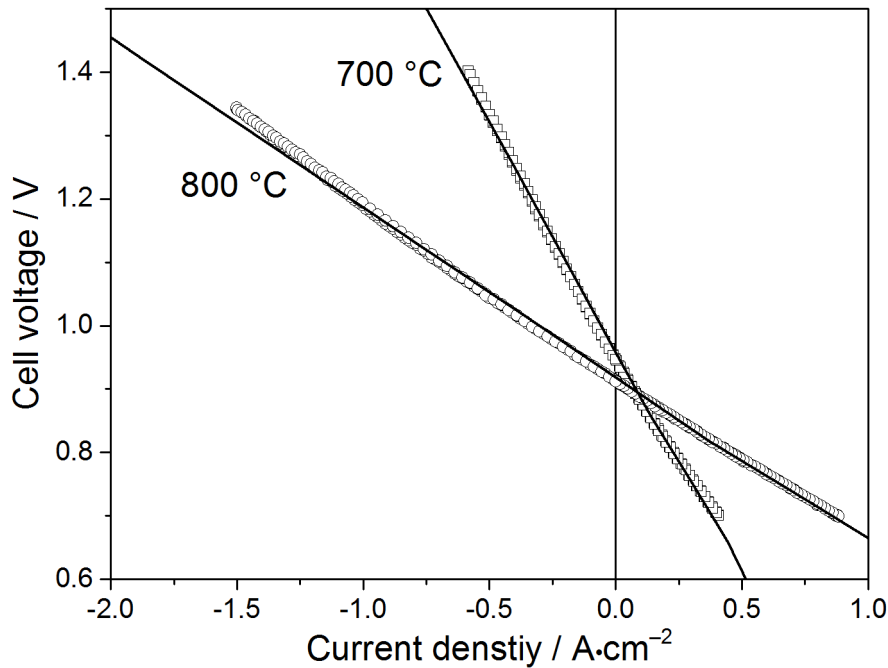


Fig. 20: Measured (dots) and simulated (line) polarization curves at 60 %MH and a temperature of 700 °C and 800 °C.

4.3.2 Reduction studies

The validated model was used to conduct model reduction studies in order to isolate individual processes as shown in Fig. 21. The original “full 2D” model which shows the existence of four processes is reduced in two steps. In the “reduced 1D model” the effect of gas conversion was excluded by holding the gas concentration over the length of the channel equal to the inlet gas composition. This reveals that the low frequency contribution is almost exclusively related to gas conversion. As a consequence it needs to be represented by a RC-element in the equivalent circuit model as described previously in chapter 4.2. When the model is further reduced to “model of oxygen electrode only” the resulting impedance spectrum reveals the effect of the oxygen electrode / electrolyte electrochemistry. It is in good agreement with prior reports of the characteristic frequency of this process in a comparable system [90]. Furthermore, the shape of this process confirms the use of a Gerischer element as representative in the equivalent circuit. The small difference between the “reduced 1D model” and the “model of the oxygen electrode only” in the low frequency region reveals the contribution of gas diffusion through the hydrogen electrode substrate, with its characteristic frequency in its typical range[81]. However, due to its strong overlapping and limited contribution compared to the neighboring processes (oxygen

electrode polarization and gas conversion) it is not possible to reliably quantify this process using equivalent circuit fitting. Consequently, no corresponding equivalent circuit element is introduced. Its contribution is instead compensated for by a slight overestimation of the neighboring processes. This is however acceptable as this study focuses on degradation and the diffusion through the substrate is expected to be largely unaffected by cell deterioration.

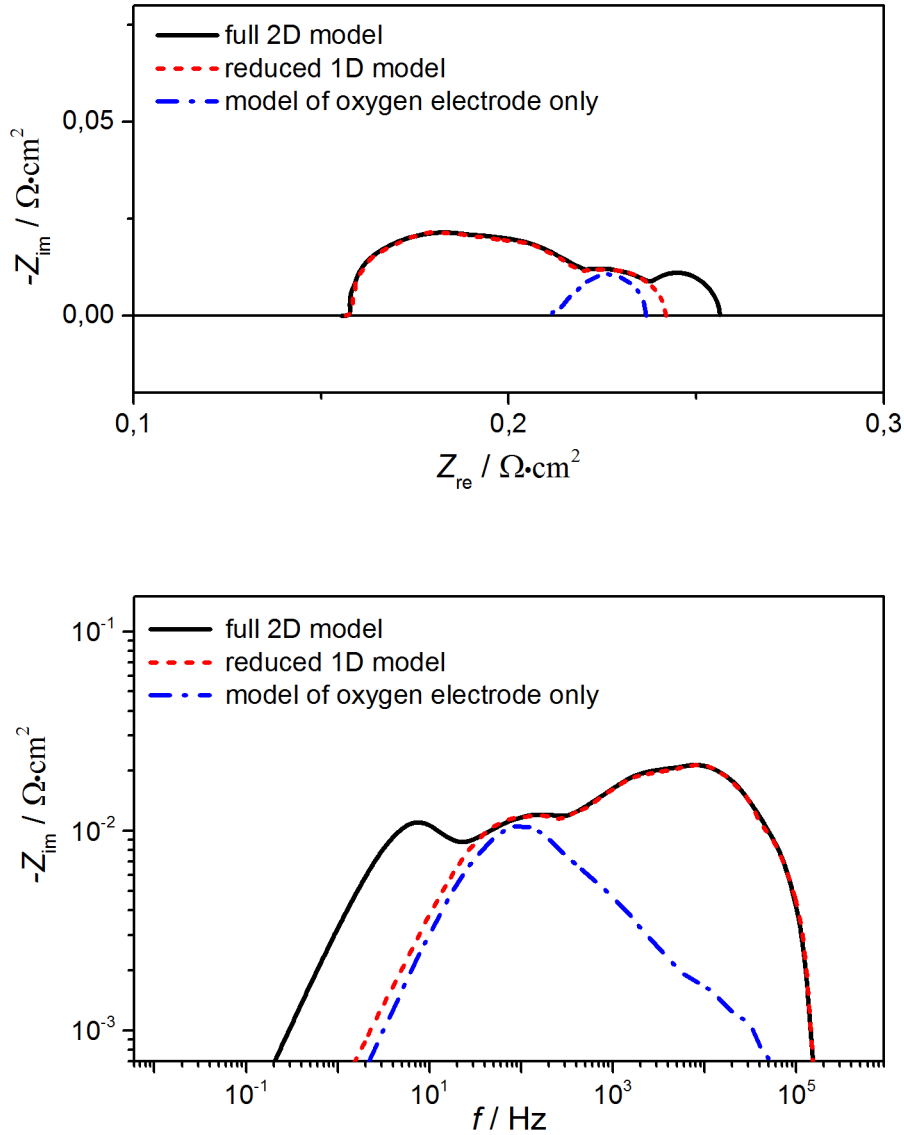


Fig. 21: Model reduction study at OCV, 60 %MH and 800 °C. Comparison between simulated impedance of the “full 2D model” (solid black line) and two reduced models: A “reduced 1D model” (dashed red line) excluding gas conversion and the “model of oxygen electrode only” isolating oxygen electrode and electrolyte electrochemistry (dash-dotted blue line).

The remaining two high frequency processes are both related to the hydrogen electrode. In order to dissolve them the introduced “reduced 1D model” was used as a basis

while specific parameters, namely the rate of the charge transfer reaction (CT rate) and the YSZ content in the active hydrogen electrode, were changed. The effect is displayed in Fig. 22 and Fig. 23, respectively. An increase or decrease of the charge transfer rate by 10 % results in a decrease or increase of the resistance of the process at approximately 10^3 Hz, respectively. All other processes remain virtually identical revealing that this process is in fact related to the actual charge transfer reaction. The nature of the second hydrogen electrode contribution at approximately 10^4 Hz is more complex as shown in Fig. 23. A decrease of the YSZ content in the hydrogen electrode by 10 % results in its increase while there is no influence on any other process. However, an increase of YSZ content of 10 % causes a reduction in resistance of both hydrogen electrode processes. This demonstrates that the higher frequency hydrogen electrode process is directly related to YSZ contribution of the active anode layer and in particular this displays the coupled behavior of ionic transport throughout YSZ within the electrode and charge-transfer process at TPB. Interestingly, the decrease of YSZ content does not have any effect on the charge transfer process, while its increase has a positive impact so that overall resistance is reduced. This suggests that cell performance could be enhanced by increasing the YSZ content of the active hydrogen electrode.

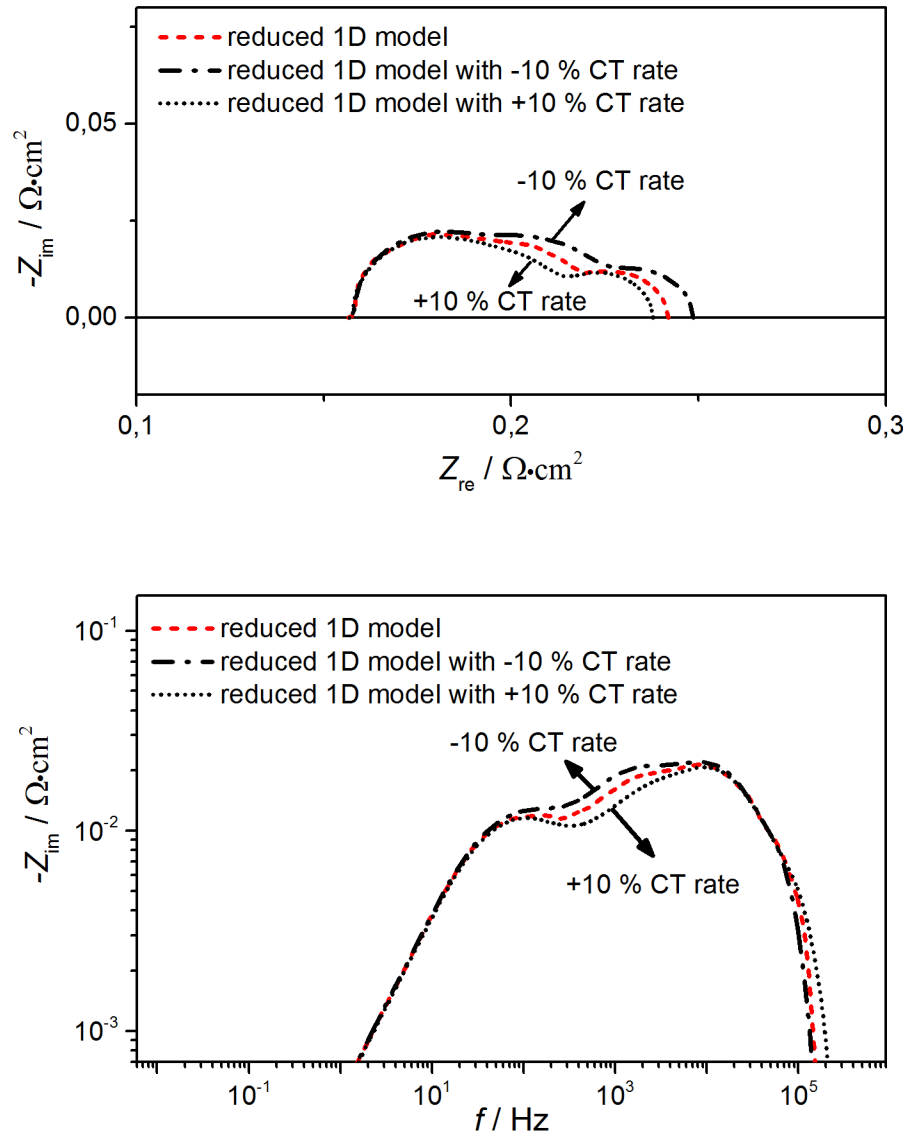


Fig. 22: Change of charge transfer reaction rate (CT rate) in “reduced 1D model” (red line) and its effect on impedance. Minus sign (-) denotes the decrease of the parameter (dash dot line), plus sign (+) denotes the increase of parameter (dotted line). Conditions are 800 °C, OCV and 60 %MH for all spectra.

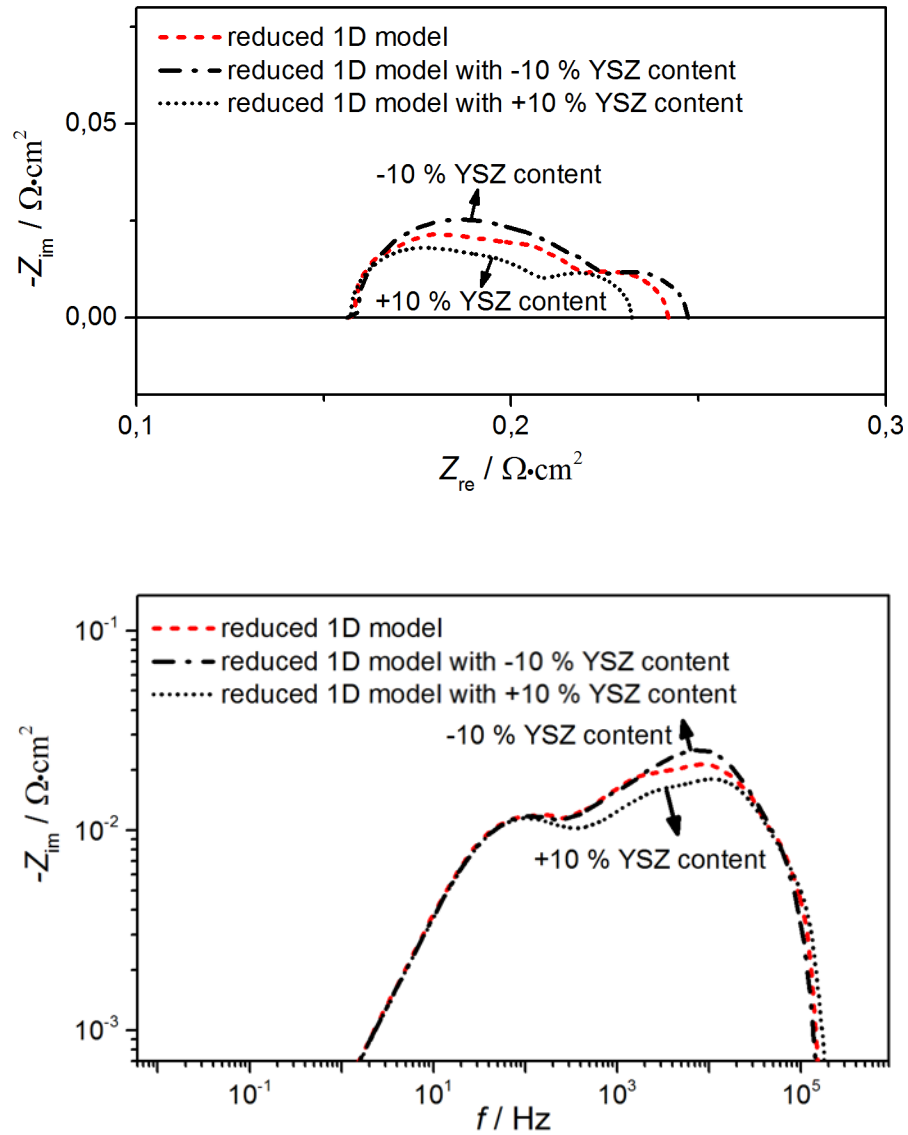


Fig. 23: Change of YSZ content of hydrogen electrode in “reduced 1D model” (red line) and its effect on impedance. Minus sign (-) denotes the decrease of the parameter (dash dot line), plus sign (+) denotes the increase of parameter (dotted line). Conditions are 800 °C, OCV and 60 %MH for all spectra.

5 Degradation Study

The following section will address the degradation processes observed during this study, i.e. the electrochemical degradation monitored in-situ as well as changes to the cells found during post-test analyses. It is structured so that one subchapter is dedicated to each process separable by EIS. Changes in resistance will be described in detail as well as their dependence on operating parameters revealed. Relevant post-test finding will be presented to finally offer explanations for the observed SOEC degradation.

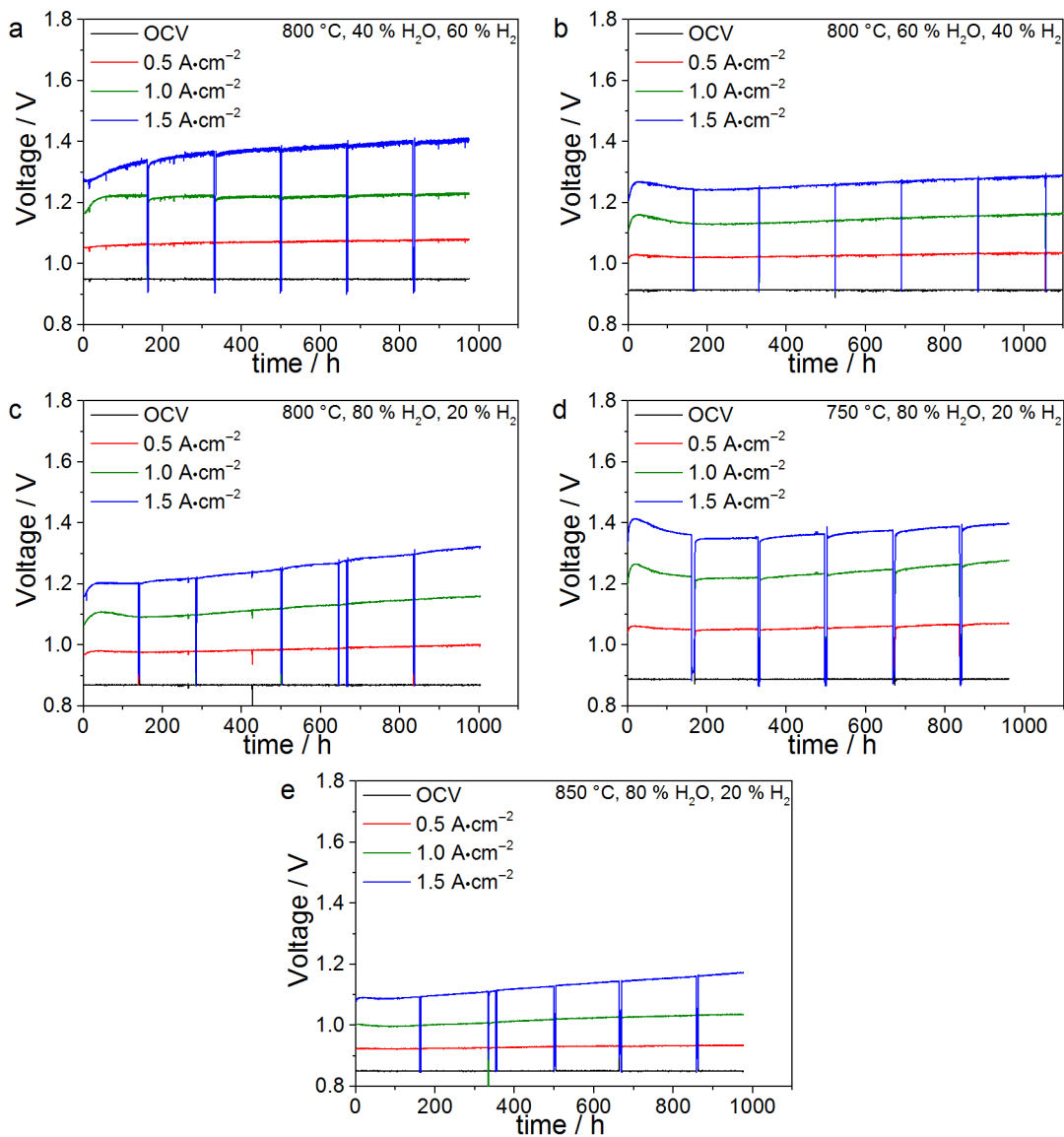


Fig. 24: Voltage evolution with time for cells operated at different current densities and (a) 800 °C and 40 %MH, (b) 800 °C and 60 %MH, (c) 800 °C and 80 %MH, (d) 750 °C and 80 %MH, and (e) 850 °C and 80 %MH.

Fig. 24 presents the evolution of cell voltage with time for all investigated combination of operating parameters. It is difficult to find general trends concerning the degradation behavior of the different rate limiting steps, since this study has shown that most degradation phenomena are influenced by at least two of the three investigated operating parameters. However, a few general observations can be made:

- The ohmic resistance dominates overall degradation in the investigated range of conditions. The parameter dependence study will show that at least two degradation processes contribute.
- While oxygen electrode polarization resistance is initially small, it presents the second largest contribution to overall degradation for most conditions.
- Hydrogen electrode degradation is moderate for most conditions, while even activation (decrease of resistance) was observed. This is to be explained by a significant decrease of the charge transfer reaction resistance coupled with a frequency change observed during the first week (~160 h) for all cells operated at any conditions.
- Resistance of gas conversion and diffusion remain close to constant.

5.1 Ohmic resistance

5.1.1 Ni-depletion

One major change in cell characteristic observed at certain operating conditions is the unidirectional migration of Ni within the active hydrogen electrode away from the electrolyte | electrode interface. This process will henceforth be called Ni-depletion. The resulting shift of the reaction zone of the hydrogen electrode away from the electrolyte effectively translates into an increase of electrolyte thickness and contributes therefore to the increase of the ohmic resistance. The findings of this section have also been published elsewhere.[91]

5.1.1.1 In-situ results

Fig. 25 presents an overview of the evolution of the ohmic resistance for all 20 cells investigated in the five long-term experiments. In Table 6, the increase of ohmic re-

sistance after 1000 h is summarized for all cells, based on the individual initial resistance of each cell.

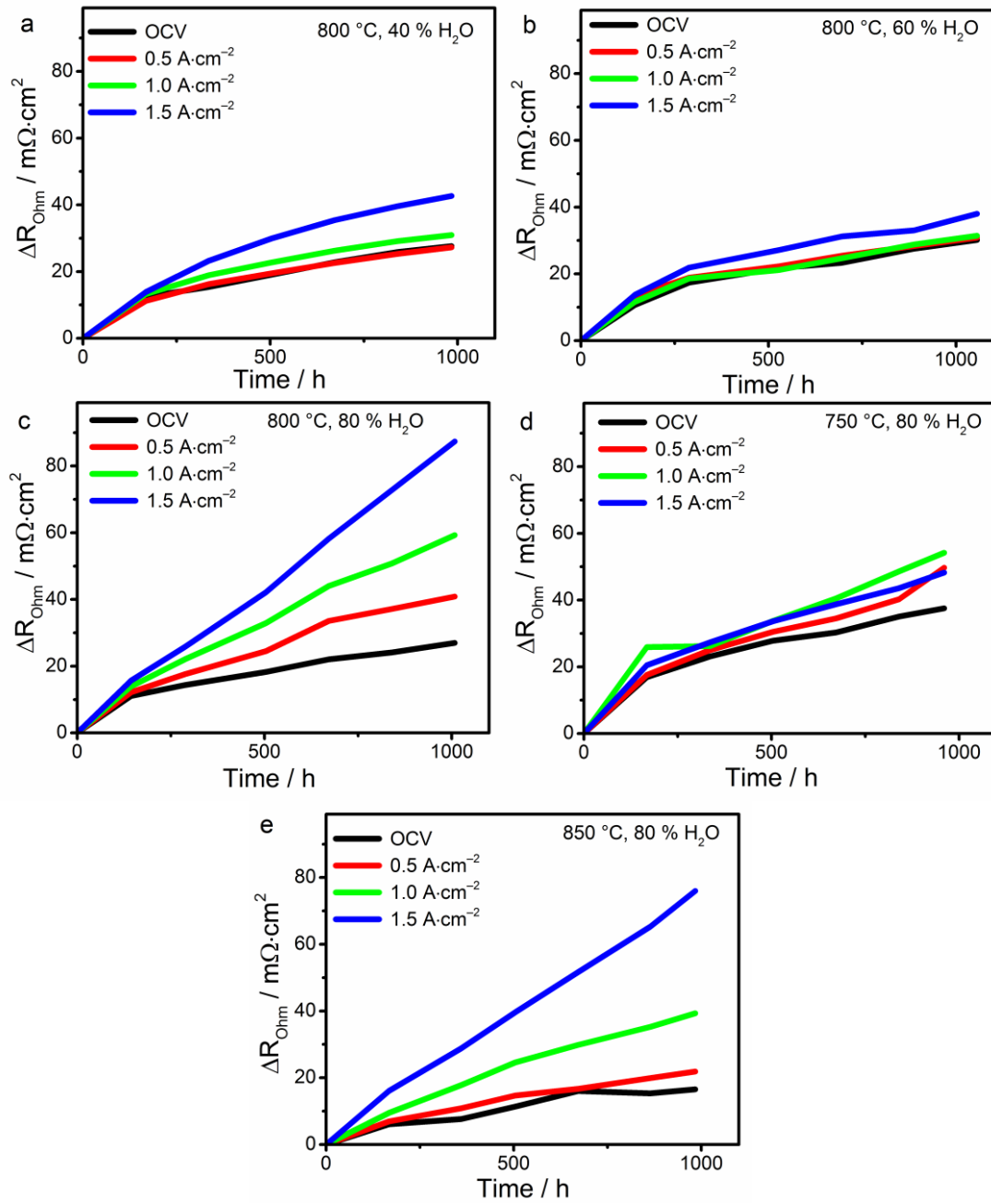


Fig. 25: Change in ohmic resistance of cells operated at different current densities and (a) 800 °C and 40 %MH, (b) 800 °C and 60 %MH, (c) 800 °C and 80 %MH, (d) 750 °C and 80 %MH, and (e) 850 °C and 80 %MH.

| | R_{ohm} 750 °C, 80 % [mΩ·cm ²] | R_{ohm} 800 °C, 40 % [mΩ·cm ²] | R_{ohm} 800 °C, 60 % [mΩ·cm ²] | R_{ohm} 800 °C, 80 % [mΩ·cm ²] | R_{ohm} 850 °C, 80 % [mΩ·cm ²] |
|-----------------------|--|--|--|--|--|
| OCV | 38 | 28 | 30 | 27 | 16 |
| 0.5 A/cm ² | 50 | 27 | 31 | 41 | 21 |
| 1 A/cm ² | 54 | 31 | 31 | 59 | 39 |
| 1.5 A/cm ² | 48 | 43 | 38 | 87 | 76 |

Table 6: Overview of the increase of ohmic resistance after 1000 h for all 20 long-term tests.

Cells operated at 40 %MH and 60 %MH show a very similar behavior, indicating that humidity has a minor effect on ohmic degradation in this range. At 80 %MH, however, a significant impact can be observed. While cells operated at OCV show an almost identical resistance increase at 40, 60 and 80 %MH, the effect of humidity increases with increasing current density. At 1.5 A/cm² the degradation of the ohmic resistance of the cell operated at 80 %MH is roughly twice as large compared to the cell operated at 40 and 60 %MH.

A clear trend with temperature can be observed for cells operated at OCV, where the strongest increase in resistance is measured for the cell operated at 750 °C, while higher temperatures leads to a smaller increase in the resistance. This trend can also be observed for cells operated at 0.5 A/cm². However, at 1.0 A/cm² the degradation of the cell operated at 800 °C is already slightly larger compared to the cell operated at 750 °C. At 1.5 A/cm² the cells operated at 800 °C and 850 °C exhibit a similar degradation which is significantly larger compared to that at 750 °C.

The fact that humidity has no influence on the resistance increase at OCV, along with the observed temperature dependence is an indication that the associated degradation at OCV is not originating from the hydrogen electrode, as will be substantiated by post mortem analysis later. It is assumed to be mainly dominated by 8YSZ electrolyte degradation and independent of current.[92] Thus, the impact of the current can be largely isolated by referring to the degradation at OCV as a baseline.

In general, during all tests a more pronounced increase of the ohmic resistance was observed with increasing current densities. At 40 and 60 %MH (800 °C) the effect of current is very similar where hardly any effect up to 1.0 A/cm² is detectable for both humidities, while a small increase at 1.5 A/cm² can be observed. However, at 80 %MH

a clear influence of the current density can be observed, where even the cell operated at 0.5 A/cm^2 , displays an increased ohmic resistance degradation compared to the cell operated at OCV. The extent of this degradation further progresses with increasing current density.

Also at $750 \text{ }^\circ\text{C}$ the influence of the current density is comparatively small. While cells operated under current show higher ohmic resistance increase than the cell at OCV, the corresponding values are very similar to each other. Thus, at $750 \text{ }^\circ\text{C}$ no clear trend regarding the influence of current density can be identified. At $800 \text{ }^\circ\text{C}$ (80 %MH) and $850 \text{ }^\circ\text{C}$, however, a clear correlation between increase in current density and enhanced degradation can be observed. At $800 \text{ }^\circ\text{C}$ the impact of current is already pronounced at 0.5 A/cm^2 ($\Delta R_{\text{ohm}} = 41 - 27 = 14 \text{ m}\Omega\cdot\text{cm}^2$) while at $850 \text{ }^\circ\text{C}$ there is only a small impact of operating at 0.5 A/cm^2 ($\Delta R_{\text{ohm}} = 21 - 16 = 5 \text{ m}\Omega\cdot\text{cm}^2$). Nevertheless, at 1.5 A/cm^2 the effect of current density on the resistance increase is very similar with $60 \text{ m}\Omega\cdot\text{cm}^2$ for both cells operated at 800 and $850 \text{ }^\circ\text{C}$. This translates into a disproportional increase in ohmic resistance with current density for both temperatures. At $800 \text{ }^\circ\text{C}$ the increase in ohmic resistance is four times larger at 1.5 A/cm^2 compared to 0.5 A/cm^2 , whereas at $850 \text{ }^\circ\text{C}$ it is more than ten times larger.

5.1.1.2 Post-test results

Results of post mortem SEM analysis are presented in the following to identify the nature and location of the observed increase in ohmic resistance.

To investigate microstructural changes in the functional hydrogen electrode layer, particularly the ones related to the Ni phase, low-energy SEM imaging was used. This technique enables distinguishing the percolated from the non-percolated Ni phase and the ceramic YSZ matrix allowing for the separation of four different phases: YSZ, pores, percolated and non-percolated Ni. The effect of this technique is exemplarily illustrated on a reduced reference sample in Fig. 26.

Fig. 27 displays the influence of the current density by showing SEM images of the electrolyte | hydrogen electrode interface of four cells operated at $800 \text{ }^\circ\text{C}$, 80 %MH and OCV, 0.5 , 1.0 and 1.5 A/cm^2 . While the SEM image of the cell operated at OCV looks very similar to the one of the reference cell, Ni depleted regions close to the electrolyte become visible with increasing current density. At 0.5 A/cm^2 this phenomenon is only apparent in certain regions, however, at 1.0 A/cm^2 and 1.5 A/cm^2 Ni depletion occurs

on a length scale of 1 – 2 μm along the whole electrolyte/hydrogen electrode interface, which results in a layer virtually depleted of Ni. Fig. 27 also reveals the existence of non-percolated Ni particles. While in cells operated up to 1.0 A/cm^2 only small amounts can be detected a significantly higher quantity can be found in the cell operated at 1.5 A/cm^2 . The analogue dependence of the Ni depletion process and the increase in ohmic resistance on current density is an indication that the behavior of the ohmic resistance degradation in Fig. 25 is associated to Ni depletion.

Fig. 28 displays how hydrogen gas humidity influences Ni depletion. All three cells presented were operated at 800 $^{\circ}\text{C}$ and high current density, that is, 1.5 A/cm^2 , since current density appears to be a driving force for Ni depletion. A Ni deprived layer is clearly formed at 80 %MH, while the cells operated at lower humidities do not show Ni depleted areas. An increased number of non-percolated Ni particles can also only be found for the sample operated at 80 %MH.

In order to reveal the influence of temperature, Fig. 29 compares cells operated at 750 $^{\circ}\text{C}$, 800 $^{\circ}\text{C}$ and 850 $^{\circ}\text{C}$, at 80 %MH and 1.5 A/cm^2 . In agreement with the observed influence of temperature on ohmic resistance increase in Fig. 25, a similar extent of Ni depletion can be observed at 800 and 850 $^{\circ}\text{C}$. At 750 $^{\circ}\text{C}$ significantly less pronounced Ni depletion was found. For this cell, certain areas at the electrolyte/hydrogen electrode interface were depleted of Ni, however, no Ni-vacated layer was formed. Only for the cell operated at 800 $^{\circ}\text{C}$ an increased number of non-percolated Ni particles can be found, while the cells operated at 750 and 850 $^{\circ}\text{C}$ do not exhibit this increase.

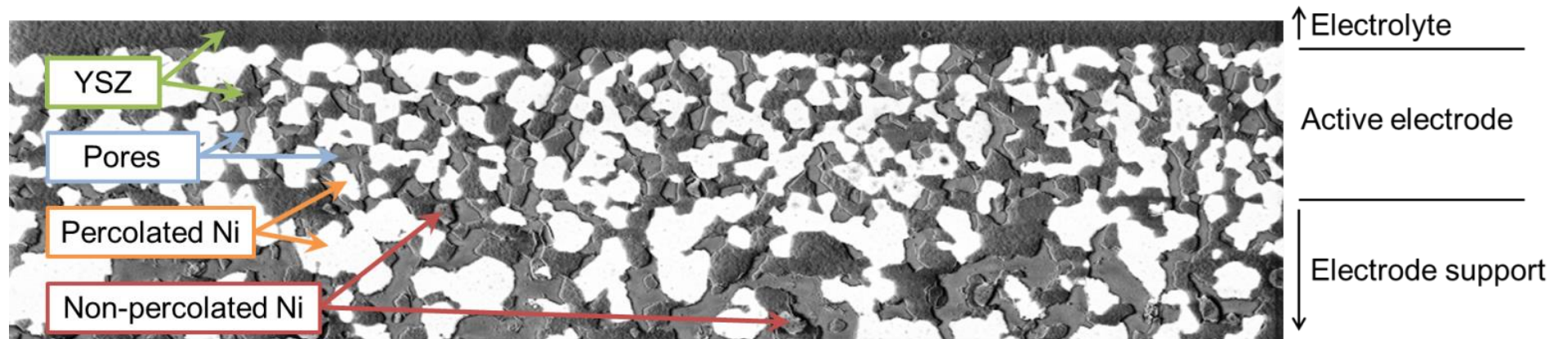


Fig. 26: SEM image of the electrolyte | hydrogen electrode interface of a reference cell. It was recorded at low acceleration voltages and without prior carbon depositing in order to distinguish the following phases: YSZ, pores, percolated and non-percolated Ni.

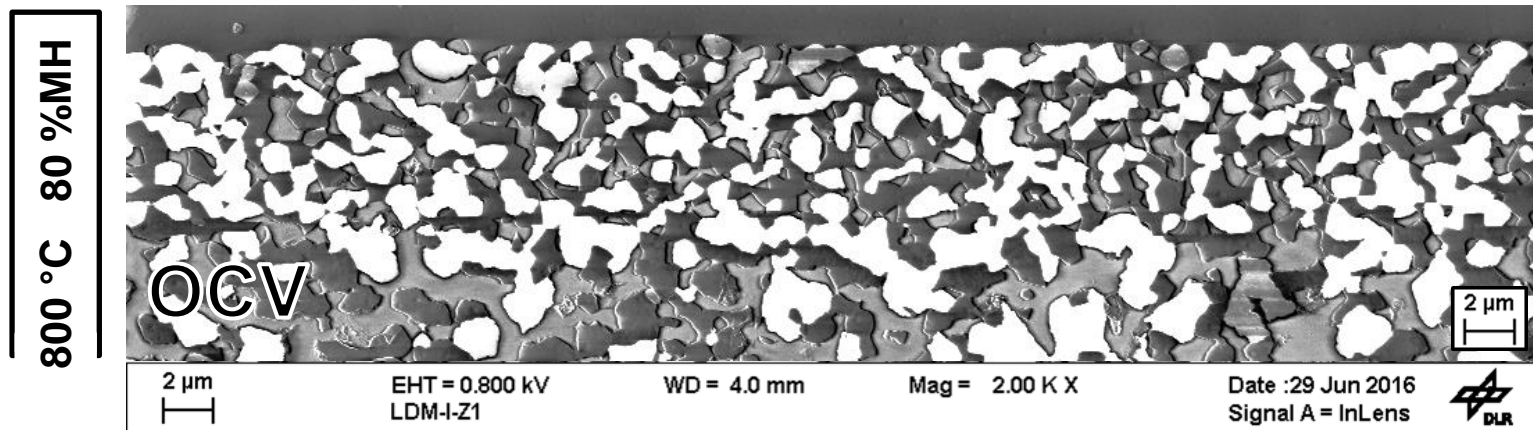
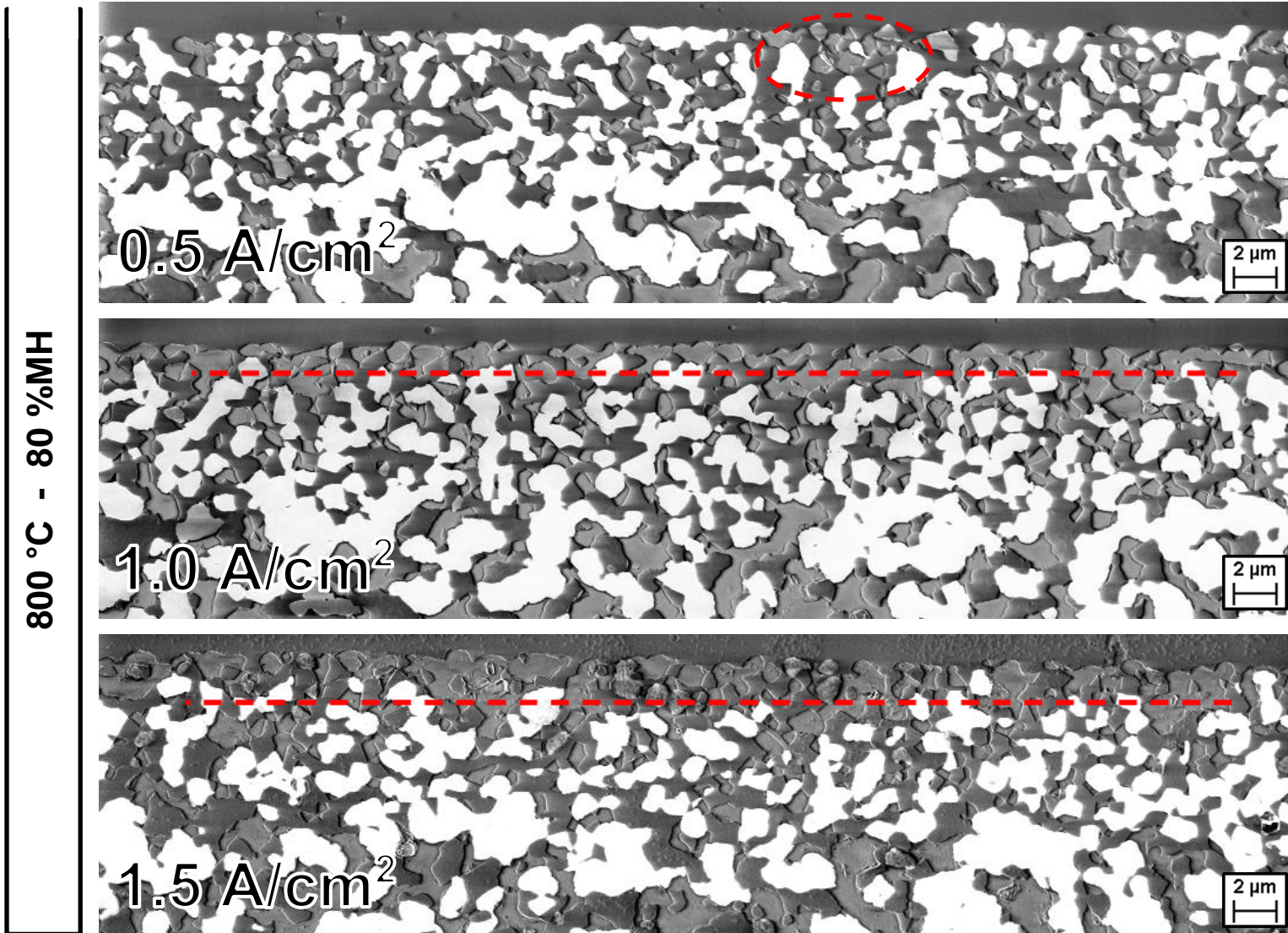


Fig. 27: Images of the electrolyte | hydrogen electrode interfaces of four cells operated at 800 °C and 80 %MH for 1000 h. The cells presented were measured at OCV, 0.5 A/cm², 1.0 A/cm² and 1.5 A/cm², respectively. The SEM-Legend displayed for the cell operated at OCV



is representative for all images of Fig.27 through Fig.29.

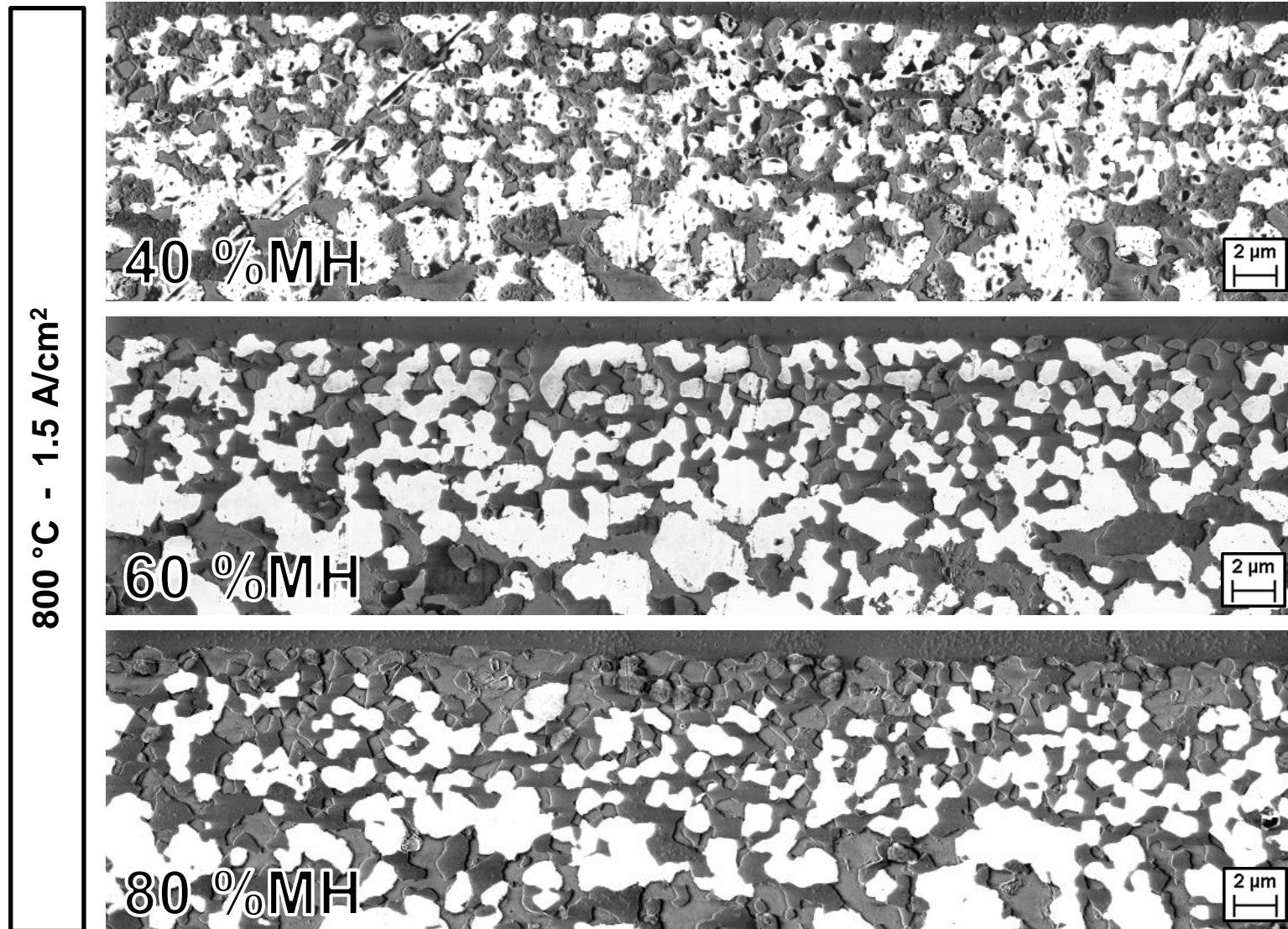


Fig. 28: Images of the electrolyte | hydrogen electrode interfaces of four cells operated at 800 °C and 1.5 A/cm². The cells presented were measured at 40 %MH, 60 %MH, 80 %MH, respectively. The dark spots in the percolated Ni-phase of the 40 %MH-image are caused by problems during sample preparation.

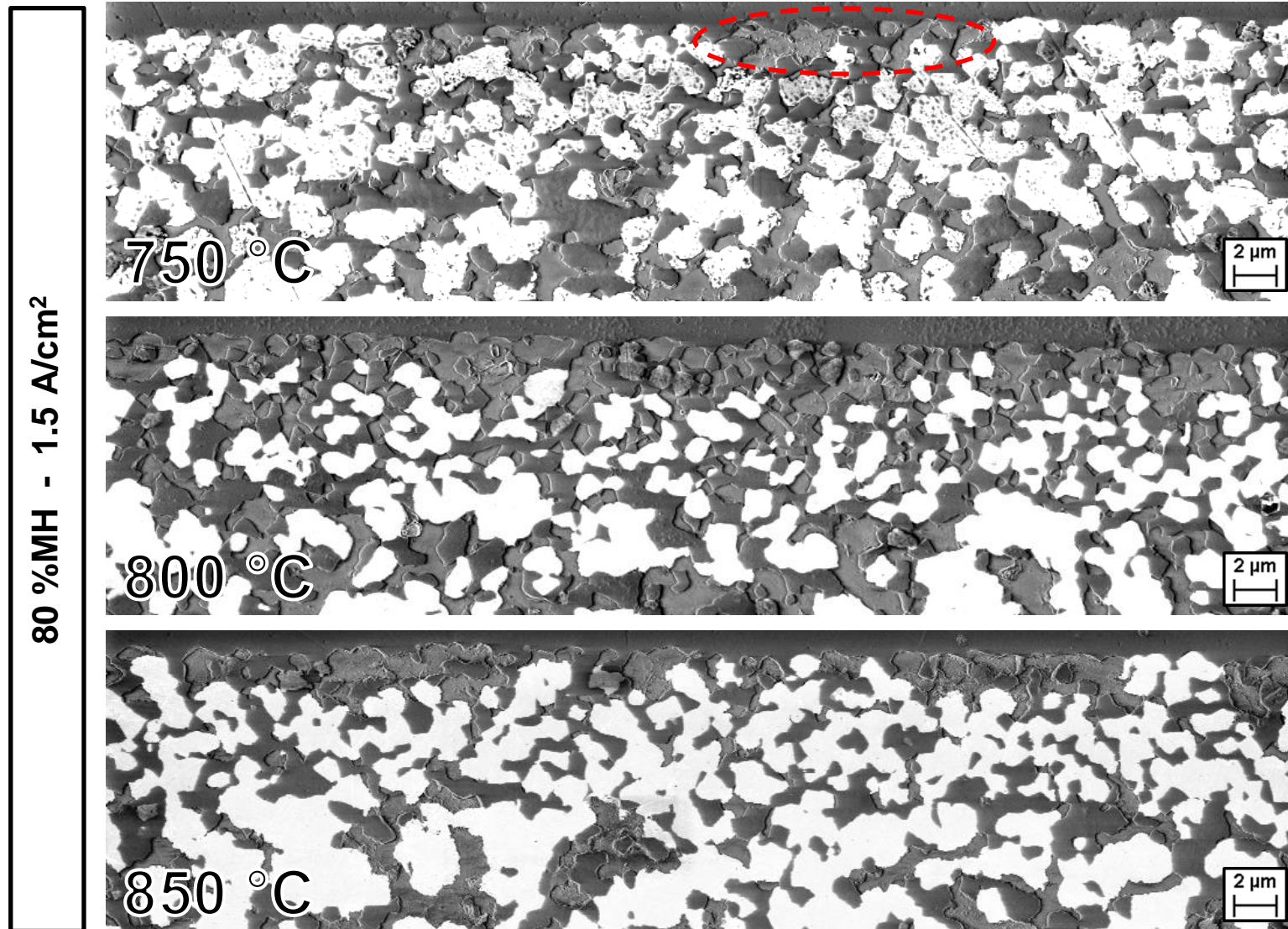


Fig. 29: Images of the electrolyte | hydrogen electrode interfaces of four cells operated at 80%MH and 1.5 A/cm² for 1000 h. The cells presented were measured at 750 °C, 800 °C and 850 °C, respectively. The dark spots in the percolated Ni-phase of the 750°C-image are caused by problems during sample preparation.

5.1.1.3 Discussion

The post-test results clearly show that – depending on the combination of operating parameters – Ni is transported unidirectionally away from the electrolyte leaving behind parts of the electrode completely deprived of Ni. For operating conditions which cause only little Ni-depletion, this is limited to small areas at the electrolyte | hydrogen electrode interface. In case of more severe Ni-depletion, a whole layer of the cermet electrode is depleted of Ni, leaving behind a layer of porous YSZ next to the dense YSZ electrolyte. Since the reaction zone is shifted away from the electrolyte the oxygen ions produced in the hydrogen electrode have to be transported through this porous YSZ layer. This represents an additional contribution to the ohmic resistance.

Cells operated at OCV display a very similar Ni distribution compared to the reference cell. Therefore, the increase of the ohmic resistance of the cells operated at OCV is not caused by Ni depletion but can be assumed to have its origin in electrolyte degradation. It is expected to occur at the same rate for cells at the same temperature, as confirmed by the values at 800 °C in Table 6.[92] Furthermore, resistance increase at low humidities (40 %MH and 60% MH), where no indication of Ni-depletion can be found by SEM imaging, behaves almost independently of current, suggesting the electrolyte degradation being independent of the applied current.

To assess the magnitude of the ohmic resistance increase due to Ni depletion, its additional resistance is estimated for the cell operated at 800 °C, 80 %MH and 1.5 A·cm⁻². In this case the Ni-depleted layer is approximately 2 μm thick. The equivalent thickness of a dense layer d_{eff} is then calculated according to

$$d_{Eff} = d_{Ni-depl} \cdot \frac{\tau_{YSZ}}{\beta_{YSZ}} \quad (5-1)$$

where volume fraction β_{YSZ} equals 0.37 in accordance with microstructural analysis (compare Table 4) and tortuosity τ_{YSZ} being 2 [93–96] which leads to a value of 10.8 μm. Typical values of 50 Ω·cm to 60 Ω·cm are reported for 8YSZ resistivity at 800 °C, which suggests that the YSZ electrolyte ($d_{YSZ} = 10 \mu\text{m}$) accounts for an ohmic resistance R_{eff} of 55 mΩ·cm² and, therefore, approximately 50 % (55 mΩ·cm²/114 mΩ·cm²) of the total ohmic resistance of the tested cells. [88, 89] With this value, the additional resistance of the Ni-depleted layer R_{eff} amounts to

$$R_{eff} = R_{YSZ} \cdot \frac{d_{Eff}}{d_{YSZ}} = 59 \text{ m}\Omega \cdot \text{cm}^2 \quad (5-2)$$

This value is in good agreement with the measured change of the ohmic resistance attributed to Ni depletion ($\Delta R_{ohm} = 87 \text{ m}\Omega \cdot \text{cm}^2 - 27 \text{ m}\Omega \cdot \text{cm}^2 = 60 \text{ m}\Omega \cdot \text{cm}^2$).

The above results show a strong correlation between the Ni depletion observed by SEM imaging and an increase in ohmic resistance. The influence of all three investigated operating parameters on Ni depletion was found to correlate with the increase in ohmic resistance. Furthermore, the calculated impact of the Ni depleted layer is in good agreement with the measured ohmic degradation (subtracted by the base degradation attributed to the other cell components). These findings strongly suggest that Ni depletion in the active hydrogen electrode is one of the major processes responsible for SOEC degradation. The established quantitative correlation between microstructural and electrochemical degradation might possibly be used for predicting the effect of Ni depletion on electrochemical degradation, once a detailed understanding of the Ni depletion mechanism and its kinetics are established.

Possible mechanism of Ni-depletion:

The observed Ni depletion in the anode functional layer is probably caused by a Ni diffusion process, either in the solid state or in the gas phase as evaporated Ni species. In general, possible drivers of these diffusion processes could be a gradient in gas composition, the potential gradient perpendicular to the electrode | electrolyte interface within the porous electrode as well as a gradient in temperature. In the following, several possible mechanisms are discussed.

Gradient in gas concentration:

During SOEC operation steam is reduced to hydrogen at the electrode and therefore conditions are increasingly reducing closer to the electrolyte as schematically depicted in Fig. 30. Since the transport of Ni via volatile species occurs along the concentration gradient towards more reducing conditions, Ni should be transported towards the electrolyte. This behavior was indeed observed by Hauch et al. for cells operated at high current densities ($2 \text{ A} \cdot \text{cm}^{-2}$ in SOEC mode) and $950 \text{ }^\circ\text{C}$. [18] However, the present study shows transport away from the electrolyte, which is consistent with other studies at operating temperatures of $850 \text{ }^\circ\text{C}$ or lower. [11, 28, 97] Consequently, the gas concentration gradient cannot be the reason for Ni-depletion.

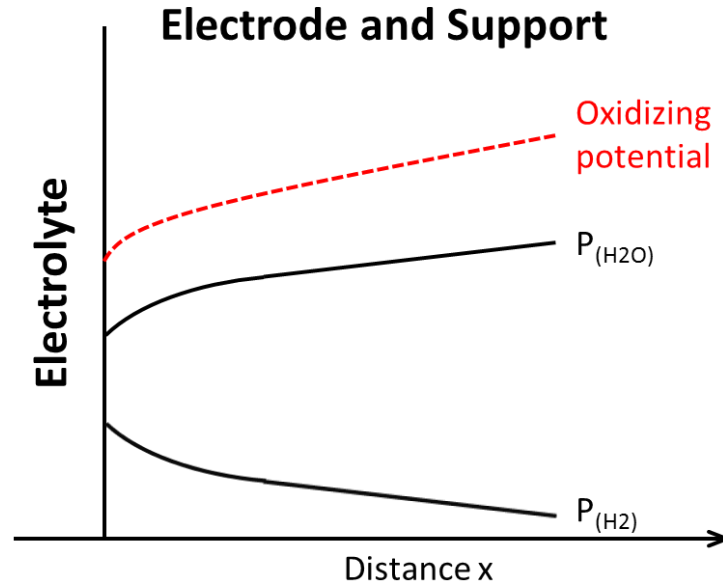


Fig. 30: Schematic depiction of the gas concentrations in a SOEC hydrogen electrode in dependence of the distance from the electrolyte. The change in gas compositions results in a gradient of the redox potential, i.e. in stronger reducing conditions closer to the electrolyte.

Difference in polarization of Ni particles:

Another possible explanation for a gradient in $a_{Ni(OH)_x}$ is a difference in the polarization of Ni particles. Due to its good electronic conductivity Ni particles within the percolation network have close to identical potential. This means that Ni particles would have to be non-percolated in order to allow for a significant difference in polarization. In fact the existence of non-percolated Ni particles can be observed to a limited degree in all cells affected by Ni depletion (compare Fig. 27 to Fig. 29).

Mogensen et al. formulated a hypothesis for the Ni-depletion mechanism based on polarization differences between Ni particles as driving force.[28] It can briefly be summarized as two steps leading to Ni depletion. The initial step is the loss of contact between Ni and YSZ particles close to the electrolyte, while two possible driving forces are suggested: First, due to the high negative polarization the volume of the YSZ particles will be slightly reduced, sufficiently for Ni and YSZ particles to lose contact. Secondly, the strong negative polarization might cause a change in interfacial energy between Ni- and YSZ-particles causing loss of contact due to dewetting. The second initial step is the loss of percolation between the Ni particles. This might again be caused by a change in interfacial energy due to the strong negative polarization. These two

steps, the loss of Ni | YSZ contact and the loss of percolation between Ni particles, were experimentally observed by Mogensen et al. [11, 26, 28, 98]. Both cause a shift of the reaction zone away from the electrode | electrolyte interface. The electrochemical potential of the isolated Ni particles is solely determined by the steam to hydrogen ratio, which is more oxidizing than that of the negatively polarized percolated Ni, leading to migration of Ni via volatile $\text{Ni}(\text{OH})_x$ -species away from the electrolyte towards the reaction zone. A schematic summary of this postulation is shown in Fig. 31, where Ni migration from electrolyte (due to potential difference) and from the support (due to gas concentration gradient) converge at the active reaction zone.

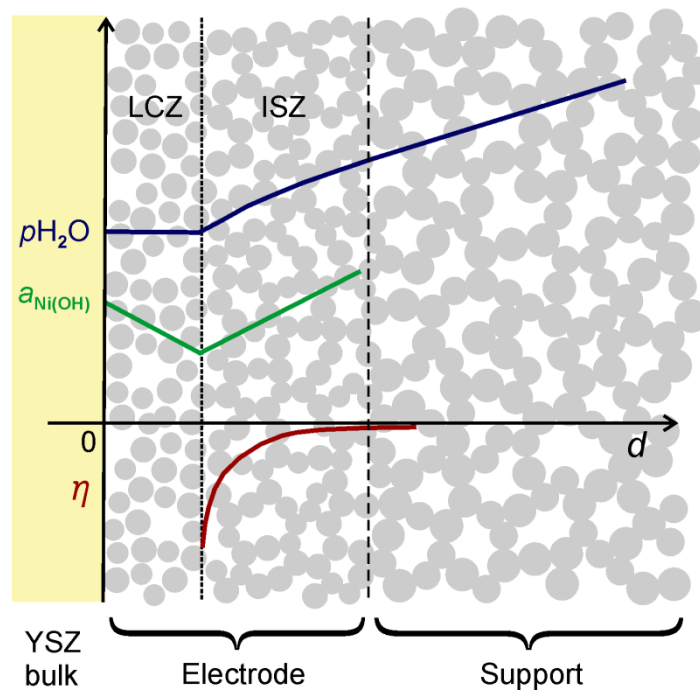


Fig. 31: Hypothesis on Ni-depletion as presented by Mogensen et al.[28]. In the electrode close to the electrolyte Ni particles have lost contact to the YSZ structure as well as to each other (Lost contact zone, LCZ). The reaction zone is shifted away from the electrolyte to the intact structure zone (ISZ). Ni migrates from the support along the steam gradient to the reaction zone, while Ni also migrates from the nonpolarized isolated particles close to the electrolyte.

It is difficult to assess how operating parameters influence the formation of isolated Ni particles due to insufficient knowledge about the mechanisms and kinetics of the underlying processes [28]. Significantly increased amounts of non-percolated Ni could only be observed for the cell operated at $1.5 \text{ A} \cdot \text{cm}^{-2}$, $800 \text{ }^\circ\text{C}$ and 80 \%MH . Consequently, no clear dependence of the investigated parameters on the formation of non-percolated Ni particles can be derived. The fact that there are cells with Ni depleted layers but no significant amount of non-percolated Ni particles could be explained if the

loss of percolation is the rate limiting step for Ni depletion at these conditions. It could also indicate that it is not the loss of percolation and the accompanying gradient in polarization which is responsible for Ni depletion. However, the present data does not allow for a clear statement.

In Fig. 32 gap formation between the Ni and YSZ phase is investigated. Fig. 32a shows a SEM image by Hauch et al. [11] that illustrates the loss of contact between Ni and YSZ phase. However, an exemplary SEM image of one of our cells operated under similar operating conditions in Fig. 32b depicts no visible similar gap formation. The absence of visible Ni-YSZ contact loss was confirmed by SEM analysis of all other cells examined in this study (not shown here). These results question whether the Ni-YSZ contact loss is indeed a prerequisite for the proposed mechanism of Ni depletion, or if the loss of Ni percolation is sufficient to trigger the Ni(OH)_x formation process. However, such a qualitative comparison of cells with different origin and possibly different microstructure and processing conditions is always difficult and is insufficient to definitely exclude the hypothesized Ni-YSZ contact loss.

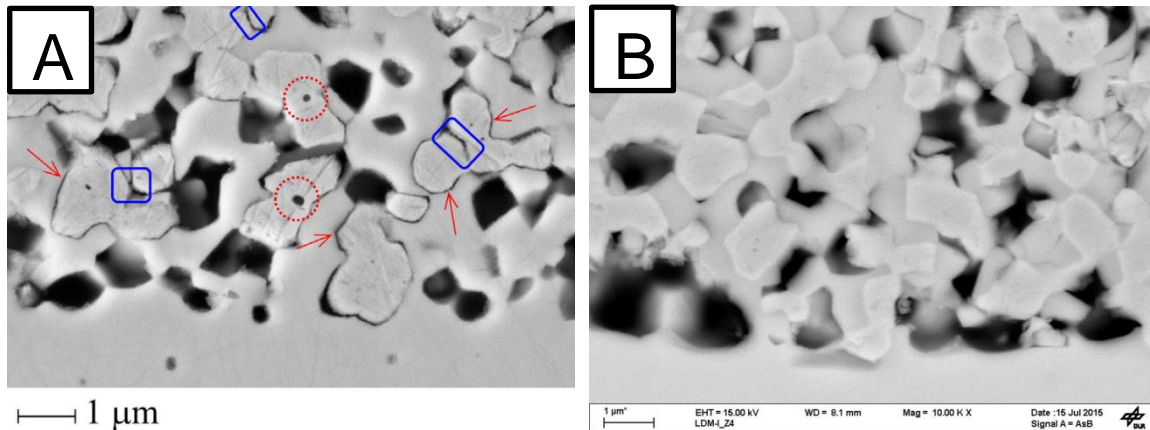


Fig. 32: Comparison of two cells operated in SOEC mode. Cell A (1000 h, 800 °C, 1.25 A/cm², 90/10 H₂O/H₂) [11] clearly shows the loss of contact between Ni and YSZ particles (red arrows). The cell in Fig. 32B (1000h, 800 °C, 1.5 A/cm², 80/20 H₂O/H₂) does not show this gap formation and is representative for the cells degraded during this study.

As mentioned before, a significant difference in potential can only occur if Ni particles lose contact to the percolation network. The question is, however, if the loss of contact between the Ni particles and the YSZ-phase is also an essential prerequisite for Ni depletion. In principle, non-percolated Ni particles that are still connected to the YSZ skeleton behave like reference electrodes. This means there is a potential difference

between them and the Ni-percolation network corresponding to the local overpotential assuming that the gas concentration at their TPB is identical for both particles as well as the chemical potential of the oxygen ions within the YSZ $\mu_{O^{2-},YSZ}$. This scenario is visualized in Fig. 33A. If the non-percolated Ni particle is closer to the electrolyte (or further away), there is an additional contribution to the potential difference. This is caused by the difference in $\mu_{O^{2-},YSZ}$ at the TBP of one particle relative to the other and corresponds to the overvoltage necessary to induce the O^{2-} -ions flux through the YSZ-shaft as displayed in Fig. 33B. This shows that non percolated Ni particles which still are connected to the YSZ backbone can indeed have a more positive potential relative to the Ni percolation network and consequently a higher $a_{Ni(OH)_x}$. Hence, the loss of contact between Ni particles and YSZ backbone is not a prerequisite for Ni depletion.

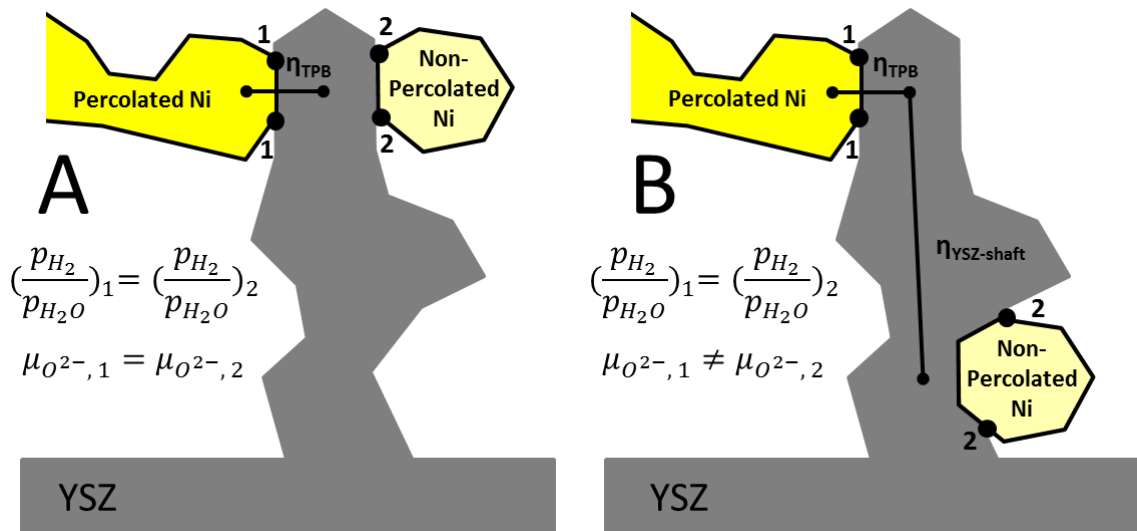


Fig. 33: Potential difference between percolated and non-percolated Ni particles both connected to the YSZ skeleton. (A) displays a scenario where the gas concentration as well as the $\mu_{O^{2-}}$ are identical, resulting in a potential difference equal to the Ni overpotential. (B) describes a scenario where both Ni particles are located at different distances from the electrolyte, resulting in an additional potential difference caused by difference in $\mu_{O^{2-}}$, i.e. the overvoltage necessary to transport the O^{2-} -ions through the YSZ shaft.

In the present study, the Ni depletion was observed to be more pronounced for higher hydrogen gas humidities. Increased hydrogen gas humidity should lead to increased $Ni(OH)_x$ formation. Thus, the observed trend is in agreement with the hypothesis of Ni transport via $Ni(OH)_x$ formation.

Moreover, a correlation of more significant Ni depletion with increased current densities was observed in the present study. As higher current densities correspond to larger cathodic (Galvani) potential steps, that is, larger overpotentials, Ni particles are more negatively polarized and stronger potential gradients emerge within the porous electrode. According to the hypothesis by Mogensen et al., this should lead to an increasing Ni-Ni contact loss and facilitated formation of volatile Ni species. Increased current densities also entail higher p_{H_2}/p_{H_2O} values, generally reducing the activity of Ni(OH)_x. However, due to the small fuel utilization values in the present study (< 20 % for all experiments) and low diffusion resistances of the used cells, this effect is probably limited. According to the hypothesis of Mogensen et al., Ni depletion can be expected to be mainly driven by the potential gradient within the porous electrode. This is consistent with the present results.

In this study, a similar extent of Ni depletion was observed for experiments at 800 and 850 °C. However, only little degradation was found at 750 °C, although hydrogen electrodes at lower temperatures are operated at significantly higher cathodic Galvani potential steps (i.e., larger cathodic overpotentials) and therefore, display larger potential gradients between percolated and non-percolated Ni. However, formation of volatile Ni species is a thermally activated process and according to thermodynamic calculations the vapor pressure of Ni gas species in a 80 %MH hydrogen gas is lowered by approximately one order of magnitude (from $5 \cdot 10^{-10}$ atm to $5 \cdot 10^{-11}$ atm) when the temperature is decreased from 850 to 750 °C.[99, 100] Thus, the high overpotentials at operating temperature of 750 °C are probably compensated for by a general decrease in Ni mobility via volatile gas species, resulting in a stable operating regime where no significant microstructural damage is caused to the hydrogen electrode.

Thus, the mechanism of Mogensen et al. is in good qualitative agreement with the parameter dependencies observed in the present study, while the lack of non-percolated particles for cells operated under most conditions is remarkable and needs to be investigated further. It should be noted that in principal the formation of non-percolated Ni particles might not be the cause of Ni relocation, but could theoretically also be its effect. Ni particles could lose connection when finer “bridges” between them are depleted, leaving behind non-percolated Ni particles. The observed interplay of the operating parameters humidity, current density and temperature in determining the occurrence and extent of Ni depletion in the hydrogen electrode demonstrates the non-linearity of this

process and underlines that a more advanced understanding of the occurring process is required to predict the onset of Ni depletion.

Electromigration:

Electromigration is the forced diffusion of charged atoms in a conductor as a result of two effects: the electrostatic force on the charged atoms resulting from the exposure to a local electrical field and the force due to the momentum transfer between electrons and the charged atoms – also referred to as “electron wind”. The electrostatic force is oriented in direction of the electrical field while the electron flow and hence their momentum is oriented in the opposite direction.[101] The occurrence of electromigration is driven by an applied current densities and the corresponding electrical field. Many studies focus on high current densities (10^4 A/cm² and above) where electromigration is reported to be effective.[101–103]

In the present study a maximum current density of 1.5 A/cm² was applied. Taking into account the Ni volume fraction of 0.45 (compare Table 4) in the cermet electrode and assuming a Ni tortuosity of 2 the effective current density in the Ni percolate amounts approximately 7 A/cm². This current density is orders of magnitudes lower compared to the previously mentioned studies. However, susceptibility strongly varies depending on operating conditions where moisture, temperature, microstructure and contamination are relevant parameters.[104] A computational study on electromigration in SOFC suggests the existence of electromigration even at 0.25 A/cm² when exposed to PH₃. [105]

The direction of ion migration due to electromigration is not readily predicted because of the two previously described driving forces opposing one another. Because of a shielding effect of the electrons the electrostatic force on the charged atoms is generally smaller and the net force is dominated by the electron momentum.[106] In SOEC operation electrons at the hydrogen electrode are conducted in the Ni percolation network towards the electrode | electrolyte interface where they are consumed in the reduction reaction. Consequently, the migration of Ni due to electromigration should lead to an accumulation of Ni at the electrode | electrolyte interface. This theoretical considerations are in good agreement with a computational study on electromigration in SOFC operation [105] where Ni transport away from the electrode | electrolyte interface is suggested due to electromigration. Furthermore, the current density in the Ni percolation network decreases closer to the electrolyte as increasingly more electrons are con-

sumed in the reduction reaction. This leads to a decreasing effect of electromigration closer to the electrolyte.

In summary it can be said that Ni migration due to electromigration might be possible at given operation conditions. However, the expected direction of Ni transport would be towards the electrode | electrolyte interface and consequently electromigration is not expected to be the mechanism behind the Ni depletion observed in the present study.

Difference in temperature of Ni particles:

Additionally to the discussed polarization gradient as driving force, there is a temperature gradient through the cell in electrolysis mode due to the heat generation at the hydrogen electrode's electrochemically active zone. This leads to a change in Ni(OH)_x activity and, thus, could contribute to Ni transport away from the electrolyte. A rough assessment of the temperature profile can be made based upon the reversible and irreversible heat losses as shown in the following. By using the standard reaction entropy values (at $\frac{p_{H_2}}{p_{H_2O}} = 1$) for hydrogen electrode ($\Delta s = 67.3 \text{ J}\cdot\text{K}^{-1}\cdot\text{mol}^{-1}$) and oxygen electrode ($\Delta s = -123 \text{ J}\cdot\text{K}^{-1}\cdot\text{mol}^{-1}$) reactions at 800 °C reported in ref.[95, 107], the reversible heat consumption can be calculated according to $\dot{Q}_{rev} = -T \Delta S$. The respective scheme of reversible heat consumption/generation at the electrodes in SOEC mode is depicted in Fig. 34a. Additionally, irreversible losses at the electrodes and at the electrolyte are taken into account as shown for an SOEC at thermo-neutral voltage in Fig. 34b. At thermo-neutral conditions the overall endothermic reversible heat consumption over the cell is compensated by irreversible losses at hydrogen electrode, electrolyte and oxygen electrode, which in this case corresponds to a total overpotential of 0.31 V. This overpotential is attributed to electrodes and electrolyte proportionally to the magnitude of their initial resistance according to Table 5. For comparison the heat generation regime of a SOFC is also illustrated for reversible conditions (Fig. 34c) and considering irreversible losses (Fig. 34d).

On the basis of this simplistic consideration of heat generation, it can be deduced that in SOEC mode there will be a temperature gradient from hydrogen to oxygen electrode and also from the hydrogen electrode functional layer to the gas channel. This would cause a higher activity of volatile Ni species at the functional layer and could contribute to Ni migration away from the electrode | electrolyte interface, where an in-

crease of 20 °C approximately leads to a factor of two in $a_{Ni(OH)_x}$. [99, 100] However, to make quantitative statements about the magnitude of this temperature gradient, and thus, a reliable estimate of its effect on Ni migration, the temperature profile in the porous electrode has to be calculated with a more sophisticated method, for example with a non-isothermal model that incorporates all necessary heat transport equations for heat conduction, convection and radiation, as implemented in ref. [108].

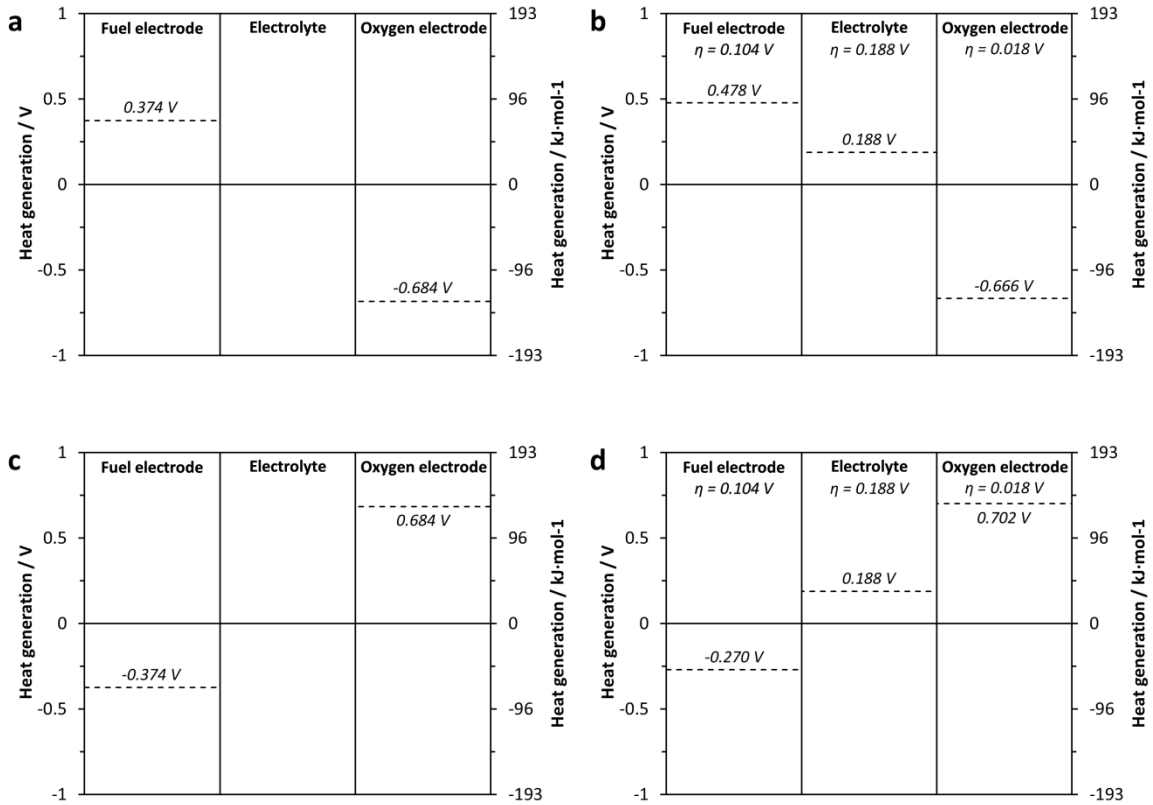


Fig. 34: Schematic depiction of local heat generation (positive voltages) and consumption (negative voltages) in electrolysis and fuel cell mode. (a) Local heat generation for a SOEC with ideally non-polarizable electrodes. (b) Local heat generation for a SOEC at thermo-neutral conditions (sum of heat source and sink terms equals zero), with reversible heat generation/consumption from (a) and irreversible terms at hydrogen electrode (P_1+P_2), electrolyte (P_0) and oxygen electrode (P_3) estimated based on initial resistance values in Table 5. (c) Local heat generation for a SOFC with ideally non-polarizable electrodes. (d) Local heat generation for a SOFC assuming the same irreversible losses as for the SOEC in (b). Heat generation based on mass transport is assumed to be negligible.

5.1.2 YSZ-aging

The phenomenon of Ni-depletion described in the last chapter does not fully account for the observed ohmic degradation. In-situ results reveal the existence of at least one other major degradation process. The following chapter will show that a decrease in conductivity of the YSZ electrolyte occurs during operation and the process will henceforth be called “YSZ-aging”.

5.1.2.1 In-situ results

As described earlier polarization is the driving force for the process of Ni-depletion. Nevertheless, degradation of the ohmic resistance can also be observed in cells operated at zero current. This reveals the existence of a second degradation phenomenon. The ohmic degradation of cells operated at OCV is displayed in Fig. 35, where the influence of temperature as well as humidity can be found. Interestingly the degradation is stronger at lower operating temperature and diminishes with increasing temperature. Additionally, no influence of the humidity on this phenomenon can be observed. The similar result of cells run at different humidities also implies a good reproducibility of this process. Furthermore, all cells show identical behavior in that they undergo a rapid initial deterioration and afterwards demonstrate a diminishing progression.

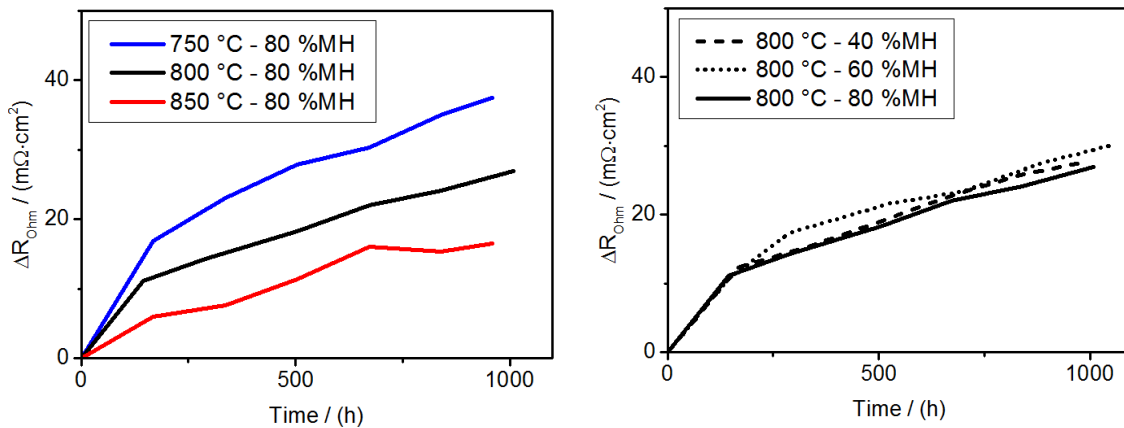


Fig. 35: Degradation of the ohmic resistance at OCV and different temperatures (left) and different humidities (right).

All of the above mentioned findings refer to cells operated at OCV. However, this does not mean that the described form of degradation only occurs at zero current. The comparison of cells operated under current load but conditions where no Ni-depletion was observed (i.e. cells operated at 40 %RH and 60 %RH, compare Fig. 28) shows that

the ohmic degradation is almost identical for those cells¹⁰. This suggests that the here described degradation phenomenon occurs under all investigated operating conditions and is largely independent of applied current density.

In Fig. 36 the change in ohmic resistance was plotted against the square root of time. It reveals that the degradation progresses at a rate proportional to $t^{0.5}$. This finding provides further information about the degradation mechanism and will be discussed in detail later on.

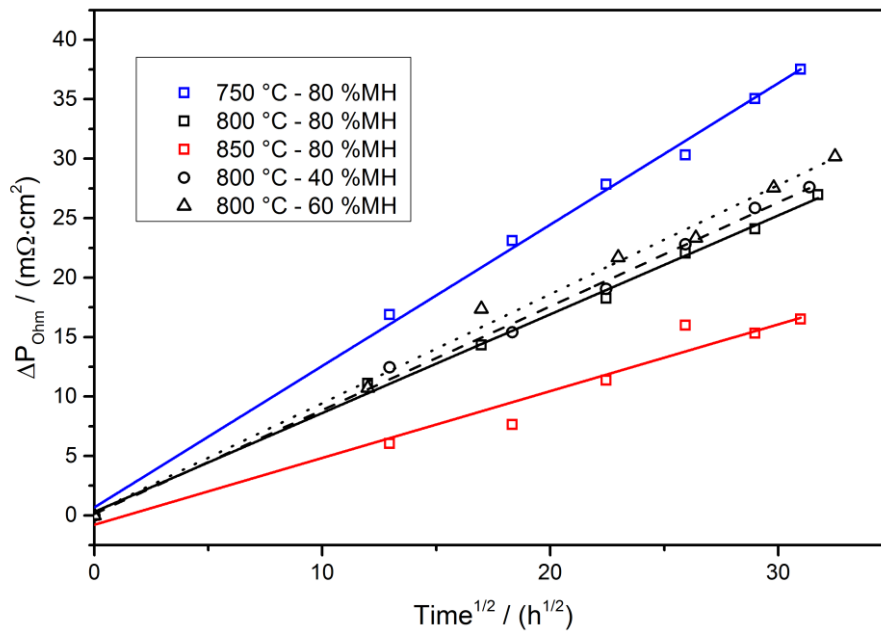


Fig. 36: Time dependence of ohmic degradation at OCV based on the square root time.

5.1.2.2 Post-test results

The difficulty in interpreting ohmic degradation originates from the several different processes which are included in the ohmic resistance. Apart from the electrolyte mainly the electronic conductivity of the MIEC oxygen electrode and the CGO diffusion barrier layer contribute. Both of these were subjected to post-test investigations which are presented in chapters 5.2 and 5.1.3, respectively. However, no correlations with the de-

¹⁰ While the mentioned cells show only small differences, at high current densities slightly higher ohmic degradation can be observed. This difference is small compared to the degradation of cells at OCV or low current densities. It is very well possible that the small variation is caused by the onset of Ni depletion or a further degradation mechanism and the process of YSZ-aging is completely independent of polarization.

scribed in-situ findings were present and no explanation, especially for the curious temperature dependence, could be found. The following section will solely address experimental results of changes to the YSZ electrolyte, while other ohmic contributions will be presented in their respective chapters.

The YSZ electrolyte was examined by SEM imaging and EDS analysis. These do not reveal any changes that could explain the previously described ohmic degradation. As they cover some other often discussed degradation mechanisms their results will be presented and further discussed in chapter 5.1.3.

Due to insufficient lateral resolution of the X-ray diffractometer (XRD), analysis of the electrolyte cannot be conducted without prior removal of electrode and diffusion barrier layer. Unfortunately, this is very difficult to achieve and it is impossible to ensure sample integrity during preparation. Consequently no XRD measurements were conducted, which could further elucidate phase composition.

The electrolyte was instead analyzed using high resolution Raman spectroscopy. As presented by Hattori et al.[58] Raman spectroscopy can be used to identify the crystallographic nature of the YSZ phase. The Raman spectra of the reference cell and two cell operated at 80 %MH, OCV and 750 °C and 850 °C, respectively are shown in Fig. 37A. All three samples show distinct characteristics of tetragonal YSZ [109–111], while the double peak between 600 cm^{-1} and 650 cm^{-1} reveals the existence of the cubic phase.[58] This is unexpected as 8YSZ is generally believed to be fully stabilized in the cubic phase down to room temperature [112, 113]. Possible explanations for the existence of tetragonal phase in the reference sample can be found in the production procedures and are possibly linked to insufficient sintering time or temperatures [114].

In order to detect changes to the phase composition during operation, the area normalized Raman spectra of the reference cell was compared to the spectra of operated cells, as shown in Fig. 37B. In both cases the difference demonstrates distinct characteristics of the spectrum of tetragonal YSZ revealing that tetragonal phase is being formed during operation. Furthermore, Fig. 37C shows that the tetragonal phase is more pronounced for the cell operated at 750 °C compared to the cell operated at 850 °C.

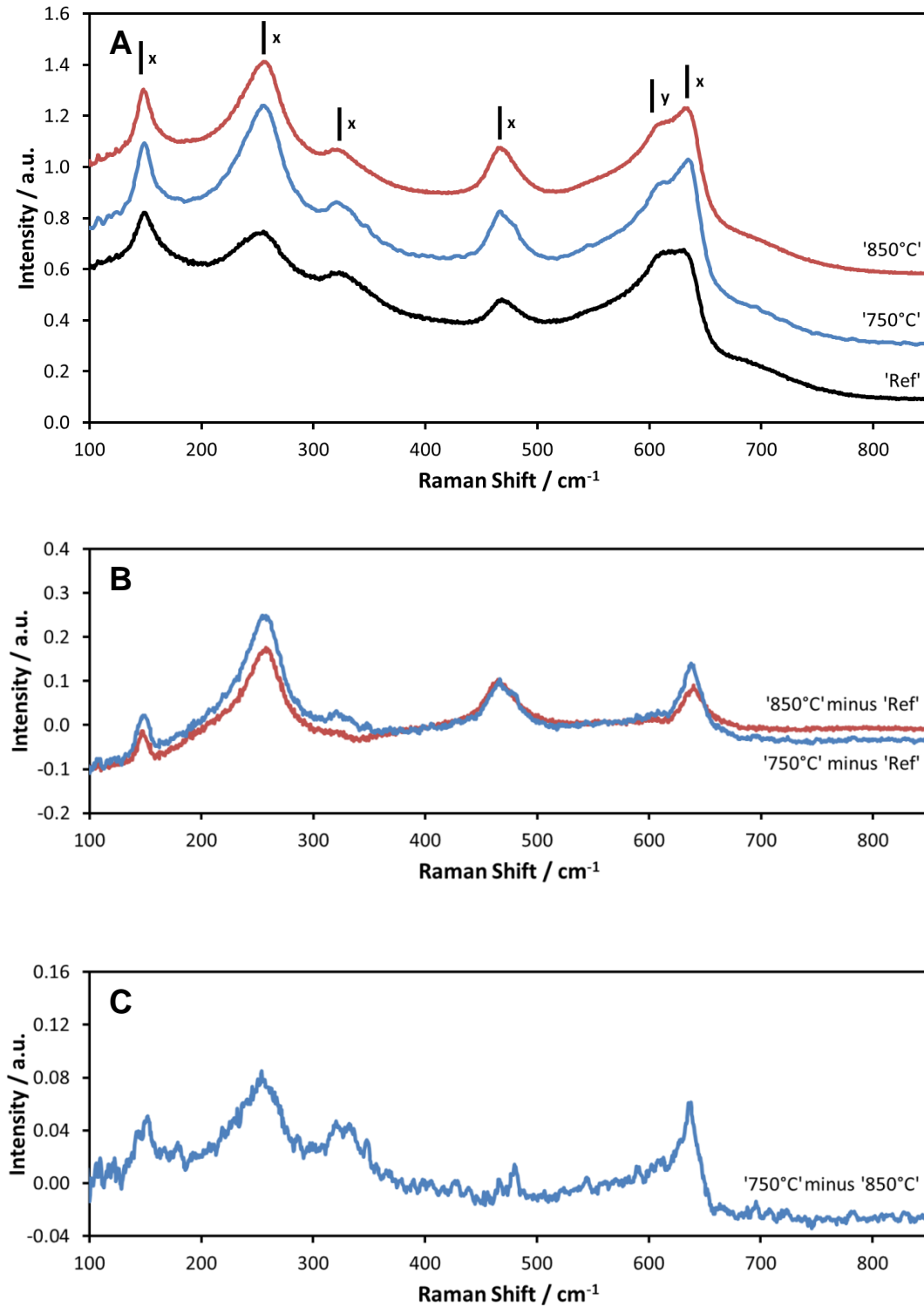


Fig. 37: (A) Area normalized Raman spectra of two cells operated at 750 °C and 850 °C, respectively, in comparison with the reference cell. For better visualization intensities of cell '750 °C' are shifted by 0.25 and of cell '850 °C' are shifted by 0.5. Peaks dominant in the spectrum of tetragonal and cubic phase of YSZ are marked with **x** and **y**, respectively. (B) Difference between spectra of operated cells and reference sample (C) Difference between spectra of cells operated at 750 °C and 850 °C. Degraded cells were operated at OCV and 80 %MH.

5.1.2.3 Discussion

Deterioration of the ionic conductivity of YSZ during heat treatment is a complex phenomenon which has been subjected to many an investigation in the last two decades of the previous century and still is up to now. Many alternative explanations for experimentally observed YSZ-aging have been postulated where even more pronounced theories often lack kinetic description [55]. Although, previous studies cover a wide variety of dopant levels and temperatures, most focus on YSZ deterioration at 1000 °C – the temperature originally expected for SOFC operation. In 1998 Kondoh et al. conducted an extensive study while reviewing many previous studies.[55, 56, 57 and references therein] They identified phase transformation towards lower symmetrical crystal structure at higher temperatures (1200 °C and above) and short range ordering of oxygen ion vacancies towards Zr^{4+} at lower temperatures (800 °C and 1000 °C) to be likely responsible for YSZ-aging. However, more recent studies [58, 59] reveal the existence of tetragonal phase in 8YSZ even at 1000 °C and 950 °C, respectively and conclude a correlation between tetragonal phase and decrease of ionic conductivity. Both these studies target the influence of dopant level on the YSZ-aging and show that significant aging occurs at 8YSZ which decreases with increased dopant level towards 10YSZ. Nevertheless, to the author's knowledge there is no recent study investigating the influence of temperature around 800 °C comparable to the observations of this study.

The formation of a lower symmetry phase and the accompanying compositional change would explain a decrease in ionic conductivity and the resulting increase in ohmic resistance observed. This is in good agreement with the findings of the Raman investigation. Fig. 37A shows that in operated cells, as well as in the reference sample both tetragonal and cubic phase exist. The tetragonal characteristics, however, increase during operation as presented in Fig. 37B. Also the in-situ correlation, that degradation is stronger at lower operating temperatures is reflected in the Raman study, as shown in Fig. 37C, where the cell operated at 750 °C exhibits a larger intensity of tetragonal phase compared to the cell operated at 850 °C. This correlation between in-situ and post-test analyses strongly suggests that indeed a phase transition towards tetragonal phase is responsible of the increase in ohmic resistance.

The phase compositions of YSZ at thermodynamic equilibrium in dependence of temperature and Yttria doping level can be extracted from the Yttria-Zirconia phase diagram. Since Duwez et al. [115] first published their original phase diagram many a

study was conducted refining and improving it. One of the most recent versions published by Lakiza et al. [116] in the year 2006 is displayed in Fig. 38. Additionally, to the boundaries of the respective thermodynamically stable phases, lines marking metastable diffusionless transformation were introduced, which mark the respective conditions where a phase transformation from cubic phase to tetragonal phase or from tetragonal phase to monoclinic phase can occur without the necessity for diffusion (line 1 and line 2, respectively). This is of great importance as cation diffusion in YSZ is slow at relevant operating temperatures leading to kinetically stabilized systems [55, 113, 117]. The slow diffusion of Y^{3+} in YSZ is illustrated in Fig. 39 by presenting the time necessary to reach a mean diffusion distance of 1 nm, 5 nm and 15 nm for Y^{3+} compared to 1 μm , 5 μm and 15 μm for O^{2-} in dependence of temperature.

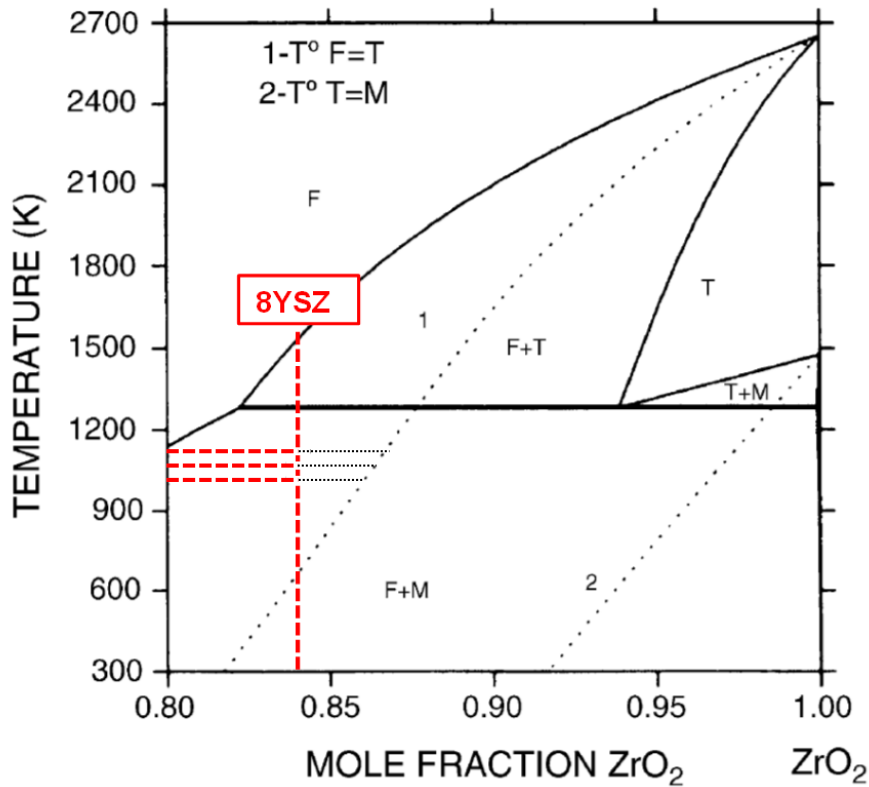


Fig. 38: Zirconia-Yttria phase diagram according to Lakiza et al. [116] including the lines (dotted) for metastable diffusionless transformation from cubic to tetragonal (line 1) and from tetragonal to monoclinic (line 2).

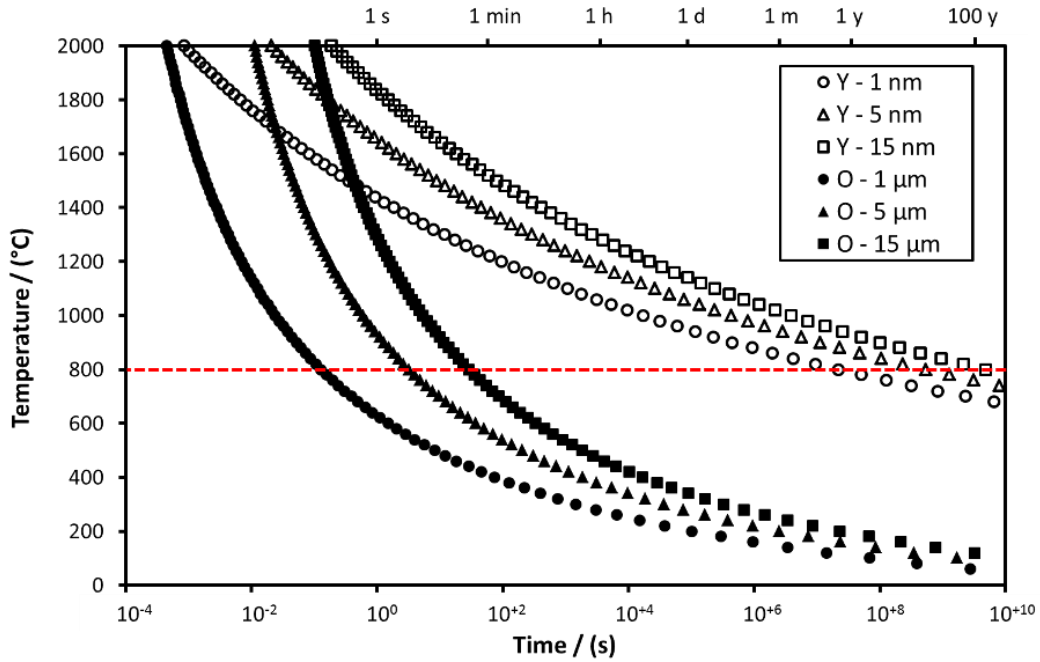


Fig. 39: Temperature required to achieve a mean diffusion distance of 1 nm, 5 nm and 15 nm for Y^{3+} and of 1 μm , 5 μm and 15 μm for O^{2-} after a certain time in YSZ. Calculation is based on diffusion data extracted from [113, 118, 119].

The phase diagram reveals that the three operating temperatures investigated in this study are all within the cubic + monoclinic area. This means that the originally cubic YSZ (due to sintering at 1230 °C) is not thermodynamically stable at these conditions but would eventually separate into two phases after indefinite time. This process, however, can only occur by cations diffusing to establish the respective thermodynamically (meta-)stable compositions of the respective phases. Since cation diffusion is very slow in YSZ [55, 113] this process is strongly kinetically stabilized. Also the phase transition towards lower symmetry does not happen directly from cubic to monoclinic but in two steps via the tetragonal phase. The underlying mechanism of this phase transition will be discussed in the following, by investigating possible rate limiting steps, analyzing their parameter dependencies and finally comparing them to the experimental findings of this study.

Diffusion limited growth:

Schelling et al. [120] concluded from their molecular dynamics simulation that the phase transition cubic to tetragonal is first order, which means that its kinetics are limited by nucleation and growth. Furthermore, the model of Fan and Chen [121] on the

microstructural evolution of YSZ phase transitions, which coincides well with previous experimental studies is also based on first order phase transition kinetics.

The diffusion controlled and interface controlled nuclei growth can be given in the following compact form [122]. At time t , the volume Y of a particle nucleated at time τ is calculated by:

$$Y(t, \tau) = g \left(\int_{\tau}^t v \cdot dt \right)^{\frac{d}{m}} \quad (5-3)$$

where g is the particle geometry factor in $\frac{m^3}{m-d}$, v is the growth velocity, d is the number of dimensions in which the particle grows and m is the growth mode parameter.

Assuming the growth of a spherical particle g will be given as $\frac{4}{3}\pi$ and d equals 3.[123] As described earlier, phase transition of 8YSZ at relevant operating temperatures can only occur with the involvement of diffusion. In the case of long range diffusion the growth mode parameter m becomes 2.[124] Assuming the particle was nucleation at the time $\tau = 0$ equation (5-3) will simplify to:

$$Y(t) = \frac{4}{3}\pi \left(\int_0^t v \cdot dt \right)^{\frac{3}{2}} \quad (5-4)$$

In case of diffusion controlled growth the growth velocity v can be substituted by:

$$v = D_{Y,YSZ}(T(t)) = D_0 \cdot e^{\left(\frac{-E_D}{RT(t)}\right)} \quad (5-5)$$

with $D_{Y,YSZ}$ as the temperature dependent diffusion constant for Y^{3+} in YSZ, D_0 as the pre-exponential factor, E_D as the activation enthalpy of diffusion and R as the universal gas constant [125]. Since temperature remained constant for the duration of the degradation experiments equation (5-4) evolves to

$$r(t) = (D_0 \cdot e^{\left(\frac{-E_D}{RT}\right)})^{\frac{1}{2}} \cdot t^{\frac{1}{2}} \quad (5-6)$$

assuming growth of a spherical particle.

The growth rate of the radius of such a particle is in good agreement with the experimentally observed time dependence of the degradation of the ohmic resistance as presented in Fig. 36. The temperature dependence on the other hand is a more complex matter. With increasing temperature the diffusion coefficient $D_{Y,YSZ}$ and hence the

growth rate of the particle increases. However, the concentration difference between the homogeneous 8YSZ solution and the concentration of metastable transformation is strongly temperature dependent. Fig. 38 reveals that at 850 °C the concentration difference is larger compared to 800 °C and again compared to 750 °C, as represented by the black dotted lines. Simplified calculations show that the effects of increased diffusion and larger concentration difference at higher temperatures roughly counterbalance other with a slightly stronger influence of concentration difference. Uncertainties especially concerning the phase diagram make a more detailed calculation unreliable.

These theoretical considerations show that diffusion limited growth does not only match the observed kinetics, but could also account for the observed temperature dependence.

Nucleation kinetics:

The kinetics of nucleation are complex and there is a variety of different modes with different time dependencies including $\propto t^{\frac{1}{2}}$. Most of these are based on the classical theory of nucleation rate. It states that the rate of formation of particles of supercritical size per unit volume \dot{N} can be given by

$$\dot{N}(T(t)) = N_0 \cdot e^{\left(-\frac{\Delta G^*(T(t))+Q_N}{RT(t)}\right)} \quad (5-7)$$

where N_0 is the temperature independent nucleation rate, ΔG^* the critical free energy for nucleus formation and Q_N the activation energy for the jumping of atoms through the matrix | nucleus interface.[125] This is only valid if merely a small fraction of the original phase is transformed so that particle growth is unaffected by one another [124].

The temperature dependence of nuclei growth is ambiguous. In case of large undercooling ΔG^* becomes negligible compared to RT and consequently the nucleation rate increases with temperature. However, at low undercooling ΔG^* can become large, significantly increasing nucleation rate by a temperature reduction.

In general however, a polycrystalline sample with preexisting tetragonal phase, grain boundaries and defects should provide sufficient nucleation seeds, so that nucleation does not become rate limiting.

Short range ordering of oxygen vacancies

In contrast to the formation of tetragonal phase [58, 59] limited by nucleation and growth Kondoh et al. identify short range ordering of oxygen vacancies (SRO) as explanation for aging of 8YSZ at 800 °C and 1000 °C in their previously mentioned study [55–57]. Although, this does not coincide well with the Raman findings of this thesis SRO will be discussed briefly. Their theory states that oxygen vacancies aggregate in the vicinity of Zr^{4+} ions in order to relax anisotropic distortion in the crystal lattice caused by Ytria doping. These oxygen vacancies are not inactive for oxygen ion transport, but require higher activation energy of migration thereby reducing the ionic conductivity.

SRO was also observed by Butz et al. [59] before and after aging of samples. Their results indicate that no significant change in SRO occurred during aging. However, quantification of this phenomenon was unfortunately not possible, which is why they could not exclude a change to the SRO.

In analogy to long range ordering Kondoh et al [55] conclude that thermodynamically SRO is more distinct at lower temperatures. Their kinetic considerations state that the diffusion of O^{2-} -ions contributes to the SRO formation kinetics. To address the complex phenomenon the concept of mean first passage time should be adapted. Unfortunately, the announced study on detailed kinetics was never published. Furthermore, it should be noticed that Kondoh's experimental results for the aging of 8YSZ at 800 °C do not coincide with the experimental results of this study as they show decreasing slope when plotting ΔR versus $t^{\frac{1}{2}}$ [55].

Summary:

Experimental findings suggest that a diffusion limited phase transition from cubic to tetragonal YSZ is most likely rate limiting for this degradation process. The diffusion limitation coincides well with the time dependence, while the temperature dependence can be explained with the concentration gap towards the composition of metastable diffusionless transformation, which decreases with decreasing temperature. Considering

that the YSZ phase diagram is continuously being improved¹¹, especially the lines of metastable diffusionless transformation are prone to errors.[112] Assuming a minor uncertainty towards higher Ytria concentrations the diffusion limited phase transition as rate limiting mechanism of degradation does account well for all experimental observation.

5.1.3 Further investigations regarding ohmic resistance

Diffusion barrier layer:

A commonly observed degradation phenomenon is the diffusion of components of the oxygen electrode perovskite through the diffusion barrier layer and the subsequent reaction to form undesirable phases, such as SrZrO_3 or $\text{La}_2\text{Zr}_2\text{O}_7$. [126] This was investigated in the operated cells by EDS linescans through the electrolyte and CGO towards the oxygen electrode as shown in Fig. 40A. For comparison, the measured intensities were normalized to the average intensity of Zr within the YSZ electrolyte of each respective sample. The distribution profile of Zr, Y, Sr and La of various operated cells are presented in Fig. 40C through F, respectively, where the YSZ|CGO interface and the CGO|LSCF interface are located at approximately 14 μm and 18 μm , respectively. No deviation between operated of reference sample can be observed for Zr or Y. The stated intensity of Y within the LSCF layer can be explained by the overlapping EDS peaks of Y and Sr. No change in La intensity at the electrolyte was measured in any sample, meaning that the formation of significant amount of La-Zr-oxides during operation can be excluded. The concentration of Sr did not change in most samples compared to the reference cell. Only the cell operated at 850 °C and to a limited amount the cell operated at OCV show an accumulation of Sr at the YSZ|CGO interface. The SEM image of the linescan of the cell operated at 850 °C reveals the existence of an irregular indent at the location in question (compare Fig. 40B, dashed circle). However, this appears to be an isolated phenomenon which was not found repeatedly. Furthermore, in-situ results show no indication of increased ohmic degradation of this specific cell rela-

¹¹ The slow diffusion makes it difficult to experimentally investigate phase transitions. Obviously, achieving steady state becomes increasingly problematic with decreasing temperature. Since the lines of metastable diffusionless transformation are calculated based on the thermodynamically stable phase transition lines, an inaccuracy has to be expected [116, 148].

tive to others. The slightly increased Sr concentration at the YSZ | CGO interface of the reference cell has to originate from cell manufacturing. No indication of significant Sr diffusion due to cell operation could be detected. The Sr signal measured within the electrolyte can be attributed to the presence of Y as previously explained.

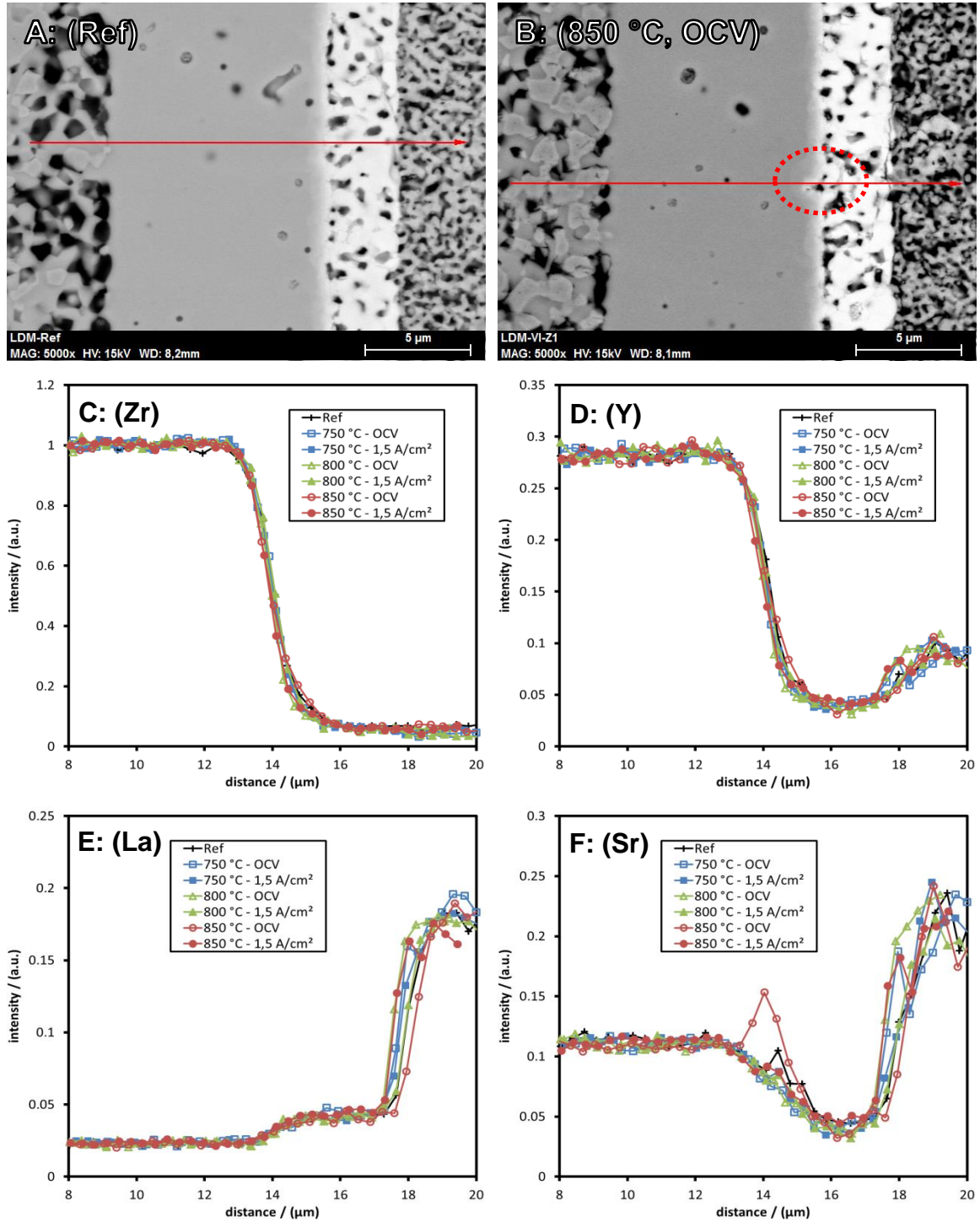


Fig. 40: EDS line scans through electrolyte and diffusion barrier layer towards oxygen electrode. (A) and (B) show SEM images of linescan location of reference cell and cell operated at 850 °C and OCV, respectively. The dashed red circle shows a singular indent with increased Sr concentration. (C) to (F) show the intensity profiles of Zr, Y, La and Sr for various investigated cells.

Microstructural deterioration:

Another often reported degradation phenomenon is the delamination of the oxygen electrode or the formation of cracks at the YSZ | CGO interface. This occurs under high polarization, if the oxygen partial pressure within the electrolyte increases above a certain level as often observed experimentally and theoretically explained by Virkar.[127 and references therein] More recently, the formation of nanometer sized pores at grain boundaries of the YSZ electrolyte was reported after 9000 hours of electrolysis operation.[27, 41]

Fig. 41 presents SEM images of the electrolyte of the reference cell, and cells operated at 1.5 A/cm^2 at $750 \text{ }^\circ\text{C}$, $800 \text{ }^\circ\text{C}$, and $850 \text{ }^\circ\text{C}$, respectively. No distinct alteration of the electrolyte can be observed in the cells operated at $800 \text{ }^\circ\text{C}$ and $850 \text{ }^\circ\text{C}$, while the sample operated at $750 \text{ }^\circ\text{C}$ showed signs of minor deterioration. This observation could be explained by larger potential gradients for the same current density at lower temperatures and is in good agreement with the previously mentioned studies. The shorter operating time compared to the study presented by The et al. [27] and Tietz et al.[41] could also explain the lack of more severe deterioration, especially at higher temperatures.

In-situ results show no significant ohmic degradation which can be attributed to microstructural deterioration of cells. A minor effect can possibly be found in cells operated at 40 %MH and 60 %MH which show almost identical degradation from OCV up to 1.0 A/cm^2 , while only at 1.5 A/cm^2 an increase can be observed. This additional deterioration could be the result of an onset of microstructural degradation which is just not detectable in SEM. However, the results do not allow for an unambiguous assignment of this minor effect.

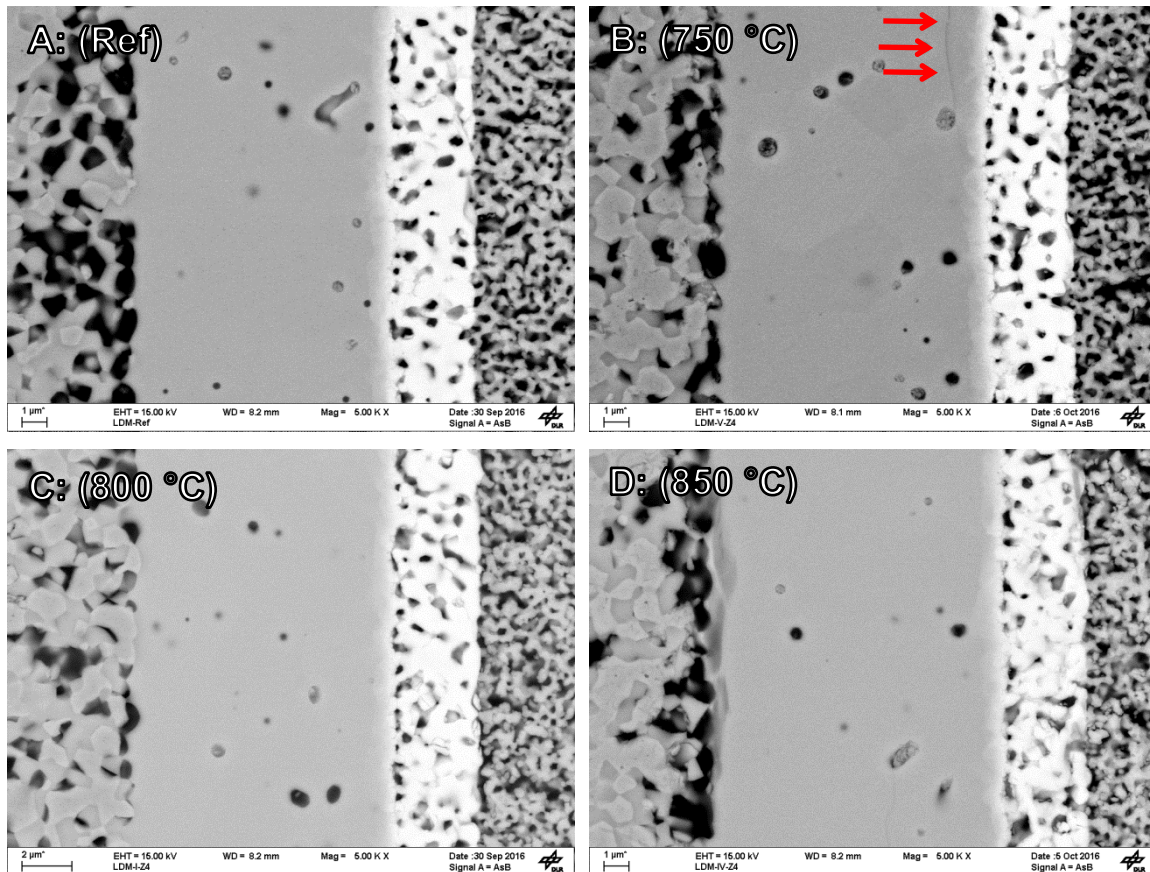


Fig. 41: SEM images of electrolytes of different cells for comparison of microstructural integrity. (A) reference cell, (B), (C) and (D) cells operated at 1.5 A/cm², 80 %MH and 750 °C, 800 °C and 850 °C, respectively.

5.2 Oxygen electrode resistance

5.2.1 In-situ results

The oxygen electrode was also subjected to significant degradation as documented in Fig. 42 and Fig. 43. Cells operated under different current densities but otherwise identical conditions show significantly different increases in oxygen electrode polarization resistance. However, no obvious trend which could be attributed to differences in polarization can be found. Instead there appears to be scattering between different cells concerning this process. Fig. 42C for example shows the degradation of cells operated at 850 °C, 80 %MH and different current densities. The cells operated at OCV and 1.0 A/cm² show similar and both significantly higher rates of degradation compared to

the cells operated at 0.5 A/cm^2 and 1.5 A/cm^2 . The fact that the timeline of each individual cell exhibits a continuous behavior clarifies that data acquisition or interpretation is not the source for this scattering, but instead differences between the cells or experimental conditions are responsible. A general trend can be observed that cells operated at 1.0 A/cm^2 and exhibit stronger degradation compared to cells run at different current densities but otherwise identical conditions. The same was observed for cells operated at OCV in 3 out of 5 cases (Fig. 42C and Fig. 43B & C). In each degradation experiment the same measurement position within the test-rig was used for the same current density, suggesting a systematic influence of the test-rig to this position. The nature of this postulated systematic influence is yet to be determined by the time of writing this dissertation.

Following the observation that the current density has no significant influence on the degradation, one approach to make the data better revisable is the introduction of the average degradation rate for all cells operated at the same temperature and hydrogen gas humidity. Fig. 42 displays the influence of temperature on the oxygen electrode degradation. At $750 \text{ }^\circ\text{C}$ only a very limited increase with an average of approximately $7 \text{ m}\Omega\cdot\text{cm}^{-2}$ can be observed after 1000 h of operation. An increase of operating temperature to $800 \text{ }^\circ\text{C}$ leads to a significantly increased degradation rate roughly 2.5 times larger compared to $750 \text{ }^\circ\text{C}$. At $850 \text{ }^\circ\text{C}$ the average degradation rate is again slightly higher compared to $800 \text{ }^\circ\text{C}$. However, it should be noted that especially at $850 \text{ }^\circ\text{C}$ there is a large deviation from mean since here additionally to the 1.0 A/cm^2 line the OCV line shows strongly increased degradation.

A second approach to negate the observed scattering is based on the assumption that an unknown source causes individual cells to degrade faster. Consequently, these cells could be neglected and only “unaffected” ones be considered. Obviously, this is a very subjective approach and results should therefore be treated with caution. However, the cells operated at 0.5 A/cm^2 and 1.5 A/cm^2 show almost identical behavior for each investigated temperature as displayed in Fig. 42. Considering only those, an increase in resistance of $5.8 \text{ m}\Omega\cdot\text{cm}^{-2}$, $15.2 \text{ m}\Omega\cdot\text{cm}^{-2}$ and $15.3 \text{ m}\Omega\cdot\text{cm}^{-2}$ occurs at $750 \text{ }^\circ\text{C}$, $800 \text{ }^\circ\text{C}$ and $850 \text{ }^\circ\text{C}$, respectively.

Both ways of interpreting the data results in the finding that there is only little degradation at $750 \text{ }^\circ\text{C}$ and significantly more at $800 \text{ }^\circ\text{C}$. A further increase in temperature to $850 \text{ }^\circ\text{C}$ has hardly any additional effect on degradation rate.

Fig. 43 presents the influence of the hydrogen gas humidity on the degradation of the oxygen electrode. As expected there appears to be no correlation and average degradation rate is similar for all three humidities, while scattering likely accounts for any minor deviations.

It is noteworthy that under certain operating conditions the degradation of the oxygen electrode largely contributes to the overall degradation. For example at 850 °C and 0.5 A/cm² it amounts approximately 40 % of the overall degradation, however, especially at 750 °C it has hardly any impact.

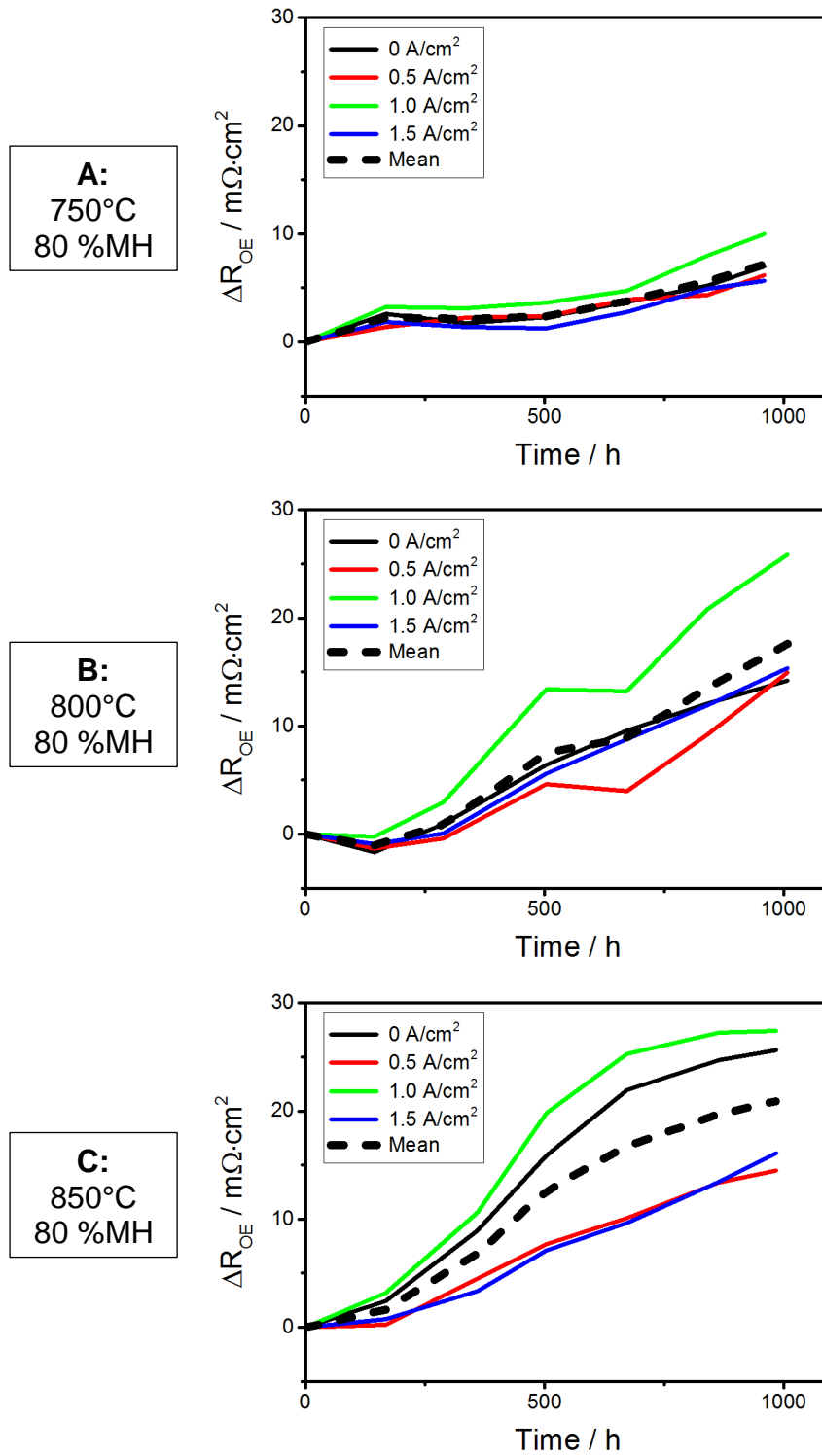


Fig. 42: Influence of operating temperature on degradation of oxygen electrode process. Cells operated at (A) 750 °C, (B) 800 °C and (C) 850 °C, current densities of OCV, 0.5 A/cm², 1.0 A/cm², 1.5 A/cm² at each respective temperature and 80 %MH.

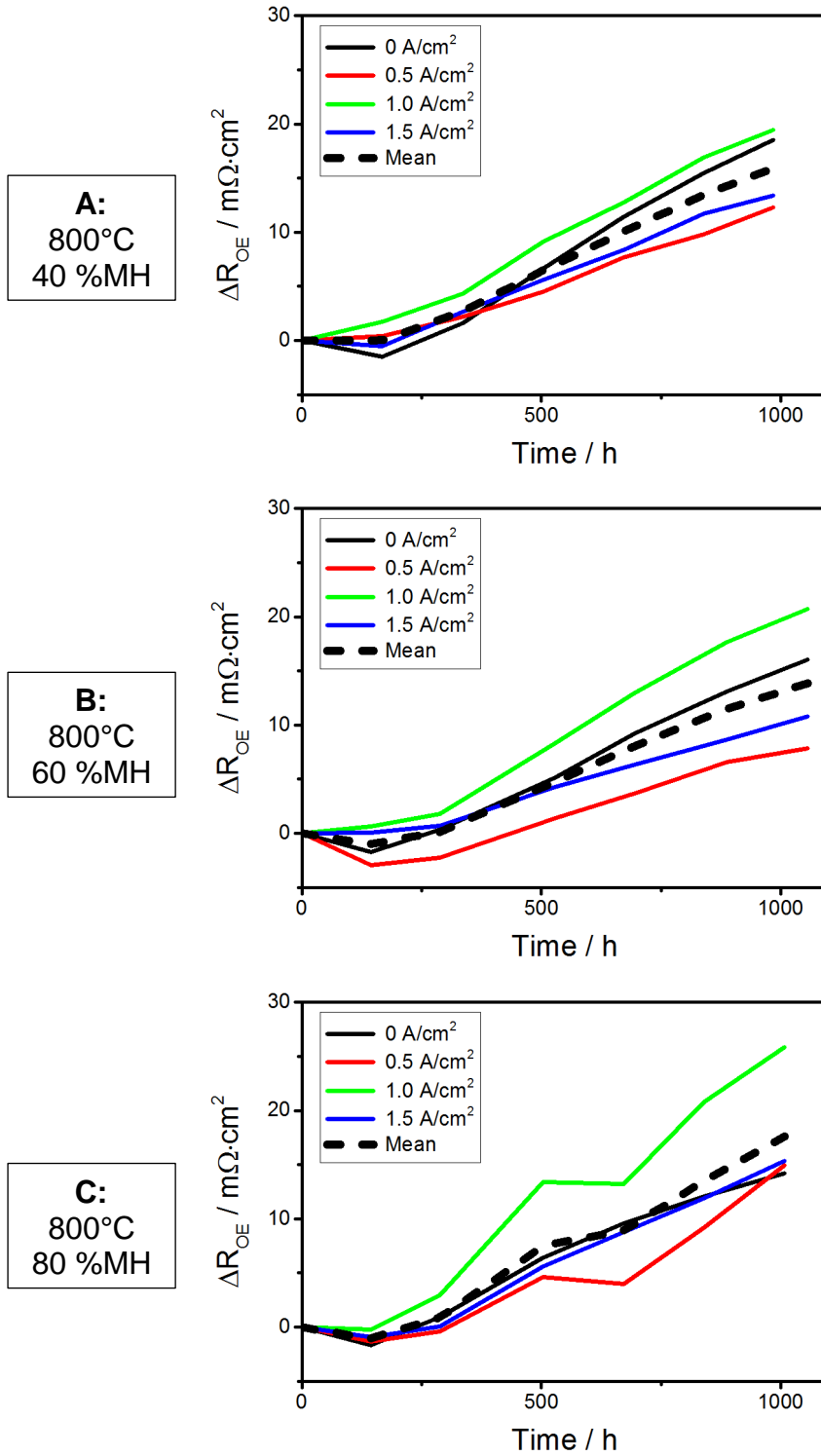


Fig. 43: Influence of operating temperature on degradation of oxygen electrode process. Cells operated at (A) 40 %MH, (B) 60 %MH and (C) 80 %MH, current densities of OCV, 0.5 A/cm², 1.0 A/cm², 1.5 A/cm² at each respective humidity and 800 °C.

5.2.2 Post-test results

After operation each cells' oxygen electrode was analyzed for microstructural alteration but no changes could be detected. Additionally, BSE-SEM analysis was conducted and signs of compositional inhomogeneities were detected as demonstrated by different levels in back scattering intensities. These were found in all operated samples as well as the reference sample. The fact that no qualitative difference between the reference sample (Fig. 44A) and an operated sample exhibiting significant degradation (Fig. 44B, cell operated at 800 °C, 80 %MH and 1.0 A/cm²) can be observed suggest that the observed compositional inhomogeneities are production related and do not originate from sample operation.

Furthermore, the chemical composition of the oxygen electrode was analyzed using REM-EDS. For sampling the region close to the CGO layer with an approximate distance of 5 – 10 μm was chosen. The LSCF-cation concentrations of operated cells in comparison with the reference sample are shown in Fig. 45. For neither of the respective elements a considerable change relative to the reference sample can be detected. Results might indicate a minor loss of Sr on A-site in all cells during operation. However, no correlation with temperature or current density is detectable. On B-site also no distinct changes were found, while Co does show a somewhat higher variance. This could be explained by the significantly lower signal intensity of Co and hence stronger scattering. Furthermore, the oxygen electrodes of all operated cell revealed traces of Pt. Its presence can be attributed to the use of Pt-meshes for oxygen electrode contacting. It should be noted that results deviate from the expected LSCF-6428 composition. This can be explained by the porous nature of the sample influencing EDS analysis as well as a lack of specific calibration for the investigated elements. Observed changes relative to the reference cell are unaffected by this and retain validity.

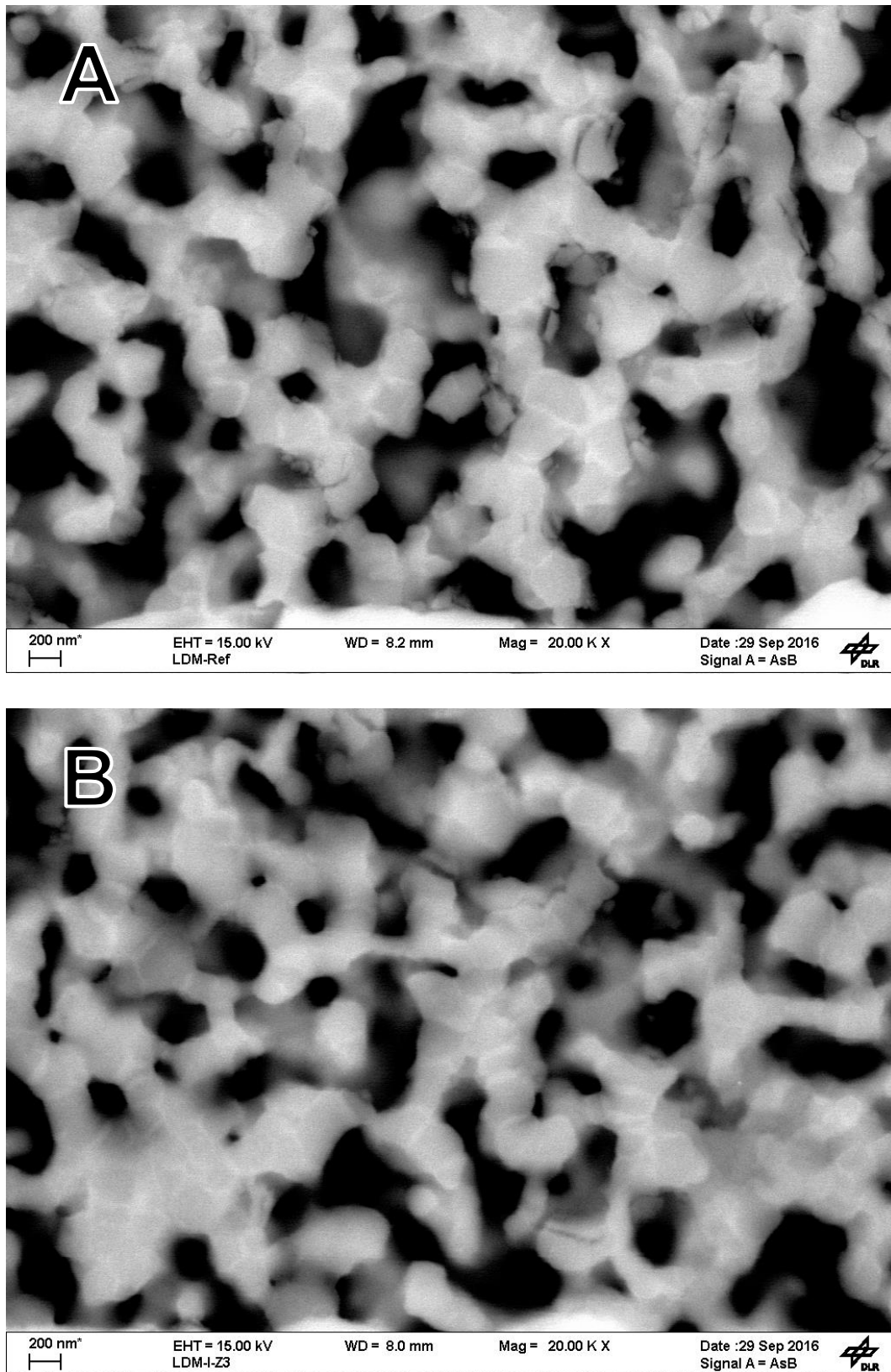


Fig. 44: BSE-SEM images of the oxygen electrode of (A) reference sample and (B) the cell operated at 800 °C, 80 %MH and 1.0 A/cm² for 1000 h

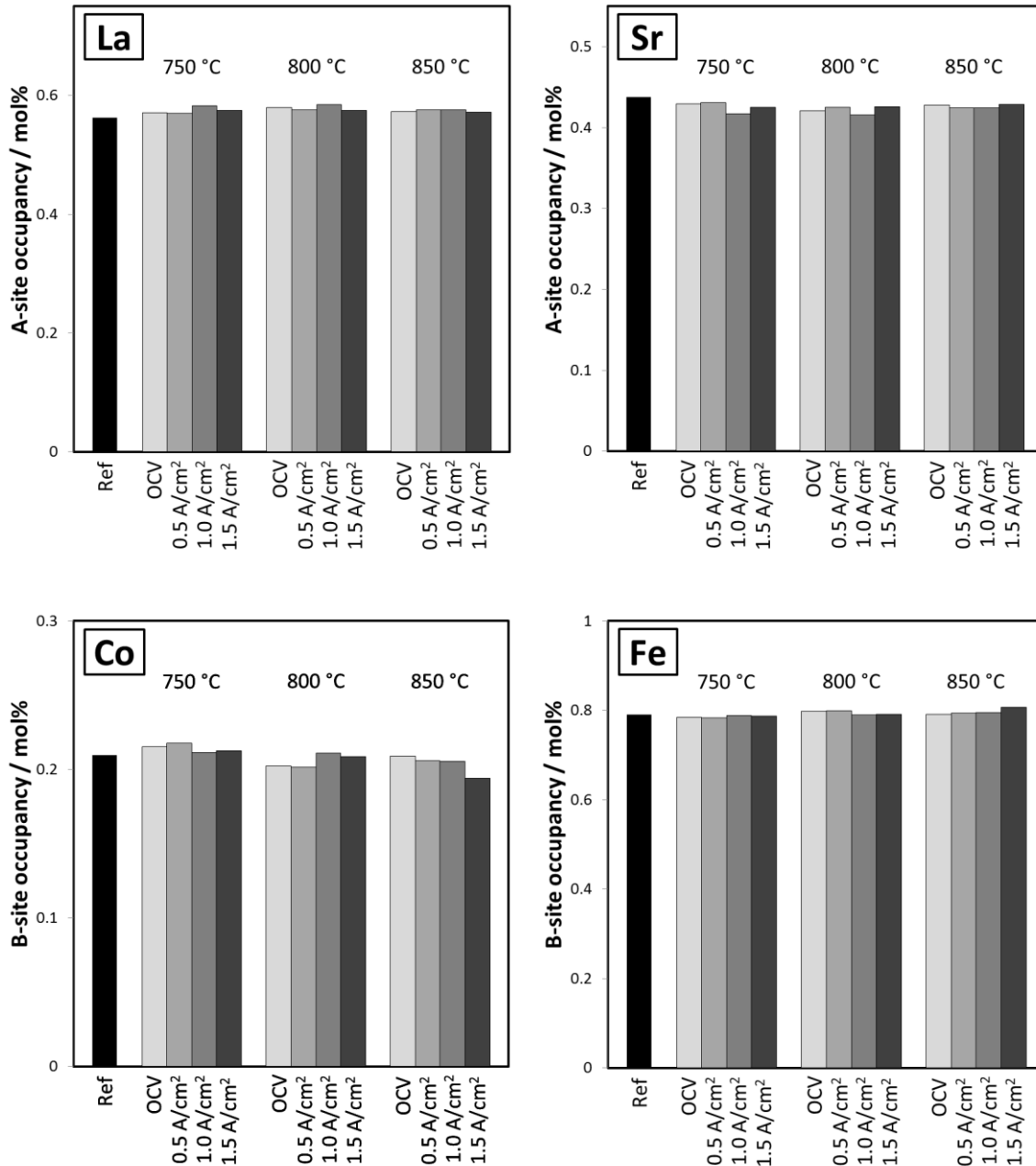


Fig. 45: Average A- and B-site composition of LSCF layer in vicinity of electrolyte measured by REM-EDS analysis of cells operated at combinations of temperature (750 °C, 800 °C and 850 °C) and current densities (OCV, 0.5 A/cm², 1.0 A/cm², 1.5 A/cm²). All cells were operated at 80 %MH.

Additionally, to the general chemical composition the LSCF layer was also investigated with a surface sensitive method using XPS analysis. Measurements were conducted on top of the LSCF layer, i.e. where the LSCF layer was contacted. The analysis was conducted on the reference sample as well as on samples operated at 800 °C and 80 %MH and a current density of OCV and 1.5 A/cm², respectively. Fig. 46 compares

the depth profile of the three samples, which was obtained by Ar⁺-sputtering. Since the sputtering system was not calibrated for the investigated material no precise sputtering depth can be specified. However, known sputtering rates of comparable materials suggest a sputtering depth of approximately 10 nm after 100 s.

On the very surface both sample as well as the reference show increased Sr occupancy on A-site accompanied by a decreased La content. This trend is more pronounced for the reference cell, while both operated cells show virtually identical characteristics. Concerning B-site both operated samples show a slightly increased Fe and decreased Co occupancy towards the surface. The reference sample exhibits the same trend but to a hardly noticeable degree. This shows that current density has no influence on LSCF surface composition. Analogous to the EDS measurements the equipment was not calibrated for the investigated elements, accounting for possible variations from expected composition.

Apart from the LSCF ions traces of Pt were found as well, which in all likelihood originate from the contacting meshes as mentioned earlier. Furthermore, large amounts of carbon were detected on all three probes. These were highest with approximately 43 mol% on the surface of the reference sample and with 29 mol% and 24 mol% lower for the sample operated at 1.5 A/cm² and OCV, respectively. After sputtering for 100 s the carbon concentration was still between 5 mol% and 10 mol% for all three samples. The fact that the largest concentration of carbon was found on the reference sample suggests the source to be production related, while the nature of the carbon species and its effect on the electrode's activity remain unknown.

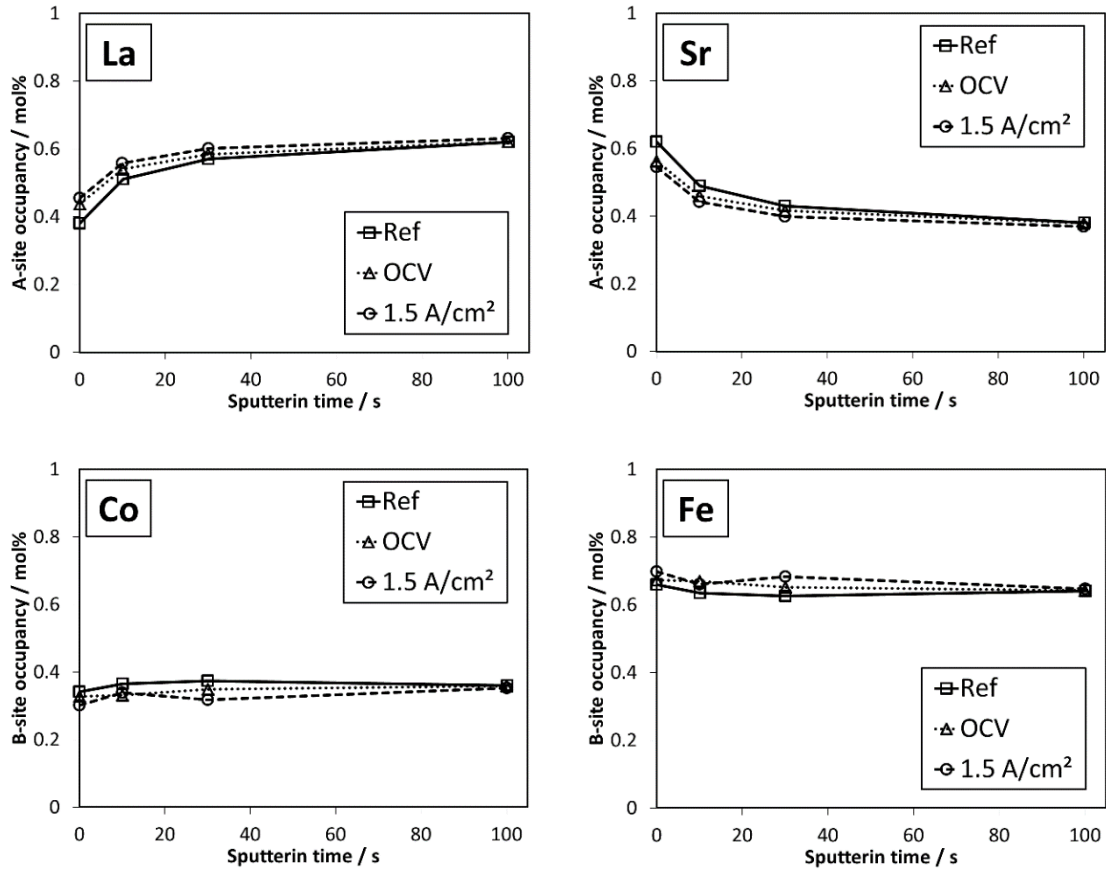


Fig. 46: XPS analysis of LSCF cation concentration on surface of LSCF structure. The measurements were conducted on the LSCF surface previously in touch with the contacting mesh. Beside the reference, two cells operated at 800 °C, 80 %MH and a current of OCV and 1.5 A/cm², respectively were investigated. (Compare Fig. 42B for respective in-situ results)

Apart from analysis of the oxygen electrode concerning general and surface chemical composition, XRD measurements were conducted to examine crystallographic structure. Fig. 47 compares the XRD spectra of cells operated at 750 °C, 800 °C and 850 °C and different current densities. All cells operated at 750 °C show very similar spectra relative to the reference sample and no distinctive difference can be observed. At 800 °C all operated cells show the formation of new peaks alongside the peaks of the reference structure at slightly lower diffraction angles, indicating the formation of a secondary phase. The same can be observed for all cells operated at 850 °C, where new peaks are formed in correspondence to the original peaks but at slightly lower diffraction angles.

The crystallographic nature of these phases is not easily determined. Several detailed XRD studies suggest rhombohedral system for $L_{0.6}S_{0.4}C_{0.2}F_{0.8}O_{3-\delta}$ operated under the applied conditions [128–132]. There is, however, a phase transition from rhombohedral to cubic above certain temperatures. For $L_{0.6}S_{0.4}C_{0.8}F_{0.2}O_{3-\delta}$ this was found to be at ap-

proximately 500 °C, while the authors state an increase of transition temperature for a perovskite with increasing Fe content on B-site [133–135]. The gathered XRD data is not suitable to unambiguously identify the crystallographic nature of the LSCF phases, where both cubic and rhombohedral structures are possible while both phases could coexist as well.

In order to compensate for this uncertainty, determination of crystallographic parameters of the reference sample was conducted for both cubic and rhombohedral structure. Fig. 48 shows how they can be used very similarly to describe the spectrum of the reference cell while the residuals confirm similar fit quality. The rhombohedral crystal parameters were transformed into the pseudo-cubic lattice parameter $a_{pseudo-Cubic}$ from its crystal volume $V_{Rhombohedral(ABO_3)}$ according to the following formulas:

$$a_{pseudo-Cubic} = \sqrt[3]{V_{ABO_3}} \quad (5.8)$$

$$V_{Rhombohedral(ABO_3)} = \frac{a^3 \cdot \sqrt{1 - 3\cos^2\alpha + 2\cos^3\alpha}}{2} \quad (5.9)$$

with α and a representing the cell angle and lattice parameter of the rhombohedral structure, respectively. This is a commonly used approach to provide comparability between different crystallographic systems [128, 129, 133]. The pseudo-cubic lattice parameters of the rhombohedral structure are in good agreement with the cubic lattice parameters as listed in Table 7.

Since the results are very similar for both crystallographic systems, the cubic structure was chosen for the analysis of degraded samples. In order to account for the additional peaks found in samples operated at 800 °C and 850 °C a secondary cubic phase was assumed for fitting. Samples operated at 750 °C were fitted assuming only one cubic phase as no secondary peaks are detectable. An exemplary fit is shown in shown in Fig. 49 for the cell operated at 800 °C and OCV, while the corresponding residuals reveal a good representation. The lattice parameters for both phases of each degraded cell are listed in Table 7.

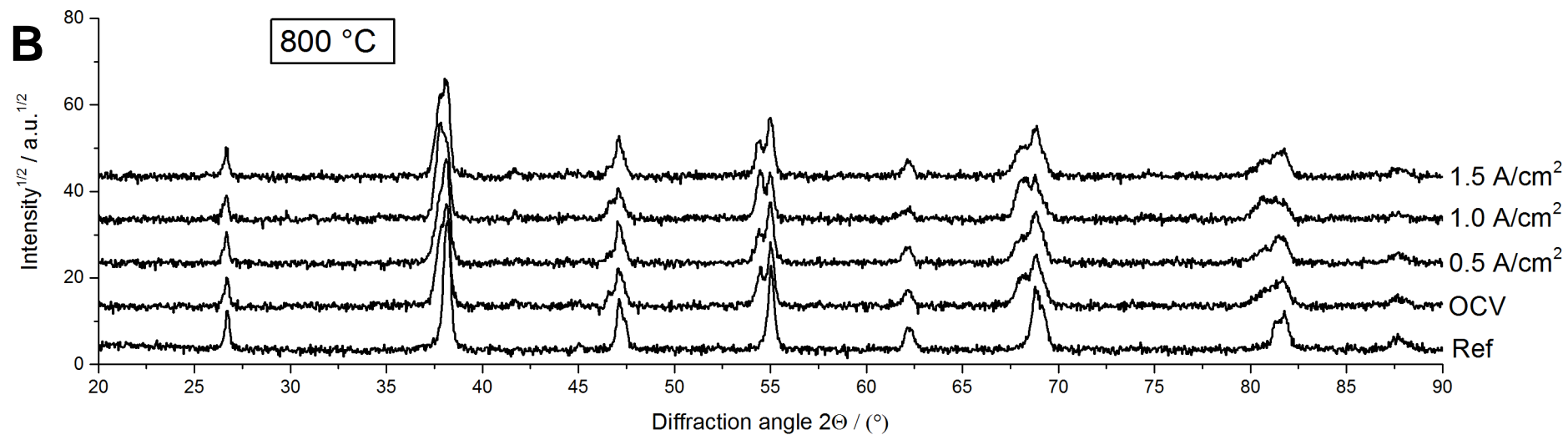
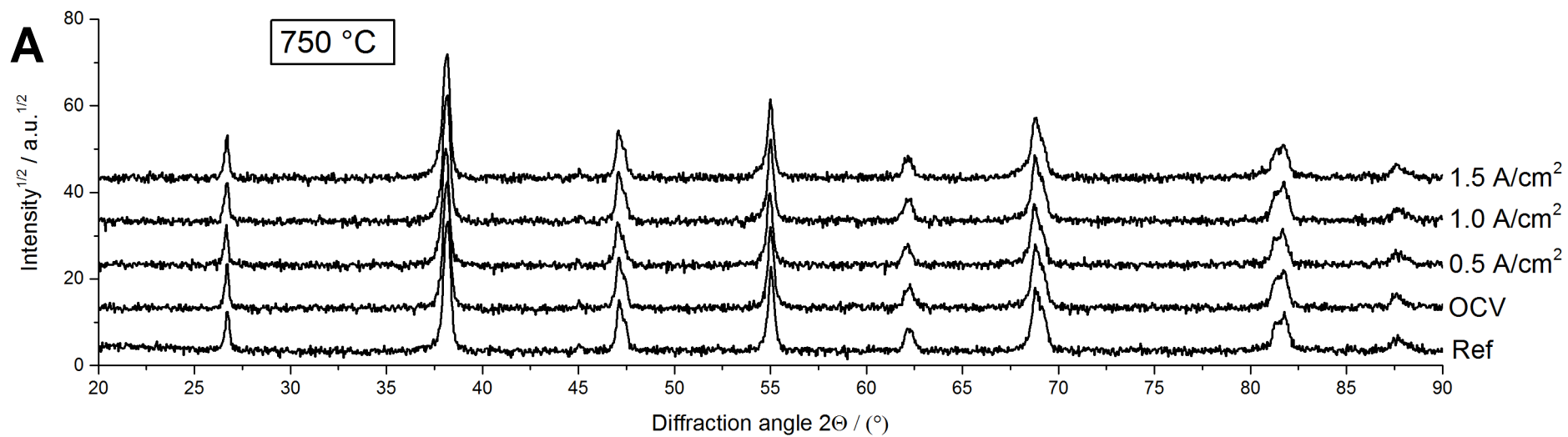
The analysis indicates a minor increase in lattice parameter of the original phase for all cells during operation, while no distinct trend with temperature or current density can be found. The increase in lattice parameter averages at approximately 0.003 Å for all degraded cells while their standard deviation amounts roughly 0.0015 Å.

The new phase which is found in samples degraded at 800 °C and 850 °C differs from the original phase by approximately 0.035 Å and no clear trend between lattice size and current density or temperature can be detected. Also the fraction of the secondary phase is similar in average for cells operated at 800 °C and 850 °C. However, strong variation between individual cells can be observed.

| | Primary phase | | Secondary phase | | Fraction | |
|---------------------------------|---------------|----------------|-----------------|----------------|---------------|-----------------|
| | <i>a</i> | V | <i>a</i> | V | primary phase | secondary phase |
| Unit | Å | Å ³ | Å | Å ³ | % | % |
| Ref - rhombohedral ^a | 3.8728 | 58.060 | - | - | 100 | - |
| Ref - cubic | 3.8722 | 58.084 | - | - | 100 | - |
| 750 °C - OCV | 3.8739 | 58.138 | - | - | 100 | - |
| 750 °C - 0.5 A/cm ² | 3.8780 | 58.321 | - | - | 100 | - |
| 750 °C - 1.0 A/cm ² | 3.8744 | 58.157 | - | - | 100 | - |
| 750 °C - 1.5 A/cm ² | 3.8752 | 58.196 | - | - | 100 | - |
| 800 °C - OCV | 3.8737 | 58.128 | 3.9091 | 59.737 | 64 | 36 |
| 800 °C - 0.5 A/cm ² | 3.8755 | 58.209 | 3.9102 | 59.785 | 67 | 33 |
| 800 °C - 1.0 A/cm ² | 3.8758 | 58.223 | 3.9099 | 59.774 | 46 | 54 |
| 800 °C - 1.5 A/cm ² | 3.8754 | 58.204 | 3.9117 | 59.856 | 60 | 40 |
| 850 °C - OCV | 3.8748 | 58.178 | 3.9050 | 59.549 | 59 | 41 |
| 850 °C - 0.5 A/cm ² | 3.8724 | 58.068 | 3.8990 | 59.271 | 75 | 25 |
| 850 °C - 1.0 A/cm ² | 3.8777 | 58.307 | 3.9081 | 59.689 | 51 | 49 |
| 850 °C - 1.5 A/cm ² | 3.8765 | 58.253 | 3.9065 | 59.618 | 71 | 29 |

^a Pseudo cubic lattice constant as cube root of ABO₃ cell volume

Table 7: Crystallographic lattice parameters of oxygen electrode's phases of reference sample as well as operated cells.



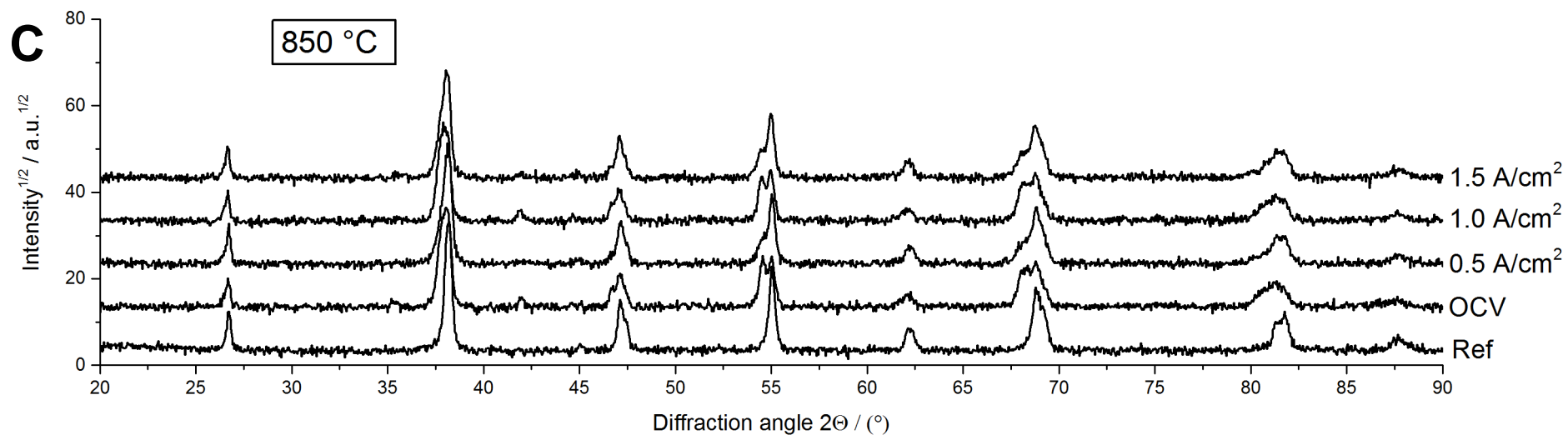


Fig. 47: XRD spectra of LSCF layer of cells operated at (A) 750 °C, (B) 800 °C and (C) 850 °C and different current densities of OCV, 0.5 A/cm², 1.0 A/cm² and 1.5 A/cm² respectively, in comparison with a reference sample. Cells operated at 750 °C show no significant changes. Cells operated at 800 °C and 850 °C show the formation of additional peaks at slightly lower angles relative to the peaks of the reference sample, suggesting the formation of a secondary phase.

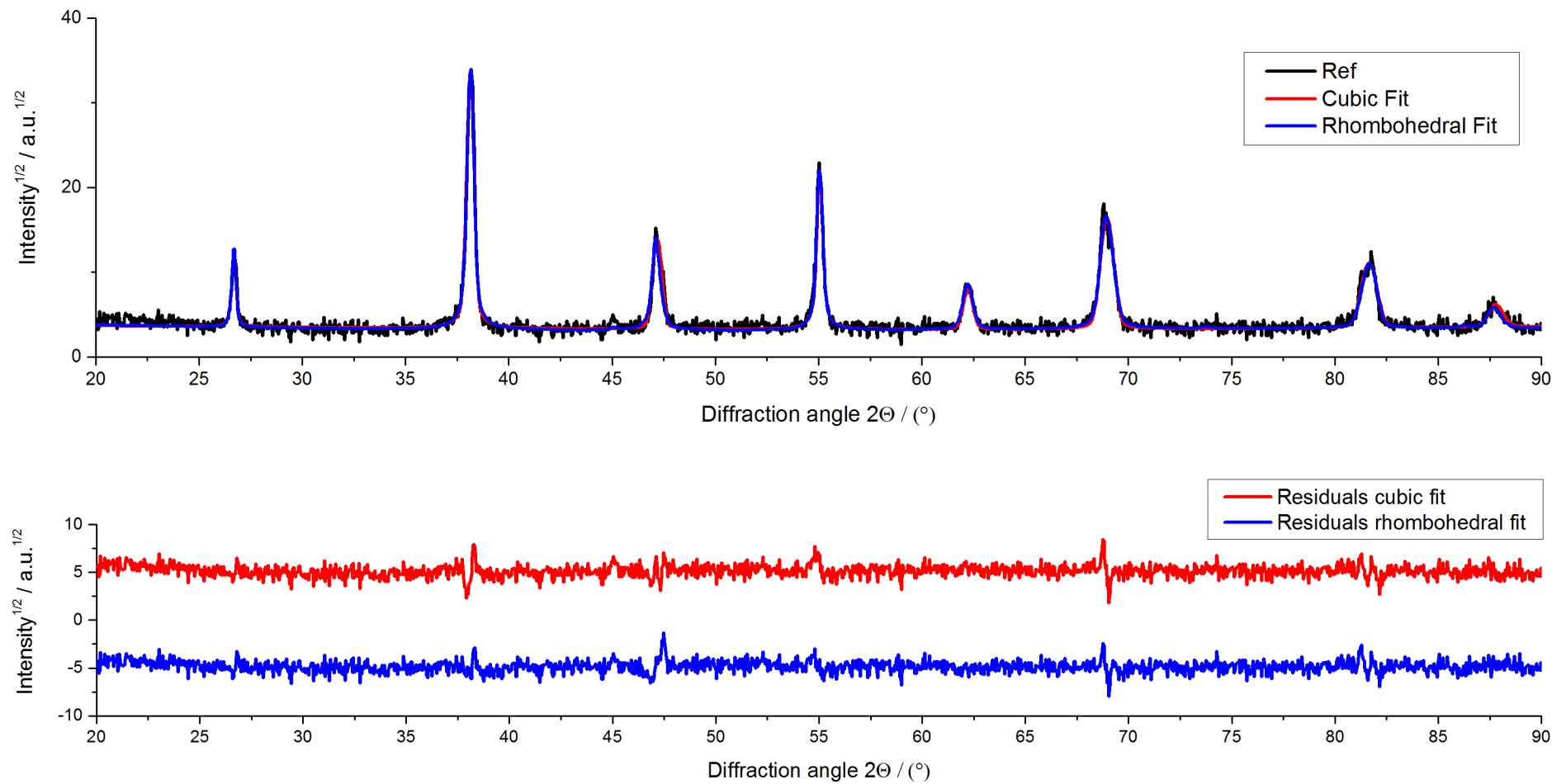


Fig. 48: Recorded XRD spectrum of reference sample with fits (top) and corresponding residuals (bottom). The reference spectrum was fitted assuming cubic ($Pm\bar{3}m$) or rhombohedral ($R\bar{3}c:R$) structure.

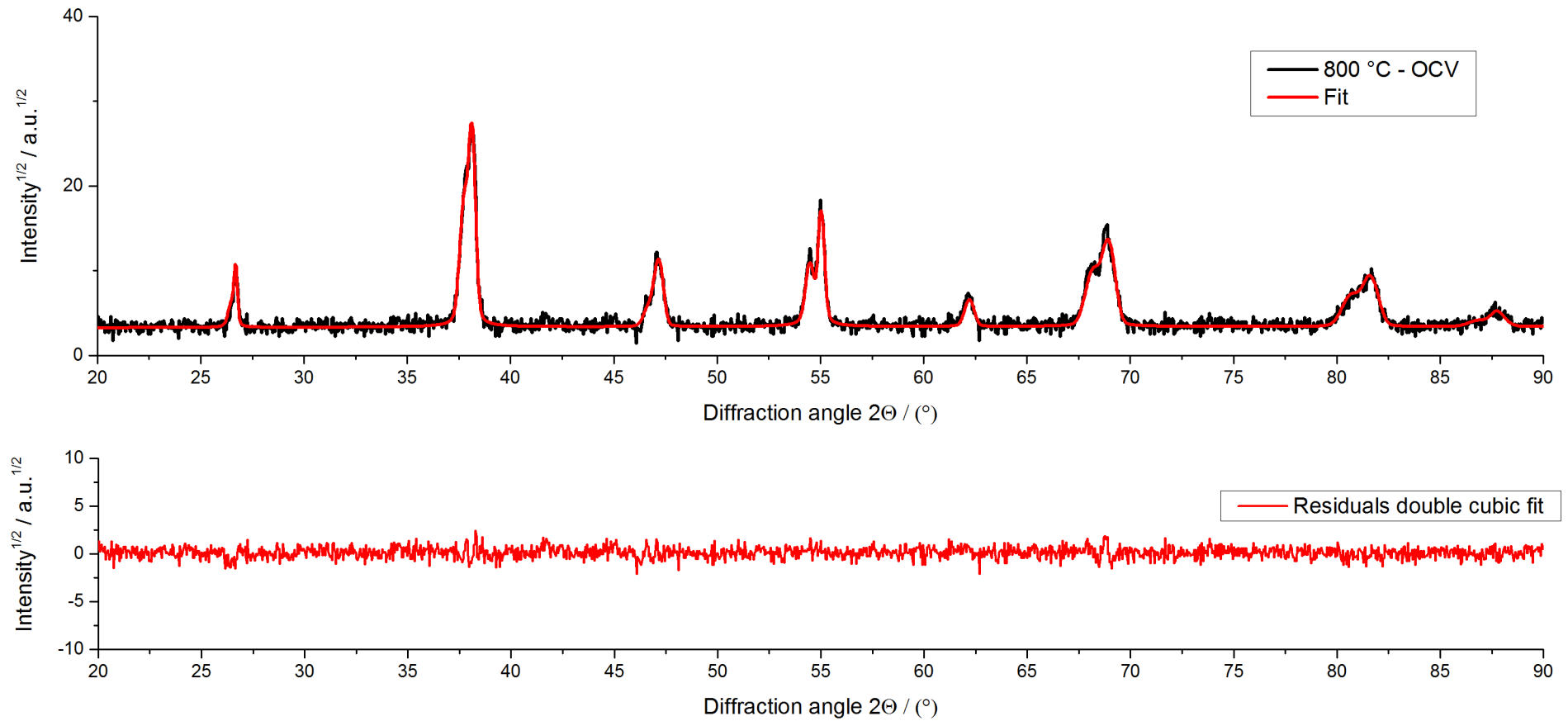


Fig. 49: Recorded XRD spectrum of cell operated at OCV and 800°C with fit assuming two cubic ($Pm\bar{3}m$) structures (top) and corresponding residuals (bottom).

5.2.3 Discussion

Both SEM-EDS and XPS analyses do not reveal any changes occurring during operation which could be correlated with in-situ degradation. XPS analysis of Sr is of special interest, since Sr segregating at the LSCF's surface is an often reported degradation mechanism for SOFC operation [46, 47, 136]. However, comparison of surface composition between reference and operated cells (compare Fig. 46) clearly shows that this is not the case for the cells investigated in this dissertation. While the operated cells do show an increasing Sr content towards the surface, this gradient is even more pronounced in the reference sample. A few nanometers inside the LSCF structure the Sr content is equal in operated and reference samples. This shows that there is Sr enrichment at the surface – likely evolving during sintering – which decreases during operation. However, no Sr segregates form as a result of cell operation. Furthermore, no difference in surface composition between the cell operated at OCV and 1.5 A/cm^2 can be detected, while polarization is reported to play an important role on the formation of Sr segregation. [47]

A distinct conformity between in-situ degradation and post-test measurements can be found in that an increase in polarization resistance is accompanied by changes in crystallographic structure. Both describe the same general behavior with temperature. At $750 \text{ }^\circ\text{C}$ there is only very limited electrochemical degradation and the XRD spectra reveal no obvious alteration. At $800 \text{ }^\circ\text{C}$ and $850 \text{ }^\circ\text{C}$, where a significant increase in resistance is observed, XRD analysis reveals the formation of a new crystalline phase. Furthermore, for neither in-situ nor XRD measurements a trend with current density can be observed. In addition, an analogy for each individual cell was observed between the quantity of the new phase formed during operation (compare Table 7) and the increase in polarization resistance. For example at $850 \text{ }^\circ\text{C}$ (Fig. 42C) the cell operated at 1.0 A/cm^2 experienced the strongest degradation closely followed by the cell operated at OCV. These cells also show the highest quantity of secondary phase with 49 % and 41 %, respectively. The cells operated at 1.5 A/cm^2 and 0.5 A/cm^2 both show significantly lower degradation with a slightly higher rate at 1.5 A/cm^2 . This is as well in excellent agreement with the 29 % and 21 % of the new phase, respectively. The very analog behavior of in-situ degradation and changes in XRD characteristics strongly suggests a correlation between the two.

There are previous studies which observed similar change in XRD spectra of LSCF after operation. However, so far no convincing interpretation has been offered. A study reported a phase change from rhombohedral to cubic after 100 h of operation at 800 °C [137]. The observed increase in electrode polarization resistance was attributed to this phase change. However, no explanation for this statement was offered. Another study reporting on a stack operated for 9000 h in electrolysis mode revealed a broadening of XRD reflections towards smaller diffraction angles, which was attributed to compositional changes within the LSCF structure as observed by BSE-SEM imaging [41]. Unfortunately, no such measurement of the initial state was offered for comparison. This is of importance since in this thesis compositional inhomogeneities were detected in the operated samples as well as in the reference sample (compare Fig. 35), while no significant change due to operation was found. At the same time XRD analyses clearly do show a change in crystallographic structure after operation at certain conditions. Furthermore, operation does not lead to a broadening of peaks as observed in the previously mentioned study but the formation of a distinct secondary crystalline phase. Consequently, the partially de-homogenized state of the LSCF recorded by BSE-SEM imaging cannot explain the change in crystallographic structure observed during operation. Based on these studies from literature the underlying mechanism of the change in LSCF crystallographic structure detected in this work remains unclear.

One possible scenario to explain the experimental findings is the formation of grains with different chemical composition. In order to check the plausibility of this scenario the change in chemical composition necessary to achieve the observed shift in lattice parameter will be estimated in the following. The lattice parameter a can be calculated according to

$$a = \sqrt{2} \cdot (r_A + r_O) \quad (5.10)$$

with r_A , and r_O for the ionic radius of A-site cations and oxygen-ions, respectively, under the precondition that the Goldschmidt tolerance factor t_{Gold} [138] is close to one. This is calculated by

$$t_{Goldschmidt} = \frac{r_A + r_O}{\sqrt{2} \cdot (r_B + r_O)} \quad (5.11)$$

with r_B for the ionic radius of B-site cations.

While the A-site cations have distinct properties determination of the B-site ionic radius is somewhat more difficult. On the one hand the ions can exhibit different oxidation states and there are theoretical studies providing approximate values. [44] On the other hand Fe^{3+} and Co^{3+} can exist in low spin and high spin configuration. In order to encompass these uncertainties a maximum and minimum value for t_{Gold} is calculated, which equals 1.016 and 0.979, respectively. Both extremes are sufficiently close to one, which means that the preconditions for equation (5.10) are satisfied.

Consequently, the change in A-site ionic radius Δr_A which corresponds to an increase in lattice parameter Δa of 0.035 Å (difference between lattice parameter of secondary and original phase, compare Table 7) can be calculated pursuing equation (5.10):

$$\Delta r_A = \frac{\Delta a}{\sqrt{2}} = 0.0247 \text{ \AA} \quad (5.12)$$

Accordingly, the corresponding change in A-site Sr occupancy $n_{A_{\text{Sr}}}$ is

$$\Delta n_{A_{\text{Sr}}} = \frac{\Delta r_A - r_{\text{Sr}^{2+}}}{r_{\text{La}^{3+}} - r_{\text{Sr}^{2+}}} = 0.31 \quad (5.13)$$

This means that the XRD reflections of the secondary phase could be explained by a new phase with an A-site occupancy of 0.29 for La^{3+} and 0.71 for Sr^{2+} . This is a result within a physically meaningful range which could explain the observed change. Experimental findings by Tai et al. [129] suggest an even further change in occupancy of approximately 0.5. There are, however, difficulties concerning this theory. If indeed a change in chemical composition is occurring, one would expect a gradual change which would lead to a phase broadening. Instead in the present study the formation of well-defined peaks was observed, which means only one discrete phase would be forming. Furthermore, if one Sr-enriched phase is forming the remaining phase has to be Sr depleted, since no large scale change in chemical composition was observed. This remaining phase would consequently experience a change in lattice parameter as well, which was also not observed.

This estimation calculation is not meant to prove or rebuff the described theory but verify its theoretical viability. It shows that the chemical composition necessary to match the observed secondary XRD reflections is in a reasonable range, while also revealing issues such as the unchanged XRD reflections of the original phase and the presence of a discrete secondary phase. The complex nature of perovskites opens up a series of possibilities, like oxygen deficiencies or understoichiometric site occupancy to

explain remaining inconsistencies. The ionic radii used for this calculation are listed in Table 8.

| | Ionic radii [Å] | Relative occupancy | Average ionic radius [Å] |
|-------------------------|-----------------|--------------------|--------------------------|
| A-site | | | 1.392 |
| La ³⁺ | 1.36 | 0.6 | |
| Sr ²⁺ | 1.44 | 0.4 | |
| B-site - minimum | | | 0.5437 |
| Fe ³⁺ | 0.55 | 0.64 | |
| Fe ⁴⁺ | 0.585 | 0.16 | |
| Co ³⁺ | 0.545 | 0.18 | |
| Co ⁴⁺ | 0.53 | 0.02 | |
| B-site - maximum | | | 0.6162 |
| Fe ³⁺ | 0.645 | 0.64 | |
| Fe ⁴⁺ | 0.585 | 0.16 | |
| Co ³⁺ | 0.61 | 0.18 | |
| Co ⁴⁺ | 0.53 | 0.02 | |
| Anion | | | 1.4 |
| O ²⁻ | 1.4 | 1 | |

Table 8: List of ionic radii of LSCF ions according to [139]

Another scenario to explain the observed changes is the occurrence of a phase change possibly from rhombohedral to cubic. On the one hand this could occur without a change in chemical composition, which would be in agreement with several experimental findings. For this case no change to the crystallographic properties of the original phase and no overall changes to chemical composition are expected. Furthermore, in this case a stronger phase transition is expected for higher temperatures [133], which matches well with the low degradation observed at 750 °C but does not explain the small difference between 800 C and 850 °C.

A third scenario could be a deficiency driven phase change. It is well known that Sr deficient $\text{La}_x\text{Sr}_{(1-x)}\text{ZCo}_y\text{Fe}_{1-y}\text{O}_{3-\delta}$ shows stable perovskite structure even for large Sr deficiencies Z [128, 131, 132, 140, 141]. With increasing deficiency the phase is shifted towards cubic system [131, 132]. However, the deficiency values investigated in these studies are with 50 % and higher significantly larger than the very limited Sr loss observed after operation. Furthermore, the Sr deficient cubic phase was reported to have significantly better electrochemical performance compared to stoichiometric rhombohedral phase [132], so that this deficiency driven phase change can neither explains the

observed performance degradation nor does it coincide with the analyses of chemical composition.

The data of this study reveal a strong correlation between performance degradation and crystallographic changes. However, none of the presented scenarios can unambiguously explain the experimental findings and there are questions which remain to be answered. If a phase change is present what is driving it and if it is occurring from cubic to rhombohedral why should it decrease electrochemical performance? Secondly, the temperature dependence remains difficult to explain: Why is there only a small difference between the samples operated at 800 °C and 850 °C, while there is a substantial one between 750 °C and 800 °C? Due to the complex nature of the perovskite material LSCF a consecutive study focusing on LSCF degradation is required to answer these questions.

5.3 Hydrogen electrode resistance

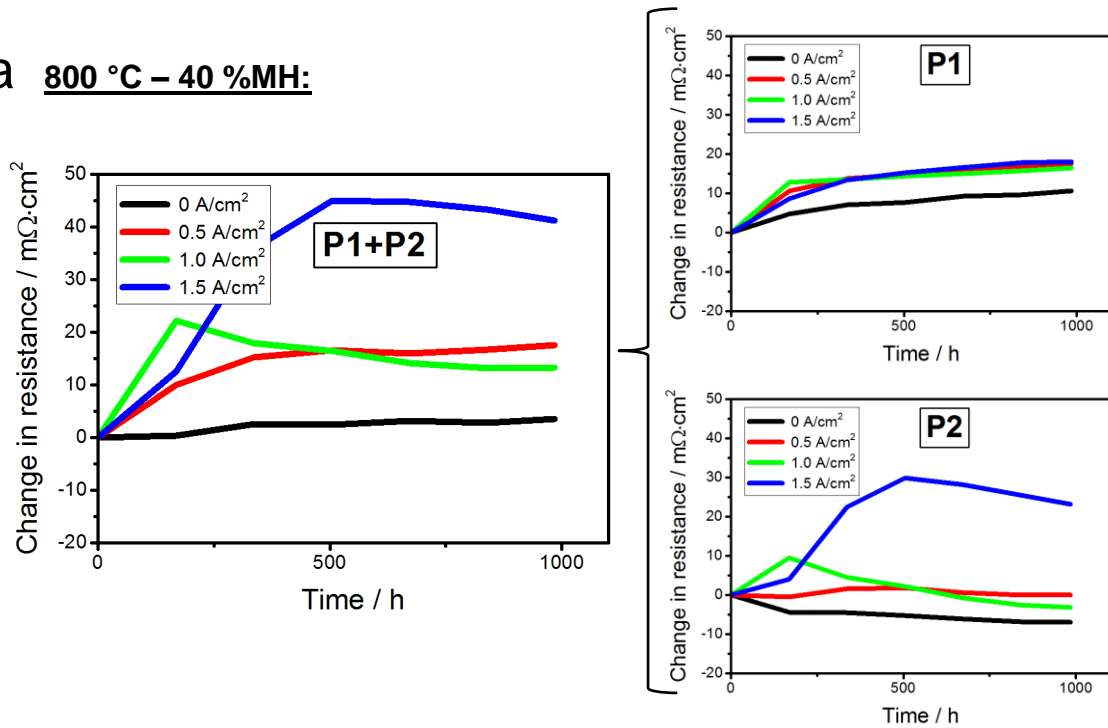
The present section will investigate the effect of operation on the hydrogen electrode charge transfer resistance, that is, the two high-frequency contributions P_1 and P_2 identified in Fig. 14 and described in Table 5. The interpretation of results is complex since both processes P_1 and P_2 are coupled, and as a consequence different degradation processes related to the hydrogen electrode resistance are difficult to distinguish. While the Ni depletion process previously discussed is a hydrogen electrode degradation process, it is reflected by an increase in ohmic resistance and is therefore not presented here. The findings of this section have also been published elsewhere.[91]

5.3.1 In-situ results

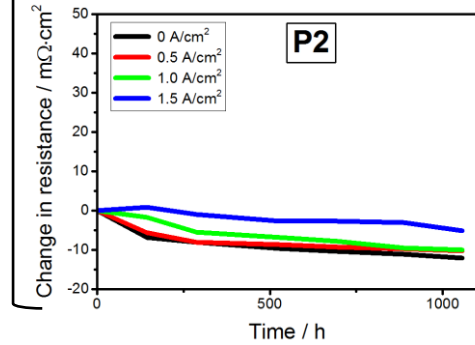
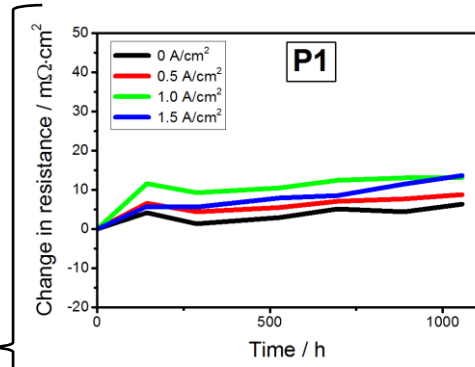
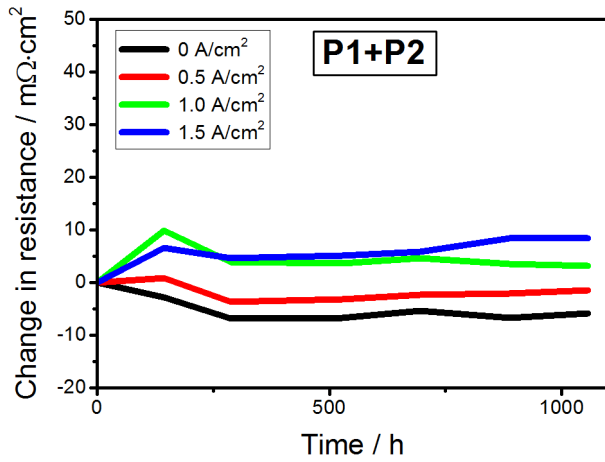
The change in hydrogen electrode polarization resistance of all cells is presented in Fig. 50. Each figure contains the information of the total hydrogen electrode polarization resistance ($P_1 + P_2$), as well as the individual contributions of P_1 and P_2 . The quantitative separation of these two processes is difficult due to their similar characteristic frequencies caused by the increase of the characteristic frequencies of P_2 during operation as will be explained later (compare Fig. 51). Furthermore, it has been demonstrated that the high-frequency hydrogen electrode processes can be modeled with a transmis-

sion line model in a more physically meaningful way than with two R-CPE elements.[82, 142] This can result in an uncertainty regarding the determined resistance values of P_1 and P_2 . However, further quantitative information about the electrode's microstructure is required as input parameters to reduce the number of fitting parameter in a transmission line model. Moreover, the high-frequency hydrogen electrode processes have successfully been modeled with two R-CPE elements before.[143]

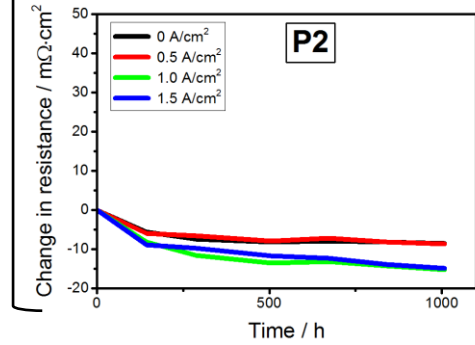
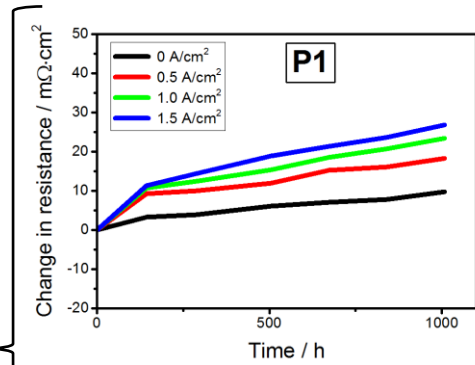
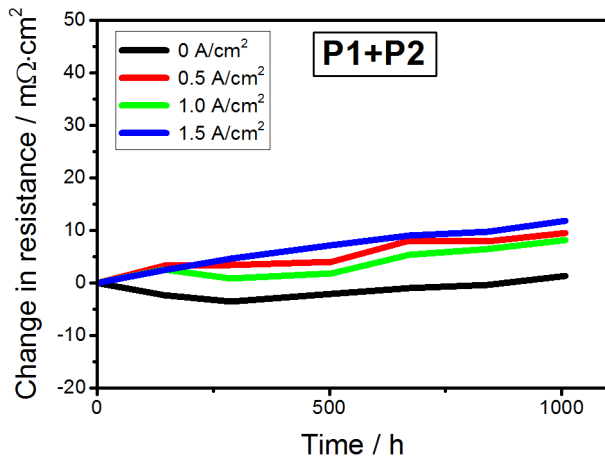
a 800 °C – 40 %MH:



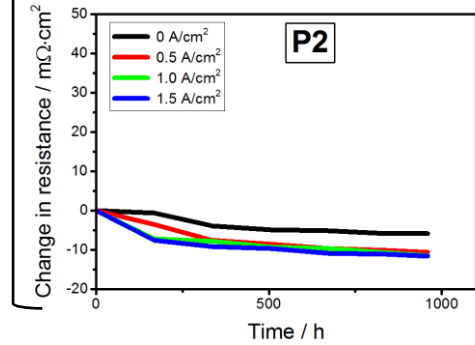
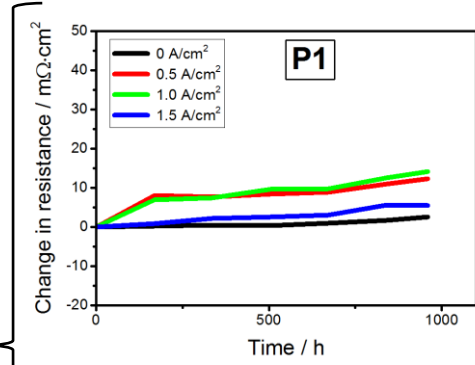
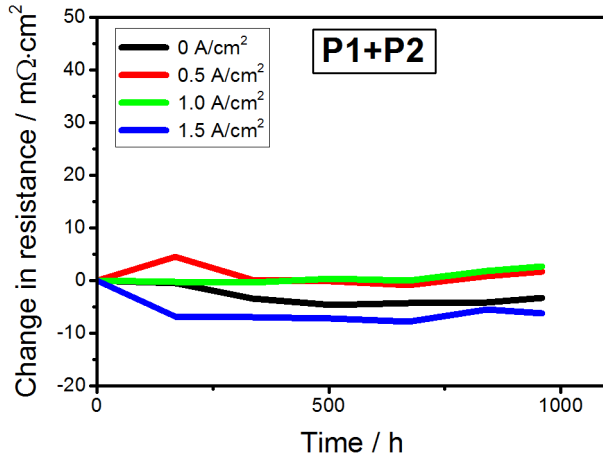
b 800 °C – 60 %MH:



C 800 °C – 80 %MH:



d 750 °C – 80 %MH:



e 850 °C – 80 %MH:

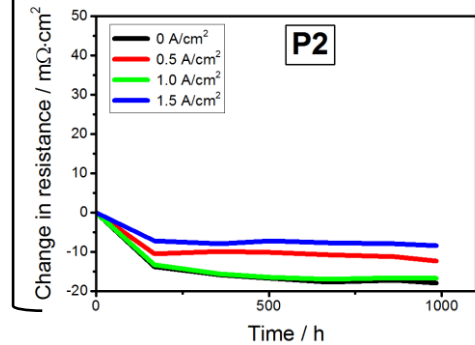
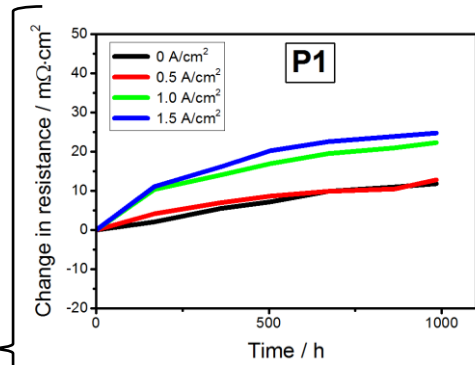
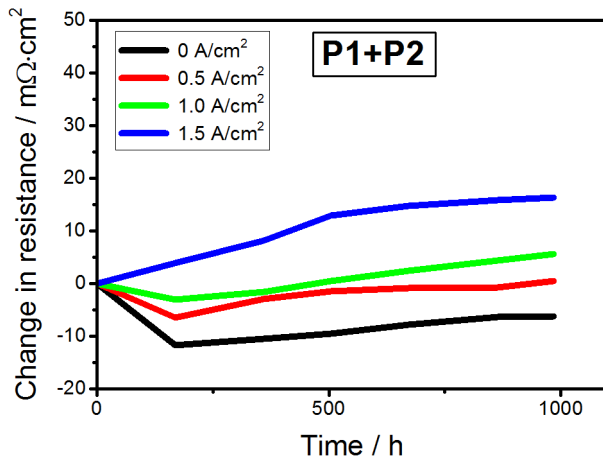


Fig. 50: Change in hydrogen electrode resistance of the cells operated at (a) 800 °C and 40 %MH, (b) 800 °C and 60 %MH, (c) 800 °C and 80 %MH, (d) 750 °C and 80 %MH, and (e) 850 °C and 80 %MH. The graphs show the increase in total hydrogen electrode resistance P1 + P2 in the left panel and the increase of the individual contributions P1 and P2 in the right panel.

For all operating conditions except at 40 % humidity, the resistance increase of the combined hydrogen electrode process P_1+P_2 is significantly lower than the ones of the ohmic resistance depicted in Fig. 25. Furthermore, a general trend observed for almost all cells is an initial decrease of the charge transfer resistance P_2 within the first 150 h followed by a comparatively stable behavior for the remaining operation. This behavior is witnessed at all operating conditions, except for the cells operated at the lowest investigated humidity (40 %MH) and high current densities (1.0 A/cm^2 and 1.5 A/cm^2), indicating that the reaction overvoltage might be a possible driving factor. These cells show an increase of P_2 followed by a decrease.

The initial conditioning of the cells is accompanied by a large shift of the relaxation time especially of the lower frequency hydrogen electrode process towards higher frequencies, which is illustrated in Fig. 51 by the imaginary impedance plots of cells operated at $800 \text{ }^\circ\text{C}$ and 80 %MH. While the two peaks related to the hydrogen electrode process can be distinguished at the initial EIS measurement, they merge into one visible peak after longer testing times. During this conditioning time, the imaginary impedance plots confirm a decrease of the intensity of P_2 and an increase of P_1 in agreement with the obtained fitting values in Fig. 50. This Ni/YSZ electrode conditioning has not been reported in literature so far. Apart from this initial change no clear correlations concerning the influence of operating parameters on P_2 can be identified. Degradation of the hydrogen electrode mainly originates from an increase in P_1 . For most conditions, P_1 tends to increase with current densities. For cells operated at 80 %MH, degradation is larger at $800 \text{ }^\circ\text{C}$ and $850 \text{ }^\circ\text{C}$ compared to $750 \text{ }^\circ\text{C}$, indicating the detrimental effect of temperature on anode microstructure. No obvious trend with humidity change was observed. Thus, in the present study, the hydrogen electrode degradation is dominated by an increase of P_1 , while P_2 barely changes.

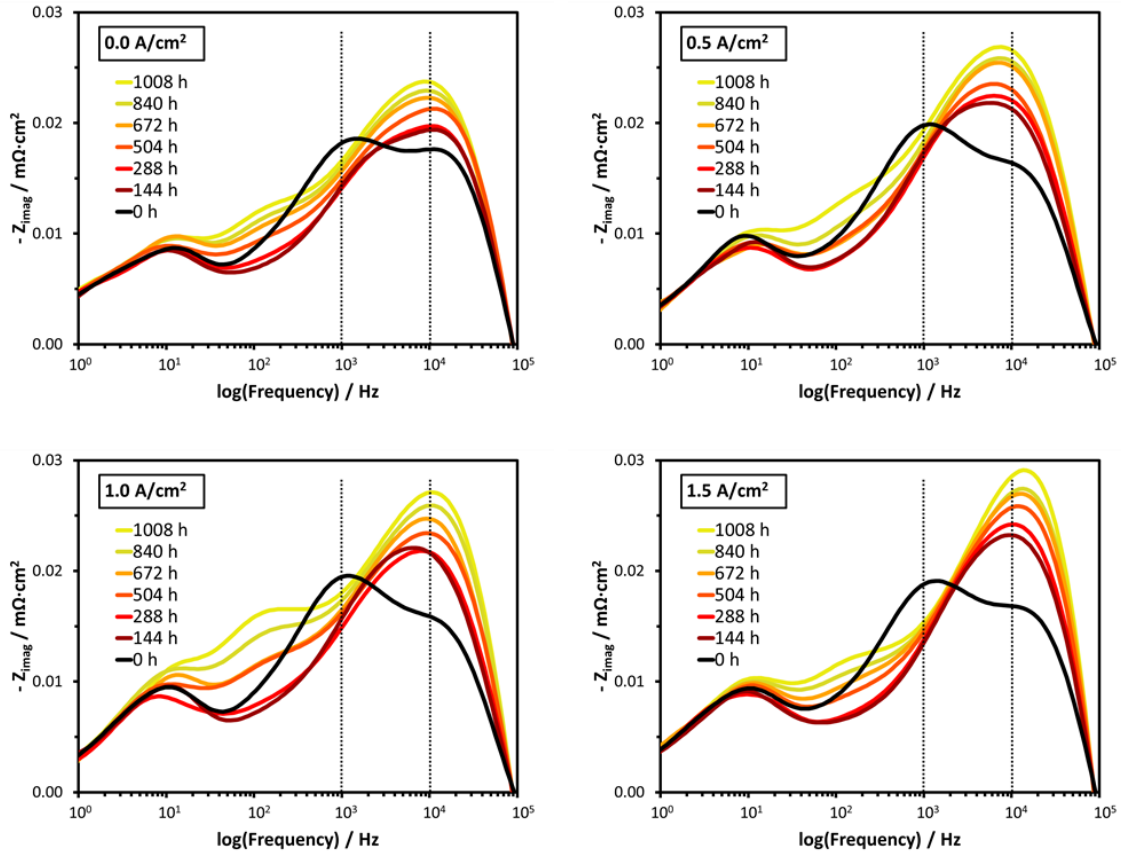


Fig. 51: Bode Plots of cells operated at 800 °C, 80 %MH four different current densities of OCV, 0.5 A/cm², 1.0 A/cm² and 1.5 A/cm², displaying the change of impedance characteristics during 1000 h of operation.

5.3.2 Post mortem results

Operated cells were investigated by SEM imaging coupled with image analysis to gain microstructural insight. This was conducted analog to the characterization of the reference cell's microstructure as described in 4.1. The microstructural characteristics for cells operated at different combinations of temperature and humidity are presented in Table 9. This includes only cells operated at OCV, since phenomena like Ni-depletion occurring under polarization lead to significant changes of (local) electrode characteristics which make it impossible to unambiguously define relevant electrode section for quantification.

The area of the YSZ backbone is similar for all cells, while any deviations originate in all likelihood from statistical inhomogeneity of cell manufacturing. Generally, there appears to be an increased share in Ni phase with increasing activity of volatile Ni spe-

cies, i.e. at high temperatures and humidities, while the pore volume decreases accordingly. Additionally, an increase in characteristic Ni particle size can be observed. It is quantified by the equivalent radius r_{equ} of a spherical particle with same cross-section area to circumference ratio (compare equation (4-1)). At 850 °C and 80 %MH r_{equ} is 18 % larger compared to the reference electrode.

| | $A_{YSZ} / \%$ | $A_{Ni_perc} / \%$ | $A_{Pores} / \%$ | $r_{equ} / \mu\text{m}$ |
|-----------------|----------------|---------------------|------------------|-------------------------|
| Ref | 37.0 | 45.2 | 17.8 | 0.59 |
| 750 °C – 80 %MH | 36.9 | 47.1 | 16.0 | 0.62 |
| 800 °C – 80 %MH | 38.1 | 46.5 | 15.4 | 0.64 |
| 850 °C – 80 %MH | 37.0 | 50.6 | 12.4 | 0.70 |
| 800 °C – 40 %MH | 37.5 | 46.3 | 16.2 | 0.58 |
| 800 °C – 60 %MH | 37.8 | 44.8 | 17.4 | 0.61 |

Table 9: Hydrogen electrodes' microstructural characteristics of cells operated at OCV in comparison to reference cell.

The hydrogen electrodes of all operated cells were furthermore subjected to EDS analysis. However, no noteworthy change could be detected. Only in the cell operated at 800 °C, 80 %MH and OCV detectable amounts of Si were found. This, however, does not appear to have any appreciable effect on electrochemical performance (compare Fig. 50).

5.3.3 Discussion

The increased degradation of P_1 at higher temperatures and current densities correlates well with the observed Ni depletion behavior. As described previously, the longer ionic path in the Ni-depleted electrode leads to an increase of the ohmic resistance, which can be explained by an effective extension of the electrolyte once regions at the interface are fully depleted of Ni. However, the partial removal or loss of percolation of Ni particles without the formation of fully Ni depleted regions would be expected to rather entail an increase of the resistance of the hydrogen electrode process P_1 that contains the coupled ionic conduction and charge transfer since the reaction zone is extended. This is a possible explanation for the observed behavior of P_1 . This is also consistent with Hauch et al., who have observed the degradation of P_1 to be dominant in a Ni/3YSZ electrode and a simultaneous loss of Ni percolation and depletion at the electrode/electrolyte interface.[11]

An additional explanation for the increasing resistance of P_1 could be the decreasing ionic conductivity of the 8YSZ in the hydrogen electrode (YSZ-aging). Its contribution to the degradation of P_1 is expected to occur analogue to the findings presented in chapter 5.1.2. Consequently, this contribution to the increase of P_1 is not expected to be dominant, since the degradation of P_1 and the effect of YSZ aging show opposite temperature dependencies.

The resistance of P_2 does not considerably increase over time. Consequently, Ni depletion at the electrode/electrolyte interface does not have a significant influence on the hydrogen electrode charge transfer resistance. It appears that any Ni removed from the reaction zone results in a shift of the active reaction zone away from the electrolyte. However, it apparently does not affect the triple phase boundary length density and reaction kinetics in the new reaction zone. From this it can be deduced that the removed Ni is mainly transported out of the active electrode into the electrode support. This is substantiated by the similar amount of Ni found in the active electrodes of all operated cells as presented in Table 9. Also pronounced Ni coarsening seems not to be present in the studied cells. Recently, it has been shown that the transition of the reaction zone from the functional to the support layer leads to a significant increase in hydrogen electrode resistance due to slower kinetics.[144] Since this is not observed in the present study the cells' electrodes appear to be sufficiently thick so that the active reaction zone remains within the electrode structure. However, the lack of an increase in P_2 for the duration of the experiment does not negate the fact that Ni is removed from the electrode. If continued, loss of Ni percolation or Ni removal is expected to shift the reaction zone into the electrode support thus reducing the TBP length density and consequently, should lead to increase of P_2 .

The present CNLS fitting procedure was guided by the calculation of DRT for all impedance spectra, as frequently done in literature to improve fitting accuracy.[145–147] However, uncertainties in the reliable separation of the processes P_1 and P_2 could still arise due to the non-physical nature of an equivalent circuit model based on R-CPE elements, making a definite deconvolution of the hydrogen electrode processes difficult. Furthermore, a more detailed understanding of the origins of P_1 and P_2 and how they are affected by different microstructural parameters is still missing, which makes the interpretation of the present degradation results difficult.

5.4 Gas Diffusion and Conversion

The combined contribution of gas conversion and gas diffusion through the substrate do not undergo any significant change during operation at any investigated conditions. This is very plausible as the effect of gas conversion is largely determined by inlet and outlet gas composition. A cell deterioration significantly altering outlet gas composition at constant inlet composition and flow rates as well as steady current density would mean large scale leakage and is equivalent to cell failure. Additionally, the gas concentration profile over the length of the cell has a minor influence on the gas conversion rate. This can, however, be assumed to be virtually stable as a high flow rate and consequently a low steam conversion were chosen, so that reaction rates are largely homogeneous over the length of the cell.

Gas diffusion through the hydrogen electrode support is mainly influenced by support layers porosity and tortuosity as well as by the reaction profile over the length of the cell. As previously explained the latter is not prone to significant changes. Strong alteration in tortuosity and porosity would have to be induced either by large scale impurity depositing or by high mobility of the supports' solid phases. However, no sign of either was detected.

In summary it can be said that for neither gas conversion nor gas diffusion through the cells' support a noteworthy change is expected. In-situ and post-test results are consistent with this consideration and show no changes.

6 Conclusion

The present dissertation provides a deepened understanding of major degradation processes limiting SOEC lifespan. A series of 20 comparable long term degradation measurements elucidates the influence of the major operating parameters temperature, hydrogen gas humidity and current density on individual degradation processes.

This approach allows the identification of four independent degradation processes. Two of them contribute to the ohmic resistance and are only distinguishable due to their different dependence on operating conditions. One of these degradation processes – Ni-depletion – is driven by current density and, is therefore, not observed at OCV. Furthermore, there appears to be a “threshold” for humidity and temperature of 80 %MH and 800 °C, respectively, for this process to occur. The resulting Ni-depleted layer effectively increases electrolyte thickness by a porous YSZ layer, thus increasing ohmic resistance. The underlying mechanism was identified to be related to Ni transport via volatile Ni(OH)_x species. The driving force likely originates from a difference in polarization between the percolation network and previously isolated Ni particles. Additionally, a temperature gradient from the hydrogen electrode towards the support occurring during SOEC operation could contribute.

The second degradation process influencing the ohmic resistance was identified to be caused by a reduction in YSZ’s ionic conductivity, which results from a crystallographic phase change from cubic to tetragonal. It is neither influenced by current density nor by hydrogen gas humidity, but exhibits faster degradation rates at lower temperatures, while its degradation rate is proportional to $t^{0.5}$. While there are several possible theories on the underlying mechanism, the observed dependencies suggest a diffusion limited phase change to be rate determining.

Furthermore, the oxygen electrode is subject to another major degradation process, which is independent of current density as well as hydrogen gas humidity and only occurs at operating temperatures of at least 800 °C. Performance deterioration can clearly be linked to a change in the crystallographic nature of the LSCF layer. The responsible mechanism is likely a phase change possibly as a result of minor chemical demixing. Definitive determination is difficult, since the oxygen electrodes experience some individually diverging deterioration.

Finally, the hydrogen electrode exhibits altering effects during operation. These mostly represent a deterioration of performance. However, especially at low current densities and temperatures electrode activation is observed. Microstructural analysis reveals that with increasing humidity and temperature the Ni phase is experiencing agglomeration. Nevertheless, electrochemical results unambiguously reveal that the performance degradation is mainly not originating from the charge transfer resistance, but rather from the ionic transport through the hydrogen electrode's porous YSZ backbone.

From these findings, a recommendation for operating conditions and cell parameters for maximal longevity can be given. All except one degradation process exhibit significantly lower deterioration rates at 750 °C. Only the aging of the YSZ electrolyte shows higher degradation rates, which can be overcome by slightly increasing Yttria levels in YSZ. Consequently good conditions for stable long term operation are 750 °C, where current densities of up to 1.5 A/cm² can be realized at 80 %MH without the onset of accelerated degradation, while the cell's electrolyte should be doped with approximately 10 mol% Y. If higher temperatures are required in order to achieve higher conversion efficiencies or lower operating voltages at certain current densities (BOP considerations), it is important to limit hydrogen gas humidity to 60 %MH, thereby eliminating Ni-depletion. Nevertheless, operation at 800 °C is accompanied by degradation of the oxygen electrode. This however, should be of diminishing importance for longer term operation due to its increase with the square root of time. Even though no measurements were conducted at 850 °C and 60 %MH, results suggest that at these conditions high current densities and efficiencies can be realized without considerably increasing overall degradation rate, making this point interesting for operation at maximal power densities.

7 Outlook

This work identifies and explains degradation mechanisms occurring during SOEC operation. This understanding is based on 1000 h measurements allowing for a comprehensive parameter study. In order to investigate how rates change for each degradation process over the duration of a cell's typical lifetime, future work should encompass measurements over longer durations (preferably > 10000 h). This should be done at chosen conditions already investigated in this study and at which all identified degradation processes are known to occur, e.g. $800\text{ }^{\circ}\text{C}$, 80 \%MH and 1.0 A/cm^2 .

The results of this study furthermore suggests that operating conditions of $850\text{ }^{\circ}\text{C}$ and 60 \%MH should offer an desirable combination of high efficiencies and comparatively low degradation rates even at high current densities. This should be verified in a long term degradation experiment. Also operation of a cell with slightly increased Yttria content should lead to beneficial results.

Additionally, investigations should be devised based on the obtained understanding to answer final questions concerning the mechanisms of the individual degradation processes. For Ni-depletion this should encompass a study with cells operated at identical conditions which are terminated at different times to get post-test information at different stages of this process providing insight to its progression. Concerning the electrolyte a degradation study with different Yttria doping levels could be conducted, while also the influence of the annealing temperature on YSZ aging should be investigated. Oxygen electrode degradation was shown to be independent of polarization so that tempering experiments should be suitable to tackle questions concerning LSCF alteration.

References

- [1] IEC, *Electrical Energy Storage White Paper*, vol. 39. 2009.
- [2] G. Bopp, M. Merkle, T. Smolinka, S. Schwunk, and G. Ebert, "Fraunhofer ISE Annual Report," 2011.
- [3] G. Fuchs, B. Lutz, M. Leuthold, and D. U. Sauer, "Technology Overview on Electricity Storage - Overview on the potential and on the deployment perspectives of electric storage technologies," *Inst. Power Electron. Electr. Drives (ISEA), RWTH Aachen Univ.*, no. June, p. 66, 2012.
- [4] M. Sterner and I. Stadler, *Energiespeicher - Bedarf, Technologien, Integration*. Springer Berlin Heidelberg, 2014.
- [5] M. A. Laguna-Bercero, "Recent advances in high temperature electrolysis using solid oxide fuel cells: A review," *J. Power Sources*, vol. 203, pp. 4–16, 2012.
- [6] S. C. Singhal and K. Kendall, *High-temperature solid oxide fuel cells : fundamentals, design, and applications*. Elsevier Advanced Technology, 2003.
- [7] K. Huang and J. B. Goodenough, *Solid Oxide Fuel Cell Technology: Principles, Performance and Operations*. Elsevier Inc., 2009.
- [8] R. A. George, "Status of tubular SOFC field unit demonstrations," *J. Power Sources*, vol. 86, no. 1, pp. 134–139, 2000.
- [9] N. M. Sammes, Y. Du, and R. Bove, "Design and fabrication of a 100W anode supported micro-tubular SOFC stack," *J. Power Sources*, vol. 145, no. 2, pp. 428–434, 2005.
- [10] M. C. Tucker, "Progress in metal-supported solid oxide fuel cells: A review," *J. Power Sources*, vol. 195, no. 15, pp. 4570–4582, 2010.
- [11] A. Hauch, K. Brodersen, M. Chen, and M. B. Mogensen, "Ni/YSZ electrodes structures optimized for increased electrolysis performance and durability," *Solid State Ionics*, vol. 293, pp. 27–36, 2016.
- [12] A. Mai, M. Becker, W. Assenmacher, F. Tietz, D. Hathiramani, E. Ivers-Tiffée, D. Stöver, and W. Mader, "Time-dependent performance of mixed-conducting SOFC cathodes," *Solid State Ionics*, vol. 177, no. 19-25 SPEC. ISS., pp. 1965–1968, 2006.
- [13] W. G. Wang and M. Mogensen, "High-performance lanthanum-ferrite-based cathode for SOFC," *Solid State Ionics*, vol. 176, no. 5, pp. 457–

- 462, 2005.
- [14] M. Shah and S. A. Barnett, "Solid oxide fuel cell cathodes by infiltration of $\text{La}_{0.6}\text{Sr}_{0.4}\text{Co}_{0.2}\text{Fe}_{0.8}\text{O}_{3-\delta}$ into Gd-Doped Ceria," *Solid State Ionics*, vol. 179, no. 35, pp. 2059–2064, 2008.
- [15] X. Sun, M. Chen, S. H. Jensen, S. D. Ebbesen, C. Graves, and M. Mogensen, "Thermodynamic analysis of synthetic hydrocarbon fuel production in pressurized solid oxide electrolysis cells," *Int. J. Hydrogen Energy*, vol. 37, no. 22, pp. 17101–17110, 2012.
- [16] P. Moçoteguy and A. Brisse, "A review and comprehensive analysis of degradation mechanisms of solid oxide electrolysis cells," *Int. J. Hydrogen Energy*, vol. 38, no. 36, pp. 15887–15902, 2013.
- [17] J. Schefold, A. Brisse, and F. Tietz, "Nine thousand hours of operation of a solid oxide cell in steam electrolysis mode," *J. Electrochem. Soc.*, vol. 159, no. 2, pp. A137–A144, 2012.
- [18] A. Hauch, S. D. Ebbesen, S. H. Jensen, and M. Mogensen, "Solid oxide electrolysis cells: Microstructure and degradation of the Ni/yttria-stabilized zirconia electrode," *J. Electrochem. Soc.*, vol. 155, no. 11, pp. 1184–1193, 2008.
- [19] A. Hauch, S. H. Jensen, S. Ramousse, and M. Mogensen, "Performance and durability of solid oxide electrolysis cells," *J. Electrochem. Soc.*, vol. 153, no. 9, pp. 1741–1747, 2006.
- [20] R. Knibbe, M. L. Traulsen, A. Hauch, S. D. Ebbesen, and M. Mogensen, "Solid oxide electrolysis cells: Degradation at high current densities," *J. Electrochem. Soc.*, vol. 157, no. 8, 2010.
- [21] A. Hauch, S. H. Jensen, J. B. Bilde-Sørensen, and M. Mogensen, "Silica segregation in the Ni/YSZ electrode," *J. Electrochem. Soc.*, vol. 154, no. 7, pp. 1–8, 2007.
- [22] J. S. Herring, J. E. O'Brien, C. M. Stoots, G. L. Hawkes, J. J. Hartvigsen, and M. Shahnam, "Progress in high-temperature electrolysis for hydrogen production using planar SOFC technology," *Int. J. Hydrogen Energy*, vol. 32, no. 4, pp. 440–450, 2007.
- [23] C. Graves, S. D. Ebbesen, S. H. Jensen, S. B. Simonsen, and M. B. Mogensen, "Eliminating degradation in solid oxide electrochemical cells by reversible operation," *Nat. Mater.*, vol. 14, no. 2, pp. 239–244, Feb. 2015.
- [24] Z. Jiao, N. Takagi, N. Shikazono, and N. Kasagi, "Study on local morphological changes of nickel in solid oxide fuel cell anode using

- porous Ni pellet electrode," *J. Power Sources*, vol. 196, no. 3, pp. 1019–1029, 2011.
- [25] D. A. Osinkin, B. L. Kuzin, and N. M. Bogdanovich, "Effect of Oxygen Activity and Water Partial Pressure to Degradation Rate of Ni Cermet Electrode Contacting Zr_{0.84}Y_{0.16}O_{1.92} Electrolyte," *Russ. J. Electrochem.*, vol. 46, no. 1, pp. 41–48, 2010.
- [26] M. Chen, Y. L. Liu, J. J. Bentzen, W. Zhang, X. Sun, A. Hauch, Y. Tao, J. R. Bowen, and P. V. Hendriksen, "Microstructural degradation of Ni/YSZ electrodes in solid oxide electrolysis cells under high current," *J. Electrochem. Soc.*, vol. 160, no. 8, pp. F883–F891, 2013.
- [27] D. The, S. Grieshammer, M. Schroeder, M. Martin, M. Al Daroukh, F. Tietz, J. Schefold, and A. Brisse, "Microstructural comparison of solid oxide electrolyser cells operated for 6100 h and 9000 h," *J. Power Sources*, vol. 275, pp. 901–911, 2015.
- [28] M. B. Mogensen, A. Hauch, X. Sun, M. Chen, Y. Tao, S. D. Ebbesen, K. V. Hansen, and P. V. Hendriksen, "Relation Between Ni Particle Shape Change and Ni Migration in Ni–YSZ Electrodes – a Hypothesis," *Fuel Cells*, vol. 17, no. 4, pp. 434–441, 2017.
- [29] S. D. Ebbesen, J. Høgh, K. A. Nielsen, J. U. Nielsen, and M. Mogensen, "Durable SOC stacks for production of hydrogen and synthesis gas by high temperature electrolysis," *Int. J. Hydrogen Energy*, vol. 36, no. 13, pp. 7363–7373, 2011.
- [30] J. E. O'Brien, C. M. Stoots, J. S. Herring, K. G. Condie, and G. K. Housley, "The high-temperature electrolysis program at the Idaho National Laboratory: observations on performance degradation," *High Temperature Water Electrolysis Limiting Factors, Eifer, Karlsruhe, Germany, June*. pp. 9–10, 2009.
- [31] Y. L. Liu and C. Jiao, "Microstructure degradation of an anode/electrolyte interface in SOFC studied by transmission electron microscopy," *Solid State Ionics*, vol. 176, no. 5–6, pp. 435–442, 2005.
- [32] A. Nechache, M. Cassir, and A. Ringuedé, "Solid oxide electrolysis cell analysis by means of electrochemical impedance spectroscopy: A review," *J. Power Sources*, vol. 258, pp. 164–181, 2014.
- [33] M. A. Laguna-Bercero, R. Campana, A. Larrea, J. A. Kilner, and V. M. Orera, "Electrolyte degradation in anode supported microtubular yttria stabilized zirconia-based solid oxide steam electrolysis cells at high voltages of operation," *J. Power Sources*, vol. 196, no. 21, pp. 8942–8947, 2011.

- [34] J. R. Mawdsley, J. David Carter, A. Jeremy Kropf, B. Yildiz, and V. A. Maroni, "Post-test evaluation of oxygen electrodes from solid oxide electrolysis stacks," *Int. J. Hydrogen Energy*, vol. 34, no. 9, pp. 4198–4207, 2009.
- [35] P. Hjalmarsson, X. Sun, Y. L. Liu, and M. Chen, "Influence of the oxygen electrode and inter-diffusion barrier on the degradation of solid oxide electrolysis cells," *J. Power Sources*, vol. 223, pp. 349–357, 2013.
- [36] M. Keane, M. K. Mahapatra, A. Verma, and P. Singh, "LSM-YSZ interactions and anode delamination in solid oxide electrolysis cells," *Int. J. Hydrogen Energy*, vol. 37, no. 22, pp. 16776–16785, 2012.
- [37] H. Yokokawa, T. Horita, N. Sakai, K. Yamaji, M. E. Brito, Y. P. Xiong, and H. Kishimoto, "Thermodynamic considerations on Cr poisoning in SOFC cathodes," *Solid State Ionics*, vol. 177, no. 35–36, pp. 3193–3198, 2006.
- [38] Y. Zhen, A. I. Y. Tok, F. Y. C. Boey, and S. P. Jiang, "Development of Cr-tolerant cathodes of solid oxide fuel cells," *Electrochem. Solid-State Lett.*, vol. 11, no. 3, p. B42, 2008.
- [39] X. Chen, L. Zhang, and S. P. Jiang, "Chromium deposition and poisoning on (La_{0.6} Sr_{0.4-x} Ba_x) (Co_{0.2} Fe_{0.8}) O₃ (0 ≤ x ≤ 0.4) cathodes of solid oxide fuel cells," *J. Electrochem. Soc.*, vol. 155, no. 11, p. B1093, 2008.
- [40] M. S. Sohal, J. E. O'Brien, C. M. Stoots, V. I. Sharma, B. Yildiz, and A. Virkar, "Degradation Issues in Solid Oxide Cells During High Temperature Electrolysis," *J. Fuel Cell Sci. Technol.*, vol. 9, no. 1, p. 011017, 2012.
- [41] F. Tietz, D. Sebold, A. Brisse, and J. Schefold, "Degradation phenomena in a solid oxide electrolysis cell after 9000 h of operation," *J. Power Sources*, vol. 223, pp. 129–135, 2013.
- [42] C. Sun, R. Hui, and J. Roller, "Cathode materials for solid oxide fuel cells: A review," *J. Solid State Electrochem.*, vol. 14, no. 7, pp. 1125–1144, 2010.
- [43] H. Yokokawa, H. Tu, B. Iwanschitz, and A. Mai, "Fundamental mechanisms limiting solid oxide fuel cell durability," *J. Power Sources*, vol. 182, no. 2, pp. 400–412, 2008.
- [44] W. Zhang, M. Chen, P. V. Hendriksen, and R. Barfod, "Investigation of Degradation Mechanisms of LSCF Based SOFC Cathodes — by CALPHAD Modeling and Experiments," Department of Energy Conversion and Storage, Technical University of Denmark, 2012.
- [45] E. Bucher and W. Sitte, "Long-term stability of the oxygen exchange properties of (La,Sr) 1 - Z(Co,Fe)O₃ - δ in dry and wet atmospheres,"

- Solid State Ionics*, vol. 192, no. 1, pp. 480–482, 2011.
- [46] D. Oh, D. Gostovic, and E. D. Wachsman, “Mechanism of $\text{La}_{0.6}\text{Sr}_{0.4}\text{Co}_{0.2}\text{Fe}_{0.8}\text{O}_{3-\delta}$ cathode degradation,” *J. Mater. Res.*, vol. 27, no. 15, pp. 1992–1999, 2012.
- [47] Z. Pan, Q. Liu, L. Zhang, X. Zhang, and S. H. Chana, “Effect of Sr surface segregation of $\text{La}_{0.6}\text{Sr}_{0.4}\text{Co}_{0.2}\text{Fe}_{0.8}\text{O}_{3-\delta}$ electrode on its electrochemical performance in Soc,” *J. Electrochem. Soc.*, vol. 162, no. 12, pp. F1316–F1323, 2015.
- [48] S. P. Simner, M. D. Anderson, M. H. Engelhard, and J. W. Stevenson, “Degradation mechanisms of La-Sr-Co-Fe-O₃ SOFC cathodes,” *Electrochem. Solid-State Lett.*, vol. 9, no. 10, p. A478, 2006.
- [49] W. H. Kim, H. S. Song, J. Moon, and H. W. Lee, “Intermediate temperature solid oxide fuel cell using (La,Sr)(Co,Fe)O₃-based cathodes,” *Solid State Ionics*, vol. 177, no. 35–36, pp. 3211–3216, 2006.
- [50] F. Wang, M. Nishi, M. E. Brito, H. Kishimoto, K. Yamaji, H. Yokokawa, and T. Horita, “Sr and Zr diffusion in LSCF/10GDC/8YSZ triplets for solid oxide fuel cells (SOFCs),” *J. Power Sources*, vol. 258, pp. 281–289, 2014.
- [51] T. Jacobsen and M. Mogensen, “The course of oxygen partial pressure and electric potentials across an oxide electrolyte cell,” *ECS Trans.*, vol. 13, no. 26, pp. 259–273, 2008.
- [52] A. D. Smigelskas and E. O. Kirkendall, “Zinc Diffusion in Alpha Brass,” no. 2071. 1946.
- [53] J. D. Kuenzly and D. L. Douglass, “The oxidation mechanism of Ni₃Al containing yttrium,” *Oxid. Met.*, vol. 8, no. 3, pp. 139–178, Jun. 1974.
- [54] Y. Matus, L. C. De Jonghe, X.-F. Zhang, S. J. Visco, and C. P. Jacobson, “Electrolytic Damage in Zirconia Electrolytes,” *ECS Proc. Vol.*, vol. 2003–07, pp. 209–213, Jan. 2003.
- [55] J. Kondoh, T. Kawashima, S. Kikuchi, Y. Tomii, and Y. Ito, “Effect of aging on yttria-stabilized zirconia I. A study of its electrochemical properties,” *J. Electrochem. Soc.*, vol. 145, no. 5, pp. 1527–1536, 1998.
- [56] J. Kondoh, S. Kikuchi, Y. Tomii, and Y. Ito, “Effect of Aging on Yttria-Stabilized Zirconia II,” *J. Electrochem. Soc.*, vol. 145, no. 5, p. 1536, 1998.
- [57] J. Kondoh, S. Kikuchi, Y. Tomii, and Y. Ito, “Effect of aging on yttria-

- stabilized zirconia: III. A study of the effect of local structures on conductivity," *J. Electrochem. Soc.*, vol. 145, no. 5, pp. 1550–1560, 1998.
- [58] M. Hattori, Y. Takeda, Y. Sakaki, A. Nakanishi, S. Ohara, K. Mukai, J. H. Lee, and T. Fukui, "Effect of aging on conductivity of yttria stabilized zirconia," *J. Power Sources*, vol. 126, no. 1–2, pp. 23–27, 2004.
- [59] B. Butz, P. Kruse, H. Störmer, D. Gerthsen, A. Müller, A. Weber, and E. Ivers-Tiffée, "Correlation between microstructure and degradation in conductivity for cubic Y₂O₃-doped ZrO₂," *Solid State Ionics*, vol. 177, no. 37–38, pp. 3275–3284, 2006.
- [60] B. A. Boukamp, "A Linear Kronig-Kramers Transform Test for Immittance Data Validation," *J. Electrochem. Soc.*, vol. 142, no. 6, pp. 1885–1901, 1995.
- [61] M. Schönleber, D. Klotz, and E. Ivers-Tiffée, "A Method for Improving the Robustness of linear Kramers-Kronig Validity Tests," *Electrochim. Acta*, vol. 131, pp. 20–27, 2014.
- [62] M. Schönleber and E. Ivers-Tiffée, "Approximability of impedance spectra by RC elements and implications for impedance analysis," *Electrochem. commun.*, vol. 58, pp. 15–19, 2015.
- [63] S. Risse, N. A. Cañas, N. Wagner, E. Härk, M. Ballauff, and K. A. Friedrich, "Correlation of capacity fading processes and electrochemical impedance spectra in lithium/sulfur cells," *J. Power Sources*, vol. 323, pp. 107–114, 2016.
- [64] I. Biswas, P. Gazdzicki, and M. Schulze, "Surface analytical methods for the development of electrochemical components of polymer electrolyte fuel cells," *ECS Trans.*, vol. 58, no. 1, pp. 1429–1444, Aug. 2013.
- [65] P. Lettenmeier, L. Wang, U. Golla-Schindler, P. Gazdzicki, N. A. Cañas, M. Handl, R. Hiesgen, S. S. Hosseiny, A. S. Gago, and K. A. Friedrich, "Nanosized IrO_x-Ir Catalyst with Relevant Activity for Anodes of Proton Exchange Membrane Electrolysis Produced by a Cost-Effective Procedure," *Angew. Chemie - Int. Ed.*, vol. 55, no. 2, pp. 742–746, Jan. 2016.
- [66] W. G. Bessler, S. Gewies, and M. Vogler, "A new framework for physically based modeling of solid oxide fuel cells," *Electrochim. Acta*, vol. 53, no. 4, pp. 1782–1800, 2007.
- [67] J. Neidhardt, M. Henke, and W. Bessler, "Kinetic Modeling of Nickel Oxidation in SOFC Anodes," *ECS Trans.*, vol. 35, no. 1, pp. 1621–1629, 2011.

- [68] J. P. Neidhardt, R. J. Kee, and W. G. Bessler, "Electrode Reoxidation in Solid-Oxide Cells: Detailed Modeling of Nickel Oxide Film Growth," *ECS Trans.*, vol. 57, no. 1, pp. 2573–2582, 2013.
- [69] A. Gorski, V. Yurkiv, W. G. Bessler, and H. R. Volpp, "Combined theoretical and experimental studies of H₂ and CO oxidation over YSZ surface," *ECS Trans.*, vol. 35, no. 1, pp. 727–737, 2011.
- [70] V. Yurkiv, D. Starukhin, H. R. Volpp, and W. G. Bessler, "Elementary reaction kinetics of the CO/CO₂/Ni/YSZ electrode," *J. Electrochem. Soc.*, vol. 158, no. 1, p. B5, 2011.
- [71] V. Yurkiv, "Reformate-operated SOFC anode performance and degradation considering solid carbon formation: A modeling and simulation study," *Electrochim. Acta*, vol. 143, pp. 114–128, 2014.
- [72] V. Yurkiv, A. Latz, and W. G. Bessler, "Modeling and simulation the influence of solid carbon formation on SOFC performance and degradation," *ECS Trans.*, vol. 57, no. 1, pp. 2637–2647, 2013.
- [73] M. Riegraf, U. Schiller, R. Costa, K. A. Friedrich, A. Latz, and V. Yurkiv, "Elementary Kinetic Numerical Simulation of Ni/YSZ SOFC Anode Performance Considering Sulfur Poisoning," *J. Electrochem. Soc.*, vol. 162, no. 1, pp. 65–75, 2015.
- [74] M. Riegraf, V. Yurkiv, U. Schiller, R. Costa, A. Latz, and K. A. Friedrich, "The Influence of Sulfur Formation on Performance and Reforming Chemistry of SOFC Anodes Operating on Methane Containing Fuel," *J. Electrochem. Soc.*, vol. 162, no. 12, pp. 1324–1332, 2015.
- [75] M. Henke, J. Kallo, K. A. Friedrich, and W. G. Bessler, "Influence of pressurisation on SOFC performance and durability: A theoretical study," *Fuel Cells*, vol. 11, no. 4, pp. 581–591, 2011.
- [76] C. Willich, C. Westner, M. Henke, F. Leucht, J. Kallo, and K. a. Friedrich, "Pressurized Solid Oxide Fuel Cells with Reformate as Fuel," *J. Electrochem. Soc.*, vol. 159, no. 11, pp. F711–F716, 2012.
- [77] M. Henke, C. Willich, C. Westner, F. Leucht, J. Kallo, W. G. Bessler, and K. A. Friedrich, "A validated multi-scale model of a SOFC stack at elevated pressure," *Fuel Cells*, vol. 13, no. 5, pp. 773–780, 2013.
- [78] M. Henke, "Pressurised Solid Oxide Fuel Cells: From Electrode Electrochemistry to Hybrid Power Plant System Integration," Universität Stuttgart, 2015.
- [79] V. Yurkiv, R. Costa, Z. Ilhan, A. Ansar, and W. G. Bessler, "Impedance of the surface double layer of LSCF/CGO composite cathodes: An

- elementary kinetic model,” *J. Electrochem. Soc.*, vol. 161, no. 4, pp. F480–F492, 2014.
- [80] M. Vogler, A. Bieberle-Hütter, L. Gauckler, J. Warnatz, and W. G. Bessler, “Modelling study of surface reactions, diffusion, and spillover at a Ni/YSZ patterned anode,” *J. Electrochem. Soc.*, vol. 156, no. 5, p. B663, 2009.
- [81] A. Leonide, V. Sonn, A. Weber, and E. Ivers-Tiffée, “Evaluation and modelling of the cell resistance in anode supported solid oxide fuel cells,” *ECS Trans.*, vol. 7, no. 1, pp. 521–531, 2007.
- [82] V. Sonn, A. Leonide, and E. Ivers-Tiffée, “Combined deconvolution and CNLS fitting approach applied on the impedance response of technical Ni8YSZ cermet electrodes,” *J. Electrochem. Soc.*, vol. 155, no. 7, pp. B675–B679, 2008.
- [83] A. Leonide, Y. Apel, and E. Ivers-Tiffée, “SOFC modeling and parameter identification by means of impedance spectroscopy,” *ECS Trans.*, vol. 19, no. 20, pp. 81–109, 2009.
- [84] A. Kromp, A. Leonide, A. Weber, and E. Ivers-Tiffée, “Electrochemical analysis of reformat-fuelled anode supported SOFC,” *J. Electrochem. Soc.*, vol. 158, no. 8, p. B980, 2011.
- [85] C. Endler, A. Leonide, A. Weber, F. Tietz, and E. Ivers-Tiffée, “Long-term study of MIEC cathodes for intermediate temperature solid oxide fuel cells,” *ECS Trans.*, vol. 25, no. 2, pp. 2381–2390, 2009.
- [86] J. Nielsen, T. Jacobsen, and M. Wandel, “Impedance of porous IT-SOFC LSCF:CGO composite cathodes,” *Electrochim. Acta*, vol. 56, no. 23, pp. 7963–7974, 2011.
- [87] C. Endler-Schuck, J. Joos, C. Niedrig, A. Weber, and E. Ivers-Tiffée, “The chemical oxygen surface exchange and bulk diffusion coefficient determined by impedance spectroscopy of porous $\text{La}_{0.58}\text{Sr}_{0.4}\text{Co}_{0.2}\text{Fe}_{0.8}\text{O}_{3-\delta}$ (LSCF) cathodes,” *Solid State Ionics*, vol. 269, pp. 67–79, 2015.
- [88] J. Liu and S. A. Barnett, “Thin Yttrium-Stabilized Zirconia Electrolyte Solid Oxide Fuel Cells by Centrifugal Casting,” *J. Am. Ceram. Soc.*, vol. 85, no. 12, pp. 3096–3098, 2004.
- [89] P. Von Dollen and S. Barnett, “A study of screen printed yttria-stabilized zirconia layers for solid oxide fuel cells,” *J. Am. Ceram. Soc.*, vol. 88, no. 12, pp. 3361–3368, 2005.
- [90] H. Zhu, A. Kromp, A. Leonide, E. Ivers-Tiffée, O. Deutschmann, and R. J. Kee, “A model-based interpretation of the influence of anode surface

- chemistry on solid oxide fuel cell electrochemical impedance spectra," *J. Electrochem. Soc.*, vol. 159, no. 7, pp. F255–F266, 2012.
- [91] M. P. Hoerlein, M. Riegraf, R. Costa, G. Schiller, and K. A. Friedrich, "A parameter study of solid oxide electrolysis cell degradation: Microstructural changes of the fuel electrode," *Electrochim. Acta*, vol. 276, pp. 162–175, Jun. 2018.
- [92] J. W. Fergus, "Electrolytes for solid oxide fuel cells," *J. Power Sources*, vol. 162, no. 1, pp. 30–40, Nov. 2006.
- [93] M. Vogler, A. Bieberle-Hütter, L. Gauckler, J. Warnatz, and W. G. Bessler, "Modelling study of surface reactions, diffusion, and spillover at a Ni/YSZ patterned anode," *J. Electrochem. Soc.*, vol. 156, no. 5, pp. B663–B672, 2009.
- [94] W. G. Bessler, M. Vogler, H. Störmer, D. Gerthsen, A. Utz, A. Weber, and E. Ivers-Tiffée, "Model anodes and anode models for understanding the mechanism of hydrogen oxidation in solid oxide fuel cells," *Phys. Chem. Chem. Phys.*, vol. 12, no. 42, pp. 13888–13903, Nov. 2010.
- [95] M. Riegraf, G. Schiller, R. Costa, K. A. Friedrich, A. Latz, and V. Yurkiv, "Elementary Kinetic Numerical Simulation of Ni/YSZ SOFC Anode Performance Considering Sulfur Poisoning," *J. Electrochem. Soc.*, vol. 162, pp. F65–F75, Nov. 2014.
- [96] J. Joos, M. Ender, I. Rotscholl, N. H. Menzler, and E. Ivers-Tiffée, "Quantification of double-layer Ni/YSZ fuel cell anodes from focused ion beam tomography data," *J. Power Sources*, vol. 246, pp. 819–830, 2014.
- [97] M. Chen, Y. L. Liu, J. J. Bentzen, W. Zhang, X. Sun, A. Hauch, Y. Tao, J. R. Bowen, and P. V. Hendriksen, "Microstructural degradation of Ni/YSZ electrodes in solid oxide electrolysis cells under high current," *J. Electrochem. Soc.*, vol. 160, no. 8, pp. F883–F891, 2013.
- [98] Y. Tao, M. B. Mogensen, and S. D. Ebbesen, "Durability of the Solid Oxide Cells for Co-Electrolysis of Steam and Carbon Dioxide under High Current Densities." Department of Energy Conversion and Storage, Technical University of Denmark, 2013.
- [99] M. H. Pihlatie, A. Kaiser, M. Mogensen, and M. Chen, "Electrical conductivity of Ni-YSZ composites: Degradation due to Ni particle growth," *Solid State Ionics*, vol. 189, no. 1, pp. 82–90, 2011.
- [100] M. Hanasaki, C. Uryu, T. Daio, T. Kawabata, Y. Tachikawa, S. M. Lyth, Y. Shiratori, S. Taniguchi, and K. Sasaki, "SOFC durability against standby and shutdown cycling," *J. Electrochem. Soc.*, vol. 161, no. 9, pp. 850–860, 2014.

- [101] D. G. Pierce and P. G. Brusius, "Electromigration: A review," *Microelectron. Reliab.*, vol. 37, no. 7, pp. 1053–1072, Jul. 1997.
- [102] J. Tao, N. W. Cheung, and C. Hu, "Electromigration characteristics of copper interconnects," *IEEE Electron Device Lett.*, vol. 14, no. 5, pp. 249–251, 1993.
- [103] P. C. Wang and R. G. Filippi, "Electromigration threshold in copper interconnects," *Appl. Phys. Lett.*, vol. 78, no. 23, pp. 3598–3600, 2001.
- [104] S. Krumbein, "Metallic Electromigration Phenomena," *IEEE Transactions on CHMT*, *IEEE Trans. CHMT*, vol. 11, no. 1, pp. 5–15, 1988.
- [105] H. Sezer and I. B. Celik, "Phosphine induced Nickel Migration in SOFC Anodes: A Computational Study," *Electrochim. Acta*, vol. 155, pp. 421–430, 2015.
- [106] A. Buerke, H. Wendrock, and K. Wetzig, "Study of electromigration damage in Al interconnect lines inside a SEM," *Cryst. Res. Technol.*, vol. 35, no. 6, pp. 721–730, 2000.
- [107] W. G. Bessler, J. Warnatz, and D. G. Goodwin, "The influence of equilibrium potential on the hydrogen oxidation kinetics of SOFC anodes," *Solid State Ionics*, vol. 177, no. 39–40, pp. 3371–3383, Jan. 2007.
- [108] N. Russner, H. Geisler, S. Dierickx, A. Weber, and E. Ivers-Tiffée, "A Non-Isothermal 2D Stationary FEM Model for Hydrocarbon Fueled SOFCs Stack Layers," *ECS Trans.*, vol. 78, no. 1, pp. 2673–2682, May 2017.
- [109] M. Yashima, K. Ohtake, M. Kakihana, H. Arashi, and M. Yoshimura, "Determination of tetragonal-cubic phase boundary of $Zr(1-x)R(x)O(2-x/2)$ ($R=Nd, Sm, Y, Er$ and Yb) by Raman scattering," *J. Phys. Chem. Solids*, vol. 57, no. 1, pp. 17–24, 1996.
- [110] C. G. Kontoyannis and M. Orkoula, "Quantitative determination of the cubic, tetragonal and monoclinic phases in partially stabilized zirconias by Raman spectroscopy," *J. Mater. Sci.*, vol. 29, no. 20, pp. 5316–5320, 1994.
- [111] D. Stender, R. Frison, K. Conder, J. L. M. Rupp, B. Scherrer, J. M. Martynczuk, L. J. Gauckler, C. W. Schneider, T. Lippert, and A. Wokaun, "Crystallization of zirconia based thin films," *Phys. Chem. Chem. Phys.*, vol. 17, no. 28, pp. 18613–18620, 2015.
- [112] J. Chevalier, L. Gremillard, A. V. Virkar, and D. R. Clarke, "The tetragonal-monoclinic transformation in zirconia: Lessons learned and future trends," *J. Am. Ceram. Soc.*, vol. 92, no. 9, pp. 1901–1920, 2009.

- [113] M. Kilo, M. A. Taylor, C. Argirusis, G. Borchardt, B. Lesage, S. Weber, S. Scherrer, H. Scherrer, M. Schroeder, and M. Martin, "Cation self-diffusion of 44 Ca, 88 Y, and 96 Zr in single-crystalline calcia- and yttria-doped zirconia," *J. Appl. Phys.*, vol. 94, no. 12, pp. 7547–7552, 2003.
- [114] M. Hattori, Y. Takeda, J. H. Lee, S. Ohara, K. Mukai, T. Fukui, S. Takahashi, Y. Sakaki, and A. Nakanishi, "Effect of annealing on the electrical conductivity of the Y₂O₃-ZrO₂ system," *J. Power Sources*, vol. 131, no. 1–2, pp. 247–250, 2004.
- [115] P. Duwez, F. H. Brown, and F. Odell, "The Zirconia-Yttria System," *J. Electrochem. Soc.*, vol. 98, no. 9, pp. 356–362, 1951.
- [116] S. Lakiza, O. Fabrichnaya, M. Zinkevich, and F. Aldinger, "On the phase relations in the ZrO₂-YO_{1.5}-AlO_{1.5} system," *J. Alloys Compd.*, vol. 420, no. 1–2, pp. 237–245, 2006.
- [117] J. Chevalier, L. Gremillard, A. V. Virkar, and D. R. Clarke, "The tetragonal-monoclinic transformation in zirconia: Lessons learned and future trends," *J. Am. Ceram. Soc.*, vol. 92, no. 9, pp. 1901–1920, Sep. 2009.
- [118] M. Yashima, H. Takashina, M. Kakihana, and M. Yoshimura, "Low-Temperature Phase Equilibria by the Flux Method and the Metastable-Stable Phase Diagram in the ZrO₂-CeO₂ System," *J. Am. Ceram. Soc.*, vol. 77, no. 7, pp. 1869–1874, Jul. 1994.
- [119] M. Kilo, C. Argirusis, G. Borchardt, and R. A. Jackson, "Oxygen diffusion in yttria stabilised zirconia - Experimental results and molecular dynamics calculations," *Phys. Chem. Chem. Phys.*, vol. 5, no. 11, pp. 2219–2224, 2003.
- [120] P. K. Schelling, S. R. Phillpot, and D. Wolf, "Mechanism of the cubic-to-tetragonal phase transition in zirconia and yttria-stabilized zirconia by molecular-dynamics simulation," *J. Am. Ceram. Soc.*, vol. 84, no. 7, pp. 1609–1619, 2001.
- [121] D. Fan and L. Q. Chen, "Possibility of Spinodal Decomposition in ZrO₂-Y₂O₃ Alloys: A Theoretical Investigation," *J. Am. Ceram. Soc.*, vol. 78, no. 6, pp. 1680–1686, Jun. 1995.
- [122] E. J. Mittemeijer and F. Sommer, "Solid state phase transformation kinetics: A modular transformation model," *Zeitschrift für Met. / Mater. Res. Adv. Tech.*, vol. 93, no. 5, pp. 352–361, 2002.
- [123] E. A. Jäggle and E. J. Mittemeijer, "Kinetics of interface-controlled phase transformations: Atomistic and mesoscopic simulations," *Int. J. Mater. Res.*, vol. 102, no. 7, pp. 837–845, 2011.

- [124] B. Rheingans and E. J. Mittemeijer, "Phase transformation kinetics: Advanced modeling strategies," *J. Miner. Met. Mater. Soc.*, vol. 65, no. 9, pp. 1145–1154, 2013.
- [125] F. Liu, F. Sommer, C. Bos, and E. J. Mittemeijer, "Analysis of solid state phase transformation kinetics: Models and recipes," *Int. Mater. Rev.*, vol. 52, no. 4, pp. 193–212, 2007.
- [126] S. P. S. Badwal, "Stability of solid oxide fuel cell components," *Solid State Ionics*, vol. 143, no. 1, pp. 39–46, 2001.
- [127] A. V. Virkar, "Mechanism of oxygen electrode delamination in solid oxide electrolyzer cells," *Int. J. Hydrogen Energy*, vol. 35, no. 18, pp. 9527–9543, 2010.
- [128] L. W. Tai, M. M. Nasrallah, H. U. Anderson, D. M. Sparlin, and S. R. Sehlin, "Structure and electrical properties of $\text{La}_{1-x}\text{Sr}_x\text{Co}_{1-y}\text{Fe}_y\text{O}_3$. Part 1. The system $\text{La}_{0.8}\text{Sr}_{0.2}\text{Co}_{1-y}\text{Fe}_y\text{O}_3$," *Solid State Ionics*, vol. 76, no. 3–4, pp. 259–271, 1995.
- [129] L. W. Tai, M. M. Nasrallah, H. U. Anderson, D. M. Sparlin, and S. R. Sehlin, "Structure and electrical properties of $\text{La}_{1-x}\text{Sr}_x\text{Co}_{1-y}\text{Fe}_y\text{O}_3$. Part 2. The system $\text{La}_{1-x}\text{Sr}_x\text{Co}_{0.2}\text{Fe}_{0.8}\text{O}_3$," *Solid State Ionics*, vol. 76, no. 94, pp. 273–283, 1995.
- [130] G. C. Kostogloudis and C. Ftikos, "Properties of A-site-deficient $\text{La}_{0.6}\text{Sr}_{0.4}\text{Co}_{0.2}\text{Fe}_{0.8}\text{O}_{3-\delta}$ -based perovskite oxides," *Solid State Ionics*, vol. 126, no. 1, pp. 143–151, 1999.
- [131] D. Waller, J. A. Lane, J. A. Kilner, and B. C. H. Steele, "The structure of and reaction of A-site deficient $\text{La}_{0.6}\text{Sr}_{0.4} - x\text{Co}_{0.2}\text{Fe}_{0.8}\text{O}_3 - \delta$ perovskites," *Mater. Lett.*, vol. 27, no. 4–5, pp. 225–228, 1996.
- [132] D. Waller, J. A. Lane, J. A. Kilner, and B. C. H. Steele, "The effect of thermal treatment on the resistance of LSCF electrodes on gadolinia doped ceria electrolytes," *Solid State Ionics*, vol. 86–88, no. 2, pp. 767–772, 1996.
- [133] S. Wang, M. Katsuki, M. Dokiya, and T. Hashimoto, "High temperature properties of $\text{La}_{0.6}\text{Sr}_{0.4}\text{Co}_{0.8}\text{Fe}_{0.2}\text{O}_{3-\delta}$ phase structure and electrical conductivity," *Solid State Ionics*, vol. 159, no. 1–2, pp. 71–78, 2003.
- [134] M. Katsuki, S. Wang, M. Dokiya, and T. Hashimoto, "High temperature properties of $\text{La}_{0.6}\text{Sr}_{0.4}\text{Co}_{0.8}\text{Fe}_{0.2}\text{O}_{3-\delta}$ oxygen nonstoichiometry and chemical diffusion constant," *Solid State Ionics*, vol. 156, no. 3–4, pp. 453–461, 2003.
- [135] K. Yasumoto, Y. Inagaki, M. Shiono, and M. Dokiya, "An

- (La,Sr)(Co,Cu)O_{3-δ} cathode for reduced temperature SOFCs,” *Solid State Ionics*, vol. 148, no. 3–4, pp. 545–549, 2002.
- [136] Y. Liu, K. Chen, L. Zhao, B. Chi, J. Pu, S. P. Jiang, and L. Jian, “Performance stability and degradation mechanism of La_{0.6}Sr_{0.4}Co_{0.2}Fe_{0.8}O_{3-δ} cathodes under solid oxide fuel cells operation conditions,” *Int. J. Hydrogen Energy*, vol. 39, no. 28, pp. 15868–15876, 2014.
- [137] S. J. Kim and G. M. Choi, “Stability of LSCF electrode with GDC interlayer in YSZ-based solid oxide electrolysis cell,” *Solid State Ionics*, vol. 262, pp. 303–306, 2014.
- [138] V. M. Goldschmidt, “Die Gesetze der Krystallochemie,” *Naturwissenschaften*, vol. 14, no. 21, pp. 477–485, May 1926.
- [139] R. D. Shannon and IUCr, “Revised effective ionic radii and systematic studies of interatomic distances in halides and chalcogenides,” *Acta Crystallogr. Sect. A*, vol. 32, no. 5, pp. 751–767, Sep. 1976.
- [140] A. Mineshige, J. Izutsu, M. Nakamura, K. Nigaki, J. Abe, M. Kobune, S. Fujii, and T. Yazawa, “Introduction of A-site deficiency into La_{0.6}Sr_{0.4}Co_{0.2}Fe_{0.8}O_{3-δ} and its effect on structure and conductivity,” *Solid State Ionics*, vol. 176, no. 11–12, pp. 1145–1149, 2005.
- [141] G. C. Kostoglou and C. Ftikos, “Properties of A-site-deficient La_{0.6}Sr_{0.4}Co_{0.2}Fe_{0.8}O_{3-δ}-based perovskite oxides,” *Solid State Ionics*, vol. 126, no. 1, pp. 143–151, 1999.
- [142] B. A. Boukamp, M. Verbraeken, D. H. A. Blank, and P. Holtappels, “SOFC-anodes, proof for a finite-length type Gerischer impedance?,” *Solid State Ionics*, vol. 177, no. 26-32 SPEC. ISS., pp. 2539–2541, 2006.
- [143] A. Kromp, S. Dierickx, A. Leonide, A. Weber, and E. Ivers-Tiffée, “Electrochemical analysis of sulfur-poisoning in anode supported SOFCs fuelled with a model reformat,” *J. Electrochem. Soc.*, vol. 159, no. 5, pp. B597–B601, 2012.
- [144] S. Dierickx, T. Mundloch, A. Weber, and E. Ivers-Tiffée, “How sulfur tolerance of two-layered Ni/YSZ anodes is governed by variations in microstructure and thickness,” *ECS Trans.*, vol. 78, no. 1, pp. 1273–1284, 2017.
- [145] A. Kromp, A. Leonide, A. Weber, and E. Ivers-Tiffée, “Electrochemical analysis of reformat-fuelled anode supported SOFC,” *J. Electrochem. Soc.*, vol. 158, no. 8, pp. B980–B989, 2011.
- [146] A. Leonide, V. Sonn, A. Weber, and E. Ivers-Tiffée, “Evaluation and

- modelling of the cell resistance in anode supported solid oxide fuel cells," *ECS Trans.*, vol. 7, no. 1, pp. 521–531, 2007.
- [147] A. Leonide, Y. Apel, and E. Ivers-Tiffée, "SOFC modeling and parameter identification by means of impedance spectroscopy," *ECS Trans.*, vol. 19, no. 20, pp. 81–109, 2009.
- [148] O. Fabrichnaya and F. Aldinger, "Assessment of thermodynamic parameters in the system ZrO₂-Y₂O₃-Al₂O₃," *Zeitschrift für Met. / Mater. Res. Adv. Tech.*, vol. 95, no. 1, pp. 27–39, 2004.